Mass Transport and Durability of Proton-Exchange-Membrane Fuel Cell Electrodes

A Dissertation
Presented to
The Academic Faculty

by

Zhengyuan Jung Fang

In Partial Fulfillment
of the Requirements for the Degree
Doctor of Philosophy in the
School of Chemical and Biomolecular Engineering

Georgia Institute of Technology
December 2020

MASS TRANSPORT AND DURABILITY OF PROTON-EXCHANGE-MEMBRANE FUEL CELLS

Approved by:

Dr. Thomas F. Fuller, Advisor
School of Chemical & Biomolecular Engineering
Georgia Institute of Technology

Dr. Nian Liu
School of Chemical & Biomolecular Engineering
Georgia Institute of Technology

Dr. Faisal Alamgir
School of Materials Science & Engineering
Georgia Institute of Technology

Dr. Pete Ludovice
School of Chemical & Biomolecular Engineering
Georgia Institute of Technology

Dr. Paul A. Kohl
School of Chemical & Biomolecular Engineering
Georgia Institute of Technology

Date Approved: October 15, 2020

Dedicated to Debang Hou and Sir Francis Thomas Bacon.

ACKNOWLEDGEMENTS

I want to first express my gratitude for my mother (Ye Wang) and father (Xiao Fang), who have shaped me as the person I am today. I would not have been able to come to study and complete my degrees in the U.S. without their financial and emotional support. I want to thank Dr. Tom Fuller and Dr. Adam Nolte, who have shaped me as a researcher. Dr. Fuller took a chance in me in the fall of 2015 over two of my fellow classmates who were more qualified and experienced in research than me at that time. Dr. Fuller allowed me to pursue a variety of experiments in both fuel cells and batteries that helped me become a more focused and practical researcher. Dr. Nolte from my undergraduate school, Rose-Hulman, provided me with the invaluable opportunity and guidance on my first undergraduate research project for almost 2 years. I want to thank my thesis committee members who have provided valuable time and suggestions. I am also very grateful for joining Fuller group that helped me grow intellectually, mentally, and physically: Rajiv Jaini, Andrew Star, Tapesh Joshi, Greg Chipman, and Jon Grunewald. There is also a long list of families and friends especially my grandma, Lianying Yang and my college friend, Ted Samore, who have supported and believed in me throughout my time at Georgia Tech. Last but not least, I am thankful for Toyota North America, Kolon Industries from South Korea, and China National Petroleum Corporation-USA, who have financially supported my research work and provided valuable feedback and suggestions.

TABLE OF CONTENTS

LIST OF TABLES

LIST OF FIGURES

LIST OF SYMBOLS AND ABBREVIATIONS

a	Specific area, m^2/m^3
A_{Pt}	Effective surface area of Pt per unit area of MEA or roughness factor, m^2/m^2
b	Tafel slope, V/decade
C	Concentration of species at a particular location depending on its subscript, mol/m^3
D_{Kn,O_2}	Knudsen diffusion of oxygen, m^2/s
$D_{O_2,i}$	Diffusivity of oxygen in ionomer thin film, m^2/s
$D_{O_2,w}$	Diffusivity of oxygen in water film, m^2/s
d_f	Thickness of ionomer thin film, m
d_{pore}	Diameter of agglomerate pore, m
d_{Pt}	Diameter of Pt particles, m
F	Faraday's constant, 96485 C/mol
$F_{adh,flat}$	Adhesive force on a flat surface, N
$H_{O_2,i}$	Henry's constant for O_2 in ionomer thin film, $Pa\text{-}m^3/mol$
$H_{O_2,w}$	Henry's constant for O_2 in water, $Pa\text{-}m^3/mol$
i	Current density, A/m^2
i_{lim}	Limiting current density, A/m^2
i_o	Exchange current density, A/m^2
i_x	Hydrogen cross-over current density, A/m^2
j	Imaginary unit, unitless
j_{ORR}	Oxygen reduction volumetric reaction rate, $mol/(m^3\text{-}s)$
k'	Volumetric reaction rate constant, $mol/(s\text{-}m^3\text{-}Pa)$
k^o	Butler-Volmer rate, s^{-1}

$k_{Pt/i}$ Mass-transfer coefficient for oxygen permeation at Pt/ionomer interface, m/s

$k_{Pt/w}$ Mass-transfer coefficient for oxygen permeation at Pt/water interface, m/s

$k_{w/i}$ Mass-transfer coefficient for oxygen permeation at water/ionomer interface, m/s

l^{ch} Flow channel length, m

ℓ^{L} Catalyst layer thickness, m

ℓ^{GDL} Gas diffusion layer thickness, m

ℓ_{pore} Depth of primary pore in carbon particle, m

m m-th order of ORR reaction, unitless

m_w Mass of water in the catalyst layer

MW Molecular weight

p Pressure, Pa

p_{atm} Atmosphere pressure, Pa

p_l Pressure of liquid

$p_{O_2}^{ch}$ Oxygen pressure in the flow channel, Pa

$p_{O_2,f}$ Oxygen partial pressure in the ionomer thin film

p_{ref} Reference pressure, 101325 Pa

p_c Capillary pressure, Pa

p_w Water vapor pressure, Pa

r_{ORR} Surface oxygen reduction reaction rate, mol/m^2-s

r_θ Surface roughness or roughness ratio of the true wetted area to geometric area, unitless

R Gas constant, 8.3145 J/mol-K

R_{ct} Charge transfer resistance

$R_{H^+}^{CL}$	Proton resistance in the catalyst layer, Ω-m^2
R_Ω	Ohmic resistance, Ω-m^2
s_w	Liquid water saturation, unitless
T	Temperature, K
U^θ	Thermodynamic equilibrium potential, V
V	Potential, V
V_p	Volume of pores in the catalyst layer, m^3
$V_{\text{Transport theo}}$	Theoretical transport polarization, V
V_w	Volume of liquid water in the catalyst layer, m^3
$x_{i.surf}$	Fraction of ionomer surface coverage, unitless
$x_{Pt.surf}$	Fraction of Pt on the surface of carbon support, unitless
Z_W	Warburg impedance, Ω

Greek Letter

α_{0c}	Transfer coefficient of cathode in oxygen reduction reaction, unitless
Γ_v	Vacant catalytic sites, mol/m^2
γ_{lv}	Surface tension between liquid and vapor, J/m^2 of N/m
γ_{sl}	Surface tension between solid and liquid, J/m^2 of N/m
γ_{sv}	Surface tension between solid and vapor, J/m^2 of N/m
γ_{O_2}	Kinetic reaction order with respect to partial pressure of O_2, unitless
ε	Void fraction on the surface, unitless
ε_g^{CL}	Porosity in catalyst layer or void fraction of secondary pores, unitless
η	Effectiveness factor in agglomerate model, unitless
θ_a	Advancing contact angle, °

θ_c	Young's contact angle, °
θ_r	Receding contact angle, °
θ^*	Apparent contact angle, °
ρ_w	Density of water
τ	Time constant in water sorption analysis or in Warburg impedance, s
τ^{CL}	Tortuosity of CL, unitless
ϕ	Thiele modulus, unitless
Φ_1	Potential of carbon/solid phase, V
Φ_2	Potential of ionomer phase, V
ω	Angular frequency, rad/s

Abbreviation

AST	Accelerated stress test
BOP	Balance of Plant
CCL	Cathode Catalyst Layer
CL	Catalyst Layer
CPE	Constant Phase Element
DOE	U.S. Department of Energy
EDS	Energy Dispersive Spectroscopy
EELS	electron energy loss spectroscopy
ESEM	Environmental Scanning Electron Microscopy
EW	Equivalent Weight of ionomer
FCEV	Fuel Cell Electric Vehicle
FIB	Focused-Ion-Beam
GDL	Gas Diffusion Layer
I/C	Ionomer-to-Carbon weight ratio, unitless

KB	Ketjen Black carbon support
MB	Mass Balance
MEA	Membrane Electrode Assembly
MPL	Microporous Layer
NDIR	Non-Dispersive Infrared Detector
PEM	Proton Exchange Membrane
PTFE	Polytetrafluoroethylene
SCCM	Standard Cubic Centimeter per Minute
SEM	Scanning Electron Microscopy
SLPM	Standard Liter per Minute
STEM	Scanning Transmission Electron Microscopy
STXM	Scanning Transmission X-ray Microscopy
TEM	Transmission Electron Microscopy
XPS	X-ray Photoelectron Spectroscopy
XRD	X-Ray Diffraction

SUMMARY

Proton-exchange-membrane (PEM) fuel cells have been demonstrated semi-commercially in automobiles in 2013 such as Toyota's Mirai, Honda's FC Clarity, and Hyundai's ix-35 and Nexo. With an increasing number of new government policies and public desires in many countries to reduce carbon emissions, PEM fuel cells provide a pivotal role in transportation sector. However, the cost, durability, and system specific power remain major barriers to wide market adoption of this technology.

The improvement of PEM fuel cell performance and durability requires a comprehensive understanding of the interactions between the individual components and their durability. In particular, the cathode of PEM fuel cells is often the limiting factor in durability, system cost, and performance. In this work, the durability of commercial membrane electrode assemblies (MEAs) was first studied via the carbon corrosion effect on the wettability of the cathode. The surface roughness and porosity were fitted to surface texture models and it was found that cathodes sustained their wettability after up to 35% of carbon support loss, at which the cell performance dropped below the U.S. Department of Energy's durability-performance target.

Secondly, the surface functionalization of carbon support was studied for its impact on ionomer distribution in the cathode catalyst layer and on mass transport. A total of three schemes were investigated for either grafting positively charged nitrogen surface groups or negatively charged sulfonate groups for three types of carbon supports. In full-cell tests, improvements over high current densities were observed in samples reacted with para-phenylenediamine or ammonia, whereas the performance decreased after functionalization

with sulfonate groups. The improvement at high current densities exceeded the mass-activity improvement and was attributed to reduced mass-transfer polarizations. Furthermore, a statistical approach was explored to examine the changes in ionomer surface coverage using scanning transmission electron microscopy (STEM) images with fluorine energy dispersive spectroscopy (EDS) maps and it was found that ionomer coverage was improved after functionalization with nitrogen containing group, though large variations in ionomer coverage values occurred. In addition, durability study was performed.

Lastly, an agglomerate model-based equivalent-circuit model for studying effect of ionomer on mass transport resistance was developed and the resistance was determined to inversely scale with ionomer. The trend of the simulated data matched that of the experimental cell performance. In addition, the comparison between the results from the model developed by a former group member and the model in this work showed applicability of using dimensions of carbon primary particles in agglomerate models, if local oxygen transport is accounted for.

The major contributions of this dissertation include understanding the role of electrode wettability in durability studies, providing high-performing carbon supports that might be incorporated to the state-of-the-art electrocatalysts, and exploring a new approach to calculate nano-scale ionomer coverage on Pt/C and a model to examine the effect of the ionomer coverage on transport resistance. Recommendations are provided for new experiments to further understand and improve its performance and durability of low Pt loaded electrode towards the technical goals of the PEM fuel cell community.

CHAPTER 1. INTRODUCTION

Proton-exchange-membrane (PEM) fuel cells are an electrochemical device for power generation and an attractive technology for energy conversion and has been mainly used in transportation sector (buses, cars, trains, marine vessels, etc.). In a PEM Fuel cell, hydrogen is supplied to the anode, where protons are generated. The protons transport through a polymer proton-conducting membrane and react with oxygen in the cathode to generate electricity.

When used as a power generator, a PEM fuel cell mainly has two advantages over an internal combustion engine: 1) high efficiency, because the thermal efficiency of an internal combustion engine is limited by the cycle, whereas an electrochemical reaction engine is not. For example, the fuel cell stack in a 2017 Toyota Mirai fuel cell electric vehicle was determined to have a peak efficiency of 66%, whereas a state-of-the-art Toyota diesel engine has a peak thermal efficiency of 44%, which is higher than typically gasoline engines.[1, 2] The theoretical 2) zero emission of pollutants at the point of use, because the product is water without NO_x and carbon emissions. Furthermore, if the hydrogen is generated from renewable energy sources instead of natural gas and is transported by electric hydrogen tanker trucks, the use of PEM fuel cell becomes truly zero emission. Compared to full battery electric vehicles, the main advantage of fuel cell electric vehicles lies in the short refueling time. Because of these advantages, an increasing number of countries and international councils are setting goals and policies for carbon emission reductions by incorporations of hydrogen and fuel cell electric vehicles. In addition, many large corporations with warehouses are switching to fuel cell-powered material handling equipment such as forklifts to meeting their sustainability goals.

1.1 History

In spite of the high research activities of PEM fuel cells today, fuel cells have in fact been known since the 1840s. The first documented fuel cell was developed by Sir William Grove in England in 1845 and was called "gas voltaic battery." The fuel cell consisted of two platinum electrodes and sulfuric acid as the electrolyte. The first practical fuel cell was developed by Sir Francis T. Bacon in 1932 and an alkaline (KOH) solution was the new electrolyte. A 1.5 kW system of the Bacon's cell was used in many Apollo space missions including the moon-landing mission.[3] The first cation-exchange polymer fuel cell was developed by William Grubb and colleagues at General Electric in the 1950s and was used in the Gemini earth-orbiting mission between 1962 and 1965.[3] The Nafion® ionomer was commercialized by DuPont in the 1960s and is still used as the electrolyte in many of the PEM fuel cells today. In the 1980s, Siemens Corp. started to develop PEM fuel cell moduli for submarine applications and class 212 submarines equipped with such fuel cells were produced in Germany.[4] Boeing tested the world's first manned airplane powered by a PEM fuel cell system in 2008.[5] The world's first manufactured FCEV production model, Tucson ix35, was introduced by Hyundai in 2013, though it was only for lease.[6] The car was equipped with a 100 kW fuel cell stack and it has an estimated driving range of 260 miles.[6] The first manufactured FCEV model that customers could purchase was Toyota Mirai launched in 2015.

1.2 Principles of Operation

In a PEM fuel cell, hydrogen oxidation reaction occurs in the anode and oxygen reduction reaction occurs in the cathode; protons transport through a polymer proton-

exchange membrane. Both anode and cathode typically consist of three components: a noble metal or platinum-group-metal (PGM) catalyst for electrochemical reaction sites, carbon black for electron conduction, and an ionomer for ion conduction. Since both the hydrogen oxidation reaction and hydrogen transport are facile in the anode shown in Figure 1-1, most of the research activities have been focused on the catalyst and transport of the cathode. Meanwhile, research on the anode catalysts involves toleration of CO poisoning, because traces of CO are present in hydrogen, the majority of which is produced from steam reforming of natural gas.[7]

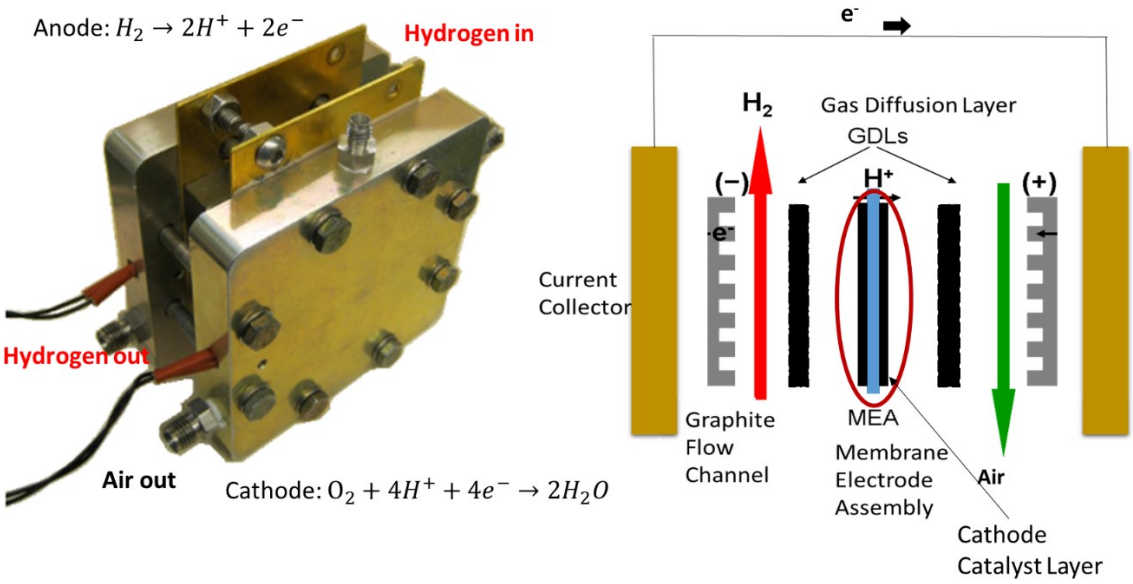

Figure 1-1 (Left) a typical hardware for single cell tests and (right) an exploded view of the hardware and fuel cell components.

1.3 Current Status

1.3.1 Transportation

Although PEM fuel cells have been developed and used as a back-up power supply and power source for personal electronics and mobile devices, the main application is in transportation sector. There has been a chick-or-egg-first kind of debate on which to

develop first, FCEVs or hydrogen stations, for several decades. Auto companies are waiting for sufficient number of hydrogen stations, whereas the hydrogen suppliers/government contractors want to see enough FCEVs on the road before constructing more hydrogen stations.

Figure 1-2 shows that the amount of hydrogen fueling stations and FCEVs both started to experience rapid growths between 2015 and 2016. The growth was catalyzed by the introduction of production FCEV models such as Toyota Mirai in 2015. The concurrent rapid growths indicated the collaborative effort among government agencies, policy makers, and automakers instead of one player dominating the implementation of the hydrogen and fuel cell technologies. In particular, the cumulative number of retail hydrogen fueling stations followed an S-shaped curve, implying the maturation of the technologies related to hydrogen storage and distribution. In addition to the more than 8,000 FCEVs, there are also more than 20,000 PEM fuel cell-powered forklifts in the U.S. by 2019.[8] The operation of these forklifts requires mobile or semi-permanent hydrogen stations. Therefore, the actual number of hydrogen stations supplying for transportation and industry uses should significantly exceed 62 by the end of 2019 shown in Figure 1-2.

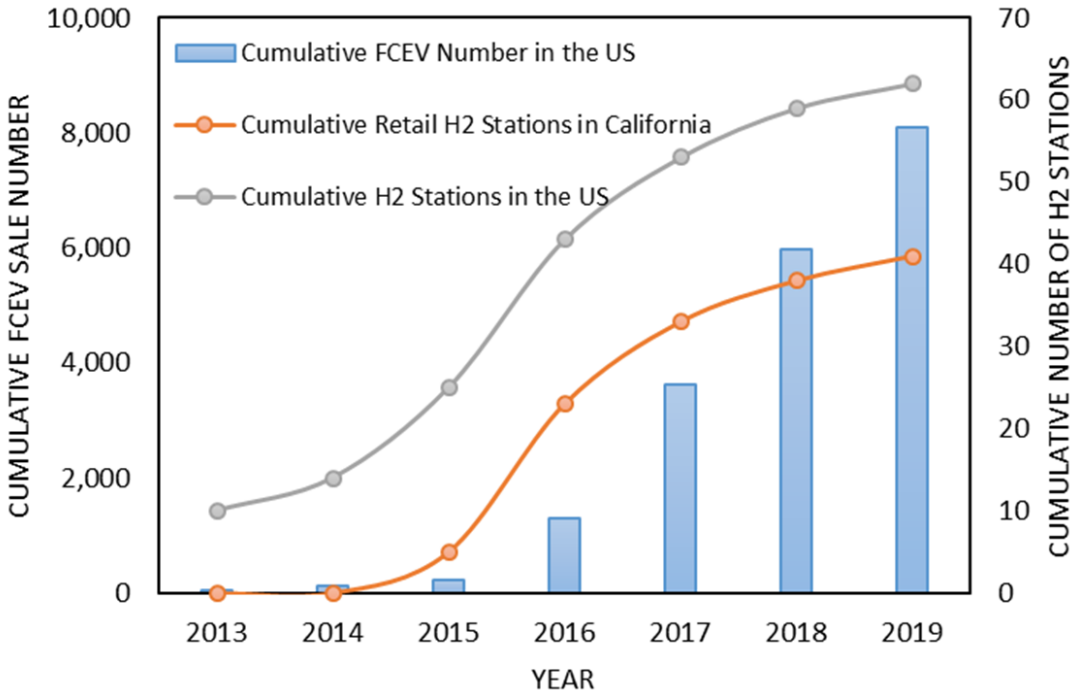

Figure 1-2 Comparison of cumulative numbers of hydrogen fueling stations[9-11] and fuel cell electric vehicles[12-20] in the U.S.

The U.S. pioneered the both the technologies and markets of FCEVs, but East Asian Countries (Japan, South Korea, and China) have emerged as the major players or even the new leaders. The annual sale number of FCEVs appeared to have reached its plateau about 2,100 per year since 2017 in the U.S., whereas the annual sales of FCEVs more than tripled in 2019 in Asia and Europe compared to the numbers in 2018 as shown in Figure 1-3. The more rapid growth in Europe and Asia not only reflects the energy policies of these regions, but also shows the increasing demand from the public for alternative fuel vehicles such as FCEVs. The rapid development of hydrogen infrastructure is another main reason for rapid growths in the two regions. As of the end of 2019, Japan led the world in the total number of hydrogen fueling stations at 111 and Germany ranked the second with 87.[11] Meanwhile, the rest of the world is left behind in fuel cell and hydrogen deployment. As of May of

2020, there was only one hydrogen station in Oceania (in Australia), and none was in Latin America or Africa.

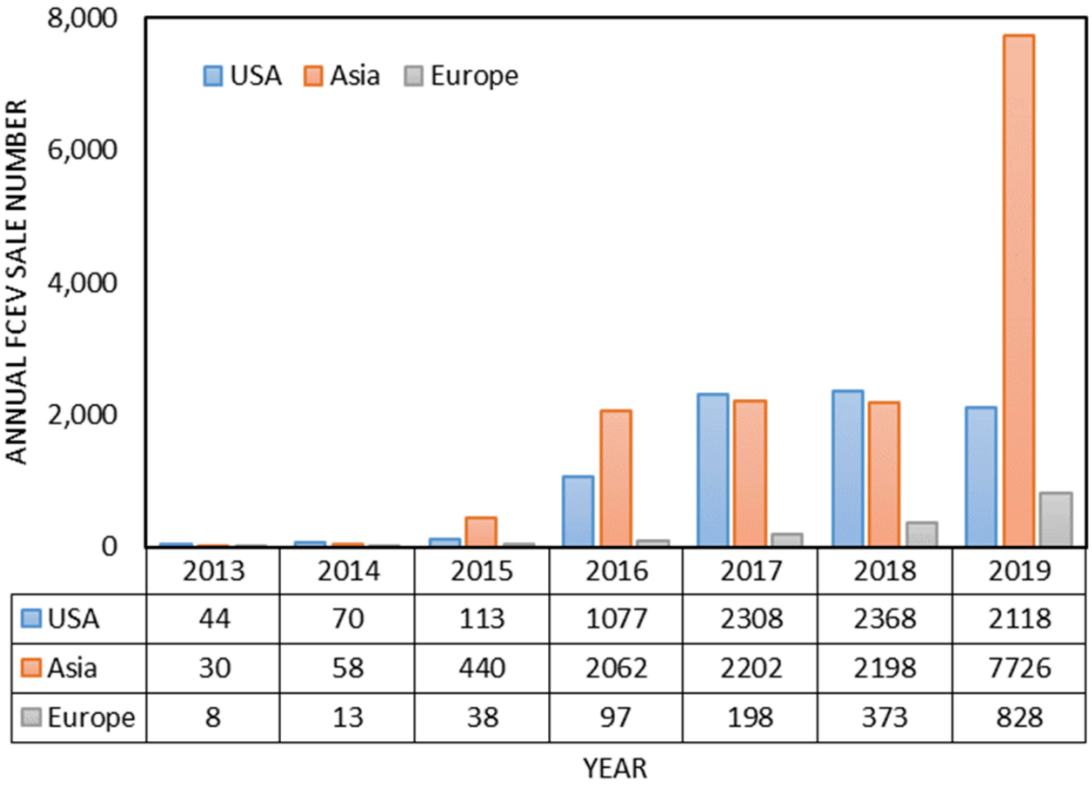

	2013	2014	2015	2016	2017	2018	2019
USA	44	70	113	1077	2308	2368	2118
Asia	30	58	440	2062	2202	2198	7726
Europe	8	13	38	97	198	373	828

YEAR

Figure 1-3 Annual sales of FCEVs by region or country. The FCEVs in this chart include Toyota Mirai,[12, 21-24] Hyundai ix-35,[13, 14] Hyundai Nexo,[6, 14, 15] Honda FCX Clarity,[19, 20, 25-28] and passenger cars and buses manufactured by Chinese auto companies[19, 28, 29] such as FEiCHi Bus.

1.3.2 Academic and Industry Research Activity

In terms of research activities in academics and industries, the research areas of the PEM fuel cells have remained the same: membranes, cathode catalysts and supports, cell hardware, performance, and durability, as shown in DOE fuel cell annual progress reports between 2006 and 2019.[30-32] In contrast, the reports from 2006 to 2008 highlight innovative fuel cell concepts as one of the main research areas, however this is no longer noted in the 2019 report. Furthermore, the largest portion of the funding in 2006 was spent on membrane (19%), whereas in the fiscal year of 2018, the largest spending was on

performance and durability (35%) and membrane was only (9%). The shift indicated the maturation of membrane electrolyte technologies and the long-term and real-world performance and durability was the new focus. Researchers at the national laboratories found that Toyota Mirai surpasses 3,000-h real-world driving (time before the cell voltage drops by 10% between 1.0 to 1.5 A/cm^2), but the PEM fuel cell in Toyota Mirai failed when the DOE accelerated stress test protocols was performed.[8]

For fuel cell component-specific research, the majority of the research activities have been on electrodes or membrane electrode assemblies (MEA). Other components such as gas diffusion layers, membranes, and bipolar plates (or gas flow channels) have received less research interests recently due to the relative maturation of these three components, and their smaller percentages in the total fuel cell stack cost than those of the electrodes.

Membrane

For membrane electrolytes, the desired characteristics include 1) high ionic conductivity, 2) low permeation of hydrogen and oxygen gases, 3) low electrical conductivity, 4) high resistance to HO and HOO radicals, 5) high thermal stability during fuel cell operating temperature range, and 6) mechanical robustness. The high ionic conductivity is the uttermost important feature and it is typically achieved by using a thin membrane such as Gore-Select™ 18 (18 μm thick) compared to early day Nafion® 117 (183 μm thick) or the second-generation Nafion® 212 (51 μm thick). The thin membrane has been achieved from the recent advances in mechanically reinforced polymers, For example, Gore used polytetrafluoroethylene (PTFE) to enhance the mechanical and dimensional stability of the membrane. According to the DOE's annual progress report on fuel cell and hydrogen, the 2017 status has met or surpassed the 2020 targets for

conductivity (resistance < 0.018 Ohm-cm^2 at 30°C), cross-over (<1.9 mA/cm^2 for H_2 and < 0.6 mA/cm^2 for O_2), mechanical (>20,000 cycles with 10 sccm crossover) and chemical (>500 h for 20% loss in OCV with 5 mA/cm^2 crossover) stabilities, and operating temperature range (-20 to 120°C).[33]

Bipolar Plates

For bipolar plates (gas flow channels or flow fields), desired technical properties are 1) high electrical conductivity, 2) resistance to corrosion, 3) high flexural strength, 4) low weight, 5) low H_2 permeation, and 6) good thermal conductivity.[8] The conventional bipolar plates are made of graphite, which possesses high corrosion resistance and high electrical conductivity but is brittle. The new classes of bipolar plates are carbon composites and metals with corrosion resistive coatings. First, the carbon composite bipolar plates are comprised of polymer binder and conductive carbon fillers. The polymer binders provides mechanical strength and gas impermeation, while the carbon fillers provide electrical and heat conduction. Although the carbon composite bipolar plates can be fabricated using standard compression molding suitable for mass production, any non-uniformity during the molding can cause uneven thickness, transport resistance, and potentially gas leakage. Second, the metals, such as stainless steel, aluminum, and titanium, have advantages of high mechanical strength, high thermal and electrical conductivity, low gas permeability, and low thickness, whereas the challenge lies in the resistance to a corrosive environment.[34] To improve the corrosion resistivity, protective coating is typically applied on the metal bipolar plates.[35] For example, titanium bipolar plates coated with π-conjugated amorphous carbon coating were used in 2015 Toyota Mirai FCEVs and it replaced the stainless steel (SUS 316L) used in the previous 2008 model.[36-38] The choice of the amorphous carbon

coating also reduced the cost of the fuel cell stack because it replaced the conventional Au plating treatment for the surface coating of the bipolar plates.[37, 38] By the end of 2017, commercial bipolar plates have reached most of the technical targets for year 2025 except for plate cost ($5.4/kW vs. target $2/kW), weight (0.4 kg/kW vs. target 0.18 kg/kW), and flexural strength (34 MPa vs. target 40 MPa).

In addition to the advances in the bipolar plate materials, there have also been many research and development on the flow field structure. Unlike the specific targets and metrics for bipolar plate materials set by the U.S. DOE, the designs of flow field structures are more of an art than a science. Conventional flow field structures typically use straight channels, which have their drawbacks such as susceptibility to water accumulation under the flow field ribs or lands.[34] To overcome the water accumulation issues, porous metal flow fields were developed. They improved the gas diffusion but suffered from high pressure loss and high manufacturing cost. An innovative 3D fine-mesh flow field structure for the cathode was developed by Toyota and the structure enhanced O_2 diffusion and facilitated removal of product water.[36, 37]

Balance of Plant

Balance of Plant (BOP) refers to other components and subsystems important for integration and operation of a fuel cell system. BOP includes valves, cooling system, heat exchanger, humidifier, air blower, controller, etc. They can be categorized into thermal management system, fuel management system, air management system, and power units. Most of the research and development of BOP focuses on streamlining or eliminating the components to reduce the weight, volume, and cost of a fuel cell system. For example, the

humidifiers for both hydrogen and air were removed in Toyota Mirai and the removal resulted from an innovative design of internal humidification using counter flow cells.[36] They allow the wet gas at the outlet of the flow channels to humidify the dry inlet gas. The humidified gas then hydrates the membrane to maintain its ionic conductivity. The removal of the external humidifiers created a synergy in design because a thinner membrane was used to maintain hydration in lower water content and the design leads to reductions in weight, volume, and cost of the fuel cell system.

1.4 Challenges

In the past five years, although FCEVs from several auto makers have been introduced to the markets, commercialization of the technology still faces technical challenges in system performance, durability, and cost reduction as well as many non-technical hurdles such as lack of public awareness, insufficient hydrogen station availability, etc. The US DOE illustrates the statuses and targets of five technical metrics shown in Figure 1-4.[33] The three challenges are closely interlinked. For example, one way to reduce the system cost is to decrease the catalyst loading in the electrodes; however, low-catalyst loaded electrodes have been reported to degrade than high-catalyst loaded ones.[39]

Another example is the relationship between the system specific power and the system cost. A 900-W fuel cell stack only requires about 1 gram of the Pt catalyst, which accounts for about 1/1000th of the target system weight and thus an additional gram of Pt catalyst can significantly increase the system specific power without much weight increase of the system. Nevertheless, one additional gram of Pt will increase the system cost by $33/kW (Pt spot price was $30.0/g on August 21, 2020), which almost doubles

the system cost target of $35/kW, which includes both the costs of the fuel cell stack and the balance of plant.

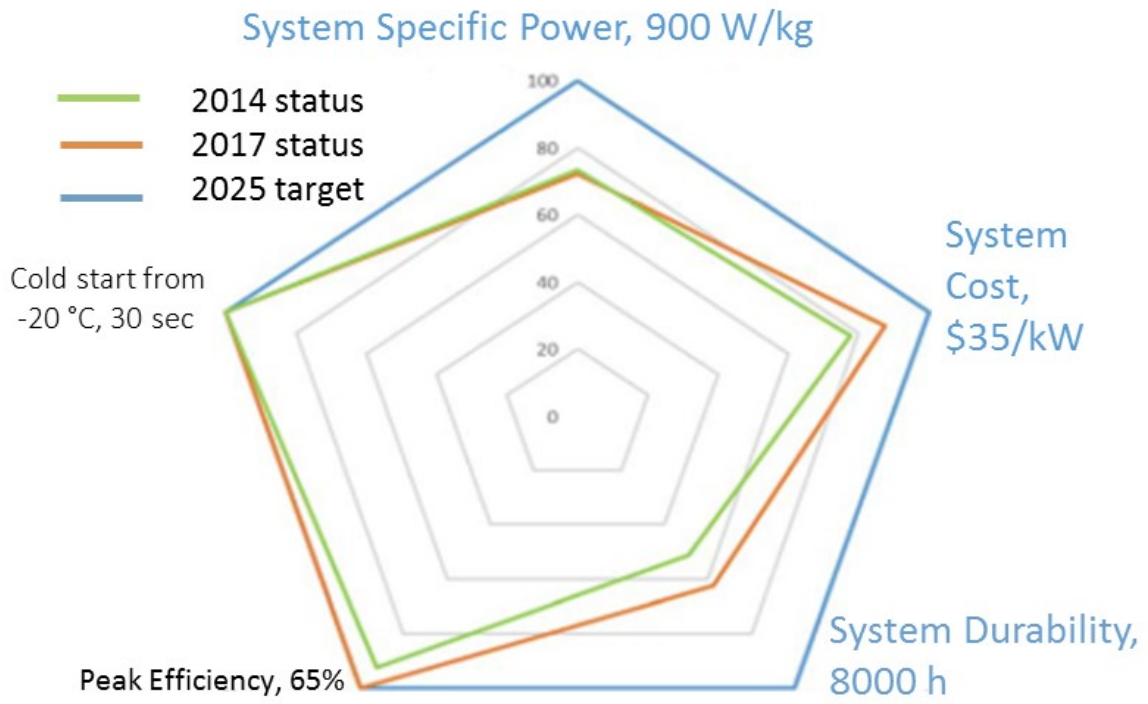

Figure 1-4 PEM fuel cell system status and targets published in 2017.[33]

The system durability appears to be the most challenging and it needs to improve by 90% from the 2017 status to reach the ultimate 8000 h target, which refers to the duration for fuel cell stack operation before the its voltage decreases by more than 10% at normal operating currents. Achieving durability target is almost entirely limited by the MEA performance which was 4100 h as of 2017. The 2020 status will be published in the spring of 2021 and it is likely to be on track to reach the 5000 h target for year 2020.

1.5 References

1. S. Satyapal. National Renewable Energy Lab.(NREL), Golden, CO (United States), 2019.

2. T. Kogo, Y. Hamamura, K. Nakatani, T. Toda, A. Kawaguchi, and A. Shoji. SAE Technical Paper, 2016.

3. M. Warshay and P. R. Prokopius, *NASA Technical Memorandum* (102366), (1989).

4. J. Han, J. F. Charpentier, and T. Tang, *in* "2012 IEEE International Symposium on Industrial Electronics", p. 1456-1461. IEEE, 2012.

5. N. Lapeña-Rey, J. Mosquera, E. Bataller, and F. Ortí, *Journal of aircraft,* **47** (6), 1825-1835 (2010).

6. B. K. Hong and S. H. Kim, *ECS Transactions,* **86** (13), 3-11 (2018).

7. W. Wei and W. Chen, *Journal of Power Sources,* **204** 85-88 (2012).

8. Y. Wang, D. F. R. Diaz, K. S. Chen, Z. Wang, and X. C. Adroher, *Materials Today,* **32** 178-203 (2020).

9. California Fuel Cell Partnership, *Station Map*, (2020). January 2, 2020, https://cafcp.org/stationmap

10. California Fuel Cell Partnership, *A California Road Map,* (1-29), (2014).

11. H2 Stations, *83 new hydrogen refuelling stations worldwide*, H2 Stations.org (2020). May 2, 2020, https://www.h2stations.org/press-release-2020-02-19/

12. Car Sales Base, *TOYOTA MIRAI U.S SALES FIGURES*, (2020). May 1, 2020, https://carsalesbase.com/us-toyota-mirai/

13. Yonhap News Agency, *Hyundai Motor's fuel-cell car sales miss target*, (2015). May 1, 2020, https://en.yna.co.kr/view/AEN20150615002600320

14. Hyundai Media Center, *Hyundai Motor America Reports December 2019 and Total Year Sales*, (2020). May 1, 2020, https://www.hyundainews.com/en-us/releases/2944

15. Car Sales Base, *HYUNDAI NEXO U.S SALES FIGURES*, (2020). May 1, 2020, https://carsalesbase.com/us-hyundai-nexo/

16. Green Car Reports, *Honda Ends Three Green Models for 2015:Insight, FIt EV, FCX Clarity*, (2014). May 1, 2020, https://www.greencarreports.com/news/1092683_honda-ends-three-green-models-for-2015-insight-fit-ev-fcx-clarity

17. M. Kane, *Hydrogen Fuel Cell Car Sales In U.S. Just 2,300 In 2018*, InsideEVs (2019). May 1, 2020, https://insideevs.com/news/342378/hydrogen-fuel-cell-car-sales-in-us-just-2300-in-2018/

18. M. Kane, *In 2019 Sales Of Hydrogen Fuel Cell Cars In The U.S. Decreased*, InsideEVs (2020). May 1, 2020, https://insideevs.com/news/392360/2019-sales-hydrogen-fuel-cell-cars-us/

19. Q. Zhao, *外资大举杀入、丰田现代抢先布局 中国燃料电池车加速从商到乘*, Chinese Automobile Web (2020). May 1, 2020, http://finance.eastmoney.com/a/202003241430262688.html

20. A. Krok, *Honda delivers 2017 Clarity Fuel Cell to first six customers*, Road Show by CNET (2016). May 1, 2020, https://www.cnet.com/roadshow/news/honda-delivers-2017-clarity-fuel-cell-to-first-six-customers/

21. Toyota, *Sales, Production, and Export Results*, (2020). May 2, 2020, https://global.toyota/en/company/profile/production-sales-figures/

22. Car Sales Base, *TOYOTA MIRAI EUROPE SALES FIGURES*, (2020). May 2, 2020, https://carsalesbase.com/europe-toyota-mirai/

23. M. Kane, *Hydrogen Fuel Cell Car Sales In 2019 Improved To 7,500 Globally*, InsideEVs (2020). May 2, 2020, https://insideevs.com/news/397240/hydrogen-fuel-cell-sales-2019-7500-globally/

24. Toyota, *Toyota sells 1.52 million electrified vehicles in 2017, three years ahead of 2020 target*, (2018). May 2, 2020, https://global.toyota/en/newsroom/corporate/20966057.html?adid=ag478_mail&padid=ag478_mail

25. J. Voelcker, *Honda Ends Three Green Models For 2015: Insight, Fit EV, FCX Clarity*, Green Car Reports (2014). May 2, 2020, https://www.greencarreports.com/news/1092683_honda-ends-three-green-models-for-2015-insight-fit-ev-fcx-clarity

26. C. Bruce, *First Honda Clarity Fuel Cell arrives in Europe, they're not for sale*, Motor1 (2016). May 2, 2020, https://www.motor1.com/news/129804/honda-clarity-europe-arrival/

27. D. Hart, J. Lewis, F. Lehner, M. Klippenstein, and R. Rose, 2017.

28. Y. Guo, *2016-2019 氢燃料电池汽车全球产销数据对比*, QN. BJX (2020). May 2, 2020, http://chuneng.bjx.com.cn/news/20200330/1058964.shtml

29. X. Ma, *22 家燃料电池产业链上市公司财务数据比拼*, QN.BJX (2020). May 2, 2020, http://chuneng.bjx.com.cn/news/20200330/1058892.shtml

30. V. Lightner, p. 719-722. US Department of Energy, Annual Progress Report, DOE Hydrogen Program, 2005.

31. N. L. Garland, p. 789-792. US Department of Energy, Annual Progress Report, DOE Hydrogen Program, 2008.

32. D. Papageorgopoulos, p. 1-5. U.S. Department of Energy Annual Merit Review Proceedings, Annual Progress Report, DOE Hydrogen Program, 2019.

33. T. Benjamin, R. Borup, N. Garland, C. Gittleman, B. Habibzadeh, and S. Hirano, *Energy. gov (Office of Energy Efficiency & Renewable Energy),* (2017).

34. M. M. Mench. John Wiley & Sons, Inc, 2008.

35. M. Ueda, Y. Mori, M. Hashimoto, S. Yamamuro, S. Tanase, Y. Aoi, M. Iwasa, and T. Sakai, *Journal of the Japan Institute of Metals,* **71** (7), 545-552 (2007).

36. T. Yoshida and K. Kojima, *The Electrochemical Society Interface,* **24** (2), 45-49 (2015).

37. S. Mizuno, H. Nakaji, and H. Yoshikawa, *Toyota Technical Review,* **61** (2015).

38. K. S. Lyons and B. D. Gould, *in* "Materials Science Forum", Vol. 879, p. 613-618. Trans Tech Publ, 2017.

39. E. Daş, S. A. Gürsel, L. I. Şanlı, and A. B. Yurtcan, *International Journal of Hydrogen Energy,* **42** (30), 19246-19256 (2017).

CHAPTER 2. LITERATURE REVIEW ON ELECTRODE WETTABILITY

Oxygen's inability to rapidly diffuse to electrochemically active catalyst sites underlies these transport resistances, which are greatly increased by degradation experienced over the course of a cell's lifetime, particularly catalyst ripening, catalyst dissolution, and carbon support corrosion. These phenomena may ex-acerbate other problems such as liquid water flooding. In the first aim of this thesis, the effect of wettability changes due to carbon corrosion is investigated by the roles of surface chemistry and microstructure.

2.1 Wetting in Cathode Catalyst Layer and Gas Diffusion Layer

De Gennes *et al*. define wetting as the study of how a liquid spreads on a solid (or liquid) substrate.[1] Similarly, Mench describes the wettability as the tendency of fluid spreading that is controlled by interfacial forces.[2] When two or more fluids are in contact with a solid surface, one of the fluids spreads more easily than the other fluid. The former is called a wetting phase, and the latter is the non-wetting phase.

Water management in PEM fuel cell remains a critical issue. The cathode catalyst layer (CCL) is the major location for simultaneous electrochemical reaction, mass transport, and heat exchange. Wettability plays a key role in establishing the water content in the CCL, which needs sufficient hydration for ionomer conductivity.[3] However, if a CCL possesses too high a degree of wettability, the CCL may be flooded during cell operations, causing increases in the mass-transfer resistance,[4, 5] and electrode sheet resistance.[6]

Gas diffusion layers (GDLs) also play an important role in water management and they have four main functions: 1) directing water from reaction sites of the CCLs to flow

channels, 2) allowing diffusion of reactant gases from catalyst layers to flow channels, 3) conducting electrons, and 4) dissipating heat.[2] On a macroscopic scale, flooding occurs when the presence of liquid water blocks pores and restricts effective diffusion of reactants to the catalyst sites. However, liquid water does not completely fills the pores of the GDL. Owejan, *et al.* found a maximum critical liquid water content, when 44.2 $\pm$ 2.5 vol% of the open pores is filled in a 75% porous GDL at a 0.2 mA/cm^2 current density.[7] After the critical water content is reached, the rate of water removal from the GDL matches the rate of water production from the CCL. Hence, the GDL has to be both hydrophilic enough to drain the generated water from the CCL and hydrophobic enough not to be filled with liquid water, impeding the gas diffusion. The wettability of the GDLs have been widely studied due to its less complexity than CCLs and thus the literature survey focuses on the latter.

2.2 Contact Angle

2.2.1 Static Contact Angle

In order to determine surface wettability, the most common technique is sessile-drop method that optically measures the static or equilibrium contact angle between a liquid drop and a flat surface, θ_c The sliding contact angle, θ_s, can also be measured. The two types of contact angles, static and sliding, are shown in Figure 2-1a and b. A small contact angle (< 90°) corresponds to high wettability or hydrophilicity, while a large contact angle (≥ 90°) correspond to low wettability or hydrophobicity.

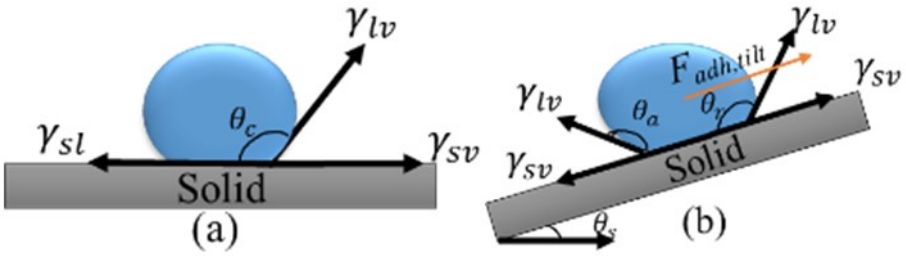

Figure 2-1 Static and sliding contact angles of liquid droplets on the surfaces of hydrophobic solid substrates.

The well-known Young's relation is

$$\gamma_{lv} \cos(\theta_c) = \gamma_{sv} - \gamma_{sl}, \tag{2.1}$$

where γ_{lv} is the surface tension between liquid and vapor, θ_c is the Young's contact angle (static contact angle), γ_{sv} is the surface tension between solid and gas, and γ_{sl} is the surface tension between liquid and solid.[1] Surface tension is defined as the energy that must be supplied to increase the surface area by one unit and Young's contact angle refers to the angle between the surface of the liquid and the outline of the solid surface.[1] In a CCL, the carbon support Vulcan has a contact angle between 65° and 79°[8, 9] and Ketjen black has a contact angle of 84°.[9] Platinum is hydrophilic with a contact angle below 8°,[10] ionomers possess both hydrophilic and hydrophobic parts, pore-formers such as polystyrene has a contact angle of 86°,[11] and additives such as polytetrafluoroethylene (PTFE) is hydrophobic with a contact angle of 110°.[12, 13]

In contrast to these examples for individual constituents, the composition of the surface of the CCL is inhomogeneous; and more importantly, the surface of the catalyst layer is porous and rough. The apparent contact angles of water on pristine CCLs have been reported to range from 130° to 156° in air.[14-18] The surface texture of CCLs is responsible for the larger observed contact angles compared to those of the individual components,

PTFE for example. This phenomenon is well known. Wenzel's and Cassie-Baxter's models are commonly used to describe the effect of the surface texture.[1]

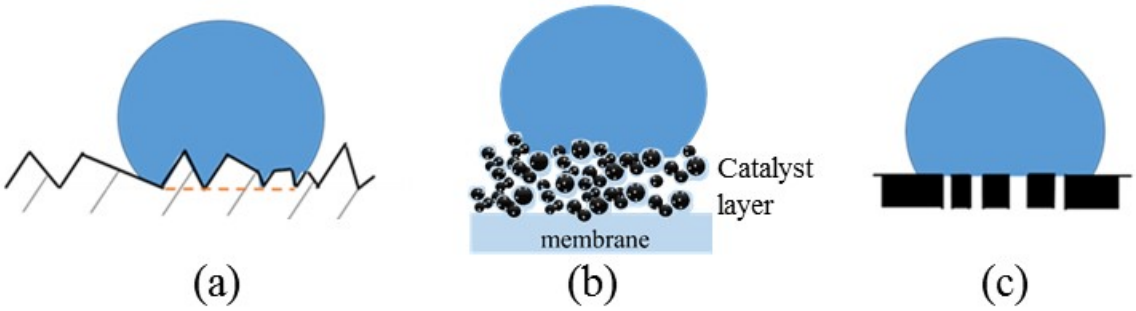

Figure 2-2 Schematics of water droplets on surfaces described by (a) Wenzel's model, (b) a fuel cell catalyst layer attached to a membrane, (c) Cassie-Baxter's model.

Wenzel's model describes the impact of surface roughness on the observed contact angle, as shown in Figure 2-2a. In this model, the apparent contact angle, θ^*, is related to Young's contact angle, θ_c, by

$$\cos(\theta^*) = r_\theta \cos(\theta_c), \tag{2.2}$$

where r_θ is the roughness ratio that represents the ratio of the true wetted area to the apparent surface area (r_θ>1).[19] Therefore, the reported contact angles of 130° to 156° represent the apparent contact angles. According to equation (2.2), the hydrophobicity is magnified because of the surface roughness. Although the roughness factor of the CCLs have not been reported, the images obtained by optical profilometer, atomic force microscope (AFM), or scanning electron microscope (SEM) can be used to approximate the r ranging from 1.1 to 2.[20, 21] It is worth defining another term, roughness factor or effective surface area of Pt, A_{Pt}, the ratio of surface area of electrochemically active catalyst to the geometric surface area of MEA (A_{Pt}>>1). Hence, the definition of the roughness factor is similar to that of the roughness ratio. However, researchers have

reported a wide range of effective surface area values which highly depends on the Pt loading: 278 for a CL with a 0.38 mg Pt/cm^2 loading,[22] 274 for a CL with 5 mg Pt/cm,[2, 23] and 210 for a CL with 0.4 mg Pt/cm^2 [24] as well as roughness factor values as low as 9.2 (Pt wire) ,[25] 20 (10 wt% Pt/C),[26] and 26 with 0.05 mg Pt/cm.[2, 24] If both the high apparent contact angle (156°) and the high roughness factor (278) are chosen, then Young's contact angle, θ_c, becomes 90.2°. If a low roughness factor (20) is assumed, the high apparent contact angle (156°) is converted to a θ_c of 92.6°, which is close to the result using the high-roughness approximation. As a result, the effective surface area of Pt (roughness factor) that has been widely reported does not approximate the roughness ratio in the Wenzel model well. Further calculations based on images of AFM, SEM, or profilometer are needed.

The second model to account for the surface roughness is the Cassie-Baxter, which can be applied to a planar but chemically heterogeneous surface.[27] For a hydrophobic surface, the apparent contact angle is described by

$$\cos(\theta^*) = (1 - \varepsilon)\cos(\theta_c) - \varepsilon, \tag{2.3}$$

where ε is the void fraction on the surface, $(1 - \varepsilon)$ is the solid fraction of the substrate that is underneath the liquid droplet, and θ_c is Young's contact angle. The porosity of CCLs can be determined by a variety of methods including mercury porosimetry[28, 29] and Focused-Ion-Beam Scanning Electron Microscopy (FIB-SEM) images.[28, 30] The major physical difference between the Wenzel and the Cassie-Baxter models lies in void filling. In Wenzel's model, the liquid phase displaces some void (air phase) in the porous substrate while in the Cassie-Baxter model, it does not. In practice, a water droplet may partially fill

the voids. The porosity of the CLs have been reported to vary from 0.20 to 0.65.[15, 30-33] The wide range of the porosity depends on fabrication methods such as hot spray or hot press as well as the use of pore forming additives during the preparation.

A third model is a combined method that account for both the surface roughness and surface inhomogeneity of sample surface.[34] The apparent contact is formulated by

$$\cos(\theta^*) = r_\theta(1-\varepsilon)\cos(\theta_c) - \varepsilon \tag{2.4}$$

2.2.2 Sliding Contact Angle

The force balance on a flat surface is shown in Figure 2-3, and based on Young's relation, the adhesion force of a liquid droplet under drag force on a flat surface is

$$F_{adh,flat} = \gamma_{lv}\, d_w \sin(\theta_c)[\cos(\theta_r) - \cos(\theta_a)], \tag{2.5}$$

where d_w is the equivalent diameter of the wetted area between the droplet and a solid surface; θ_c is the contact angle when no drag force is present (Figure 2-1a); θ_a is the advancing contact angle, which is defined as the upper threshold of contact angle beyond which the contact line between the liquid drop and the solid moves; θ_r is the receding contact angle, which is the lower threshold.[1, 35-37]

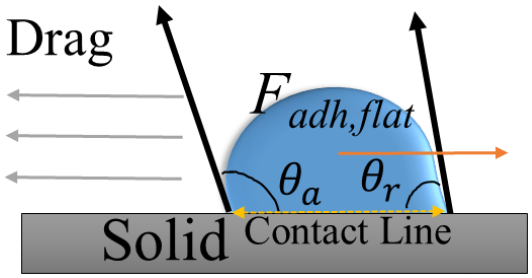

Figure 2-3 Force balance of a liquid droplet on a flat surface under shear flow.

Neumann *et al*. suggest experimental advancing contact angles be better approximations for smooth and chemically heterogeneous solid surfaces such as CCLs.[38, 39] Similarly, Das *et al*., suggest the use of sliding contact angle, whose dynamics is more representative of the droplet mobility and detachment from a GDL surface in a fuel cell. On a tilt stage as shown in Figure 2-1b without determining advancing and receding angles, the adhesion force becomes

$$F_{adh,tilt} = \frac{\rho\, V g \sin(\theta_s)}{\pi\, d_w}, \tag{2.6}$$

where ρ is the liquid density, V is the droplet volume, g is the gravitational acceleration constant, and θ_s is the sliding angle.[37, 40]

The sliding angle is also affected by surface inhomogeneity as seen in the pinning effect shown in Figure 2-4a. It occurs when the contact line between the liquid drop and solid substrate is restrained while the liquid/vapor interface shrinks due to evaporation.[41] For instance, Furuta *et al.* determined that the sliding angle and contact angle hysteresis increased with an increase in the surface roughness using patterned hole radii from 1 to 10 μm on a silicon wafer.[41] Although the sliding angle measurement captures the dynamic water removal well, it does not account for transient contact angle behavior and difference in local composition of the CL. For example, Yu *et al*. studied ex situ, time-dependent contact angles of CLs and found a decreasing trend with time. They also applied environmental scanning electron microscopy (ESEM) to measure micro-contact angle distribution based on the microstructure of the CL.[15] Figure 2-4 shows that a macroscopically hydrophobic CL can allow microscopic wetting behavior, in which

locations with low ionomer content exhibit flat-water droplets, whereas high-ionomer locations show sphere-like droplets.

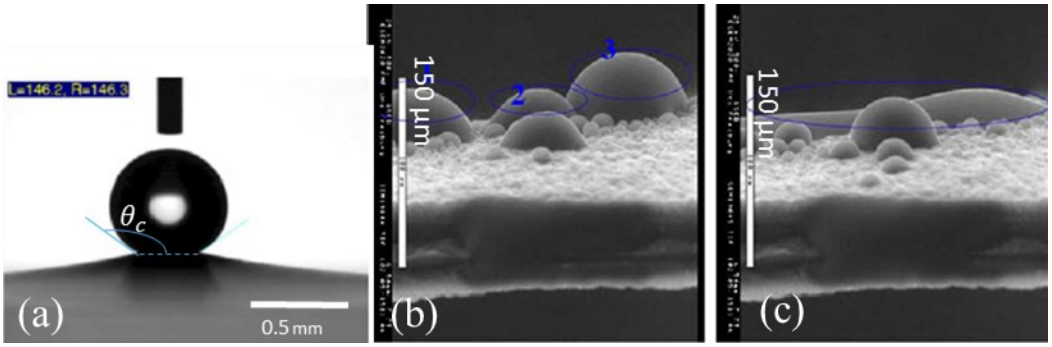

Figure 2-4. (a) Millimeter-size water drop on a CL by a goniometer. (b) and (c) micro-size water droplets (right two) imaged by an environmental scanning electron microscopy. [15]

2.3 Other Characterization Techniques

In addition to contact angle measurements, other ex-situ and in-situ techniques can be applied to visualize and characterize wettability and water content in a fuel cell.

2.3.1 Optical Imaging

First, optical imaging is a simple tool for visualization, which is achieved via specially designed cell architecture. Zhang *et al*. designed and fabricated a transparent cathode end plate with a polycarbonate window shown in Figure 2-5.[42] Figure 2-5a illustrates a droplet of 80 mm on the cathode CL. Despite the presence of a larger droplet in the center view of the image at 0.8 A/cm^2 than that in 0.4 A/cm^2, the liquid water in the pores of the GDL surface exhibited similar quantities at both 0.8 and 0.4 A/cm^2. Kumbur *et al*. constructed a rectangular flow channel (5 mm x 4 mm), optically accessible from the top, with a GDL on the bottom affixed to a feeder plate. This ex situ experimental setup is used to study the effect of surface hydrophobicity of GDLs, and it may be used to examine the surface hydrophobicity of CLs.[43] Although specially designed fuel-cell components for optical accessibility provide direct images of water droplets and useful information on the liquid

motion, they alter the materials of the components and corresponding physical properties, such as thermal conductivity. The altered physical properties can lead to un-reliable predictions for real fuel cell systems.

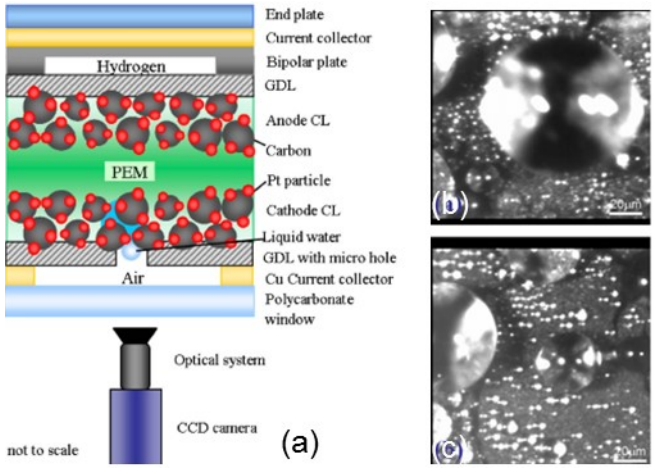

Figure 2-5 (a) In situ visualization fuel cell setup and images obtained by optical lens at b) 0.8 A/cm^2 and c) 0.4 A/ cm^2.[42]

2.3.2 X-Ray Tomography

Second, X-ray tomography acts as a high-resolution technique for imaging operating fuel cells, in which X-ray beam penetrates through GDLs, CLs, and membrane to allow quantifying water content in 3-D. However, there are two drawbacks of X-ray tomography: 1) similar attenuation of the X-ray beam by liquid water and carbon, thus lowering the detection sensitivity shown in Figure 2-6a; 2) The X-ray beam cannot penetrate thick components, such as graphite and aluminum plates used in fuel cells.[44] Despite the sensitivity limitation, a group of Japanese researchers, developed a setup that incorporates soft X-ray radiography (less than 10 keV) for visualizing water content in CLs, microporous layers (MPL), and GDLs in an operating fuel cell. They obtained high spatial (about 1μm) and temporal (1 frame/second) resolution and determined inhomogeneous distribution of water in the CL Figure 2-6 b and c.[45, 46]

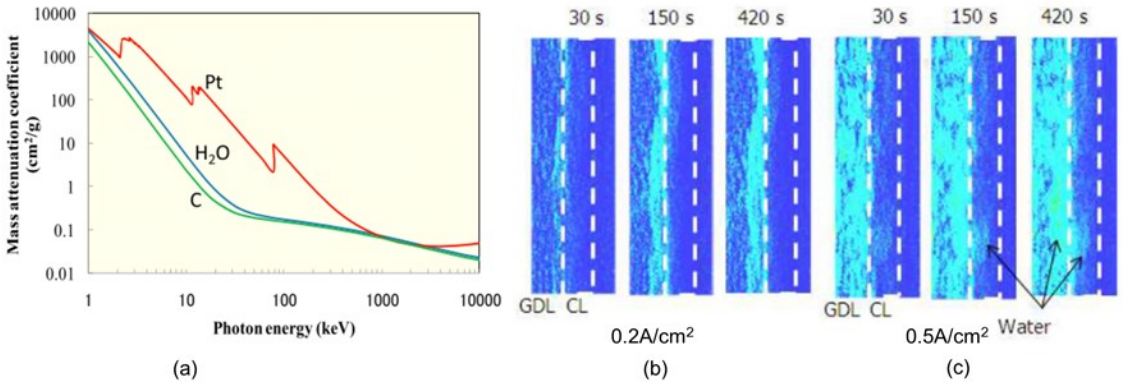

Figure 2-6 (a) Mass attenuation coefficient of the materials in PEM fuel cells. (b) and (c) Time-dependent water distribution visualization in the cathode CL at two different current densities.[46]

2.3.3 Neutron Radiography

Similar to X-ray radiography, neutron radiography, which uses neutron radiation, can also provide fruitful insights for water distribution in a fully operational fuel cells and other thin-porous media. [44, 47, 48] An advantage of neutron over X-ray radiography lies in stronger attenuation of neutrons by water by compared to other materials used in fuel cells. Iranzo *et al*. investigated the effects of operating conditions such as inlet relative humidity on the water accumulation in the flow channels by neutron radiography.[49] Researchers at Sandia National Laboratory performed in situ high-resolution neutron radiography quantifying through-plane liquid water profiles as a function of cell temperature, current density, and anode and cathode gas feed flow rates. They identified the water diffusion from the cathode and thermal gradients as the two most significant effects on water balance in the fuel cell after corrosion[47] A decrease in water retention after corrosion results from pore structure collapse and compaction of the CCL as well as the drying effect of increased internal heat generation. The researchers also point out limitations of the current technique: first, the spatial resolution of neutron radiography is lower than that of X-ray and thickness of CCLs. The resolution of state-of-the-art neutron imaging detectors is about 13 to 16 μm [44, 47]

comparative to the thickness of CCLs ranging from 11 to 15 µm for fresh samples and 3 to 7 µm for corroded samples at 0.4 mg Pt/cm^2 loading.[50, 51] At low Pt loading, the thickness of the cathode is even less. Therefore, neutron radiography cannot probe the interior of the CLs. Second, high flux of neutron sources. In addition, neutron sources need significantly large and costly facilities, which are not practical for installation at universities.

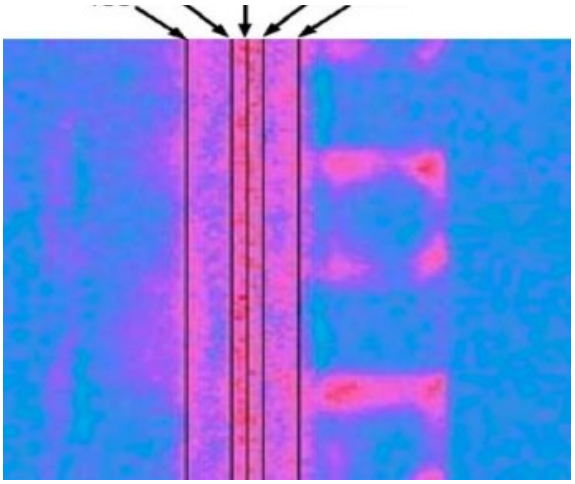

Figure 2-7 Neutron image of water content in pink in PEM fuel cell at 60 °C and 0.5 A/cm^2. Each pixel corresponds to 16.4 µm x 16.4 µm. Pixel number 185 (anode GDL/MPL), 205 (MPL/anode CL), 212 (center of membrane), 219 (cathode CL/MPL), 235 (MPL/cathode GDL) [44].

2.3.4 Dynamic Water Sorption Analysis

Fourth, water sorption/uptake analysis is a useful ex-situ method to probe the interior portions of a CL. The water uptake, λ, is defined as the number of water molecules per sulfonic-acid group. Although this term is mostly used in describing Nafion membranes, it can also represent the water content in the ionomers in the CLs and is expressed as

$$\lambda = \frac{m_w/M_w}{m_i^{dry}/\mathrm{EW}}, \tag{2.7}$$

where m_w is the weight of water absorbed by a CCL sample, M_w is the molecular weight of water, m_i^{dry} is the dry weight of ionomer in the CCL, and EW is the equivalent weight

of the ionomer.[2, 33] To further determine the dynamic behavior of the water uptake, the time constant, τ, is calculated by [33]

$$\frac{m_w(t)}{m_{w,\infty}} = 1 - \exp\left(-\frac{t}{\tau}\right), \tag{2.8}$$

where $m_w(t)$ is time-dependent weight of water absorption measured at each relative humidity and $m_{w,\infty}$ is the equilibrium weight of water absorption. It is important to note that water sorption studies require a free-standing CL sample, which is often difficult to obtain or which deviates from the properties of CL fabricated via conventional methods such as hot-press or direct-spray. Kusoglu *et al.* studied the dynamic water-uptake behavior of the CCL as a function of relative humidity (RH), temperature, Pt-loading, and CL pretreatment using a dynamic-vapor-sorption analyzer.[33] To highlight some of the findings, Figure 2-8a shows that the custom-made CL samples absorb water much less than the Nafion 212 membrane and that the difference in water sorption is magnified at higher RH. Similarly, Goulet *et al.* showed that the presence of CL and GDL made little impact on the mass of water absorbed by the membrane at 70°C, a typical operating temperature for fuel cells (Figure 2-8b).[52] Jung *et al.* also employed dynamic vapor sorption technique and determined that the ionomer in the CL exhibits water content value that is 1/3 of the Nafion membrane.[53] However, none of the authors above have investigated the effect of corrosion on the water uptake of the CL.

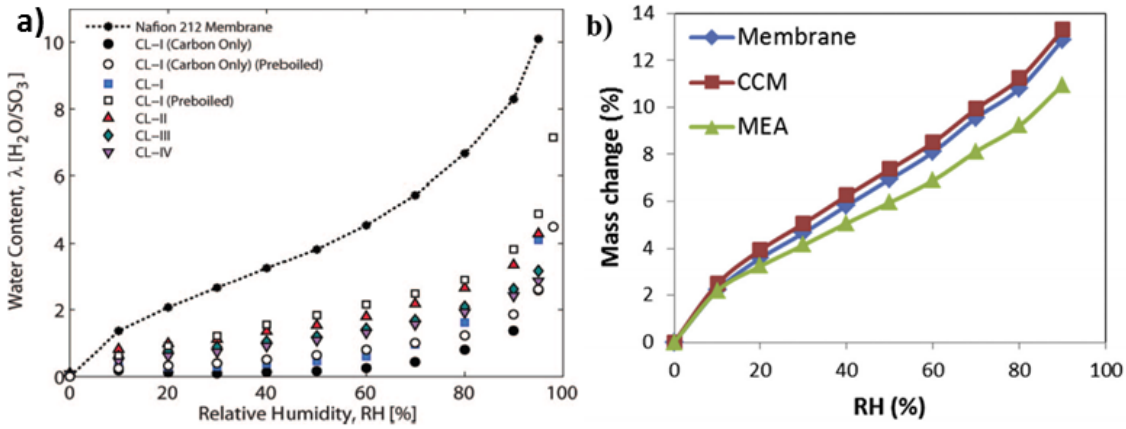

Figure 2-8. a) Water content of CL samples compared to bulk Nafion 212 membrane at 25°C [33] and b) water sorption isotherm in the membrane, catalyst coated membrane (CCM), and 5-layer MEA at 70°C normalized by the initial specimen ionomer content.[52]

Figure 2-9a displays that a higher Pt loading leads to an exponential increase in water uptake. The increase is more significant at low RH, indicating an important design metrics for PEMFC operating at low RH, because the high loading of Pt makes the ionomers in the CL more isotropic and allows for greater swelling. Figure 2-9b shows that it takes longer for the CLs to reach steady states with rising RH and that the time constant from equation (2.8) range from 2 minutes to 20 minutes.

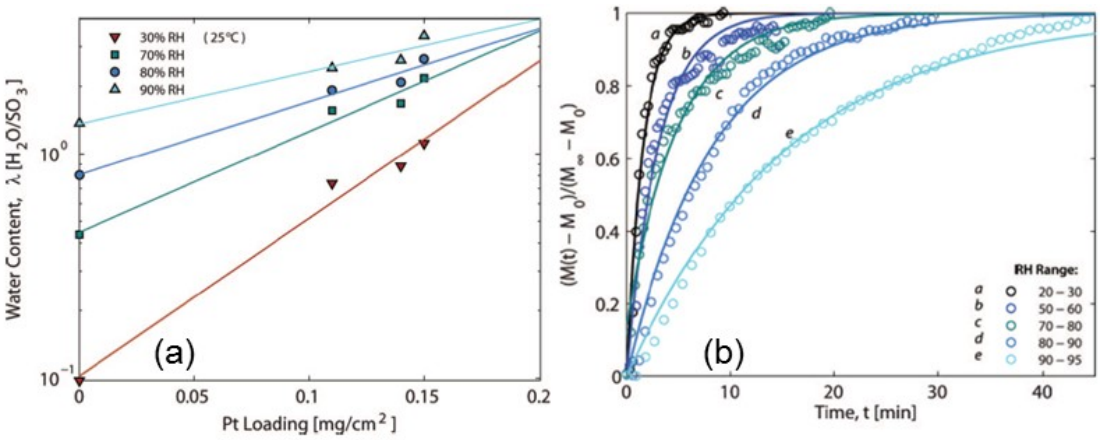

Figure 2-9 (a) Effect of Pt loading on water uptake of CL samples at different RHs. Lines are linear fit to the data. (b) Normalized water uptake of a pre-boiled CL-I sample (in-house made sample with 0.28 ionomer wt-fraction and 1.5 mg Pt/cm^2) 25°C plotted with fits from equation (2.8).[33]

2.3.5 Other Techniques

Furthermore, the relationship between air-water capillary pressure and water saturation can be applied to elucidate the water injection/withdrawal behavior of a CL. The capillary pressure is shown in equation (2.9), and the saturation, s_w, is the fraction of the pore filled by liquid water and is expressed as

$$s_w = \frac{V_w}{V_p} = \frac{m_w/\rho_w}{\pi\, d_p^2 \delta\, \varepsilon}, \tag{2.9}$$

where V_w is the volume of water in the sample, V_p is the CL pore volume, m_w is the mass of water absorbed, ρ_w is the density of water, d_p is the diameter of the pore, δ is the thickness of the sample, and ε is the void fraction of the sample. Gostick *et al.* designed an experimental setup in which the air pressure is controlled to impose a specified capillary pressure and the saturation of the sample is monitored.[54] The setup consists of a pressure gauge, a syringe pump, an analytical balance, and a sample holder as shown in Figure 2-10a. Although the initial setup was used to characterize GDLs, Kusoglu *et al.* employed the methodology for CLs with a modification of starting from fully saturated CL samples rather than from initially dry samples because of the wicking property of the ionomers in the CLs. Kusoglu *et al.* found that a large portion of the curve resides in the negative capillary pressure region (note: p_c in the paper is defined as $p_l - p_w$) shown in Figure 2-10b, indicating that the CLs are at the transition region between hydrophilicity and hydrophobicity. Figure 2-10b also illustrates that the hysteresis loops become narrower with a decrease in the CL sample thickness. The authors suggested an abundance of pores with the similar size that leads to water withdrawal around -5 kPa as evidenced by knee shapes in Figure 2-10b. Based on capillary pressure equation ($p_c = \gamma_{lv} 2\cos(\theta_c)/r$)

Young's contact angle is calculated to be 90.1°,when r of 50 nm [15, 42] and γ of 0.0717 N/m [2] are applied. If the pore size of the CL is 25 nm, the Young's contact angle is 90.05°. The results show that the CL has an appreciable degree of hydrophilicity.

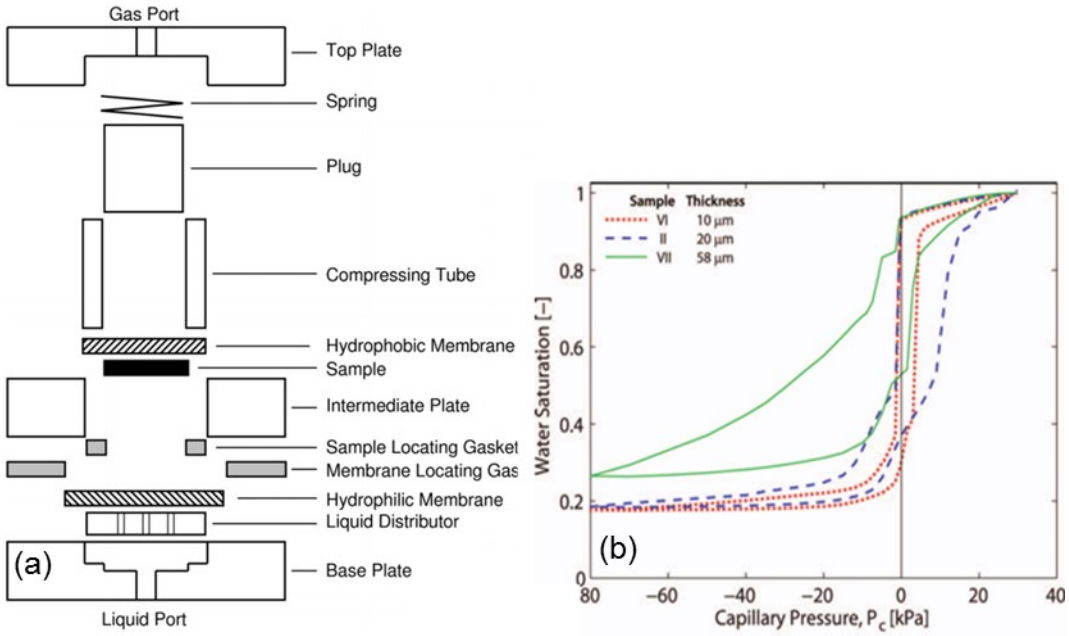

Figure 2-10 (a) Expanded view of the sample holder for capillary pressure-saturation measurements.[54] (b) Relationship between capillary pressure and saturation for catalyst layer samples with different thicknesses.[33]

Moreover, percolation method[55] and droplet impacting method[56] can be applied to study pore and surface wettability, respectively. The percolation consists of two phases: 1) liquid water is injected and fills pores and 2) visible liquid droplets start forming on the surface and deflate pores leading to breakthrough points The percolation studies are typically limited to GDLs and MPLs. Unlike highly porous GDL (porosity >0.8), CL has a much lower pore volume and makes it difficult to allow liquid water to penetrate the CL and thus percolation method is not suitable.[2] Li *et al*. reported a novel impacting method that uses a high-speed camera to capture the droplet dynamics on membrane/Vulcan carbon composite. [56] However, the authors fabricated the composite without Pt particles on a glass slide and thus the composite cannot be assembled in a fuel cell set up.

2.4 Carbon Corrosion Effect on Wettability

The wetting property at the cathode changes as the carbon corrosion progresses and accelerated stress test (AST) is a common method to speed up carbon degradation in fuel cell electrodes. Studies have shown that the water contact angles decrease as a result of increased surface oxides on carbon blacks, which are used as supports.[8, 15, 16, 57] The decreases in contact angles have been correlated to surface oxygen content measured by X-ray photoelectron spectroscopy (XPS).[14, 16, 17, 57] However, carbon mass loss was not reported during these half-cell or full-cell tests. For tests with carbon-loss measurement,[58-61] they lacked studies on the relationship between microstructure change and wettability change due to carbon corrosion. Furthermore, as one of the U.S. Department of Energy's year 2020 technical targets is to improve the durability with cycling to 5,000 hours from the 3,700 hours (the status of year 2017) of 10% voltage loss between 1 A/cm^2 and 1.5 A/cm^2 of the polarization curve, it is important to understand whether the carbon-corrosion induced wettability change occurs before or after the cell performance falls below the technical target.[62, 63]

2.5 References

1. P.-G. De Gennes, F. Brochard-Wyart, and D. Quéré, *Capillarity and wetting phenomena: drops, bubbles, pearls, waves*, Springer Science & Business Media (2013).
2. M. M. Mench. John Wiley & Sons, Inc, 2008.
3. P. K. Das, X. Li, and Z.-S. Liu, *International Journal of Hydrogen Energy,* **35** (6), 2403-2416 (2010).
4. H. Fathi, S. H. Mansouri, and A. Raoof, *Iranian Journal of Hydrogen & Fuel Cell,* **3** (3), 233-245 (2017).

5. F. C. Cetinbas, X. Wang, R. K. Ahluwalia, N. N. Kariuki, R. P. Winarski, Z. Yang, J. Sharman, and D. J. Myers, *Journal of The Electrochemical Society,* **164** (14), F1596-F1607 (2017).

6. D. R. Morris, S. P. Liu, D. Villegas Gonzalez, and J. T. Gostick, *ACS applied materials & interfaces,* **6** (21), 18609-18618 (2014).

7. J. P. Owejan, T. A. Trabold, D. L. Jacobson, D. R. Baker, D. S. Hussey, and M. Arif, *International Journal of Heat and Mass Transfer,* **49** (25–26), 4721-4731 (2006).

8. M. L. Studebaker and C. W. Snow, *The Journal of Physical Chemistry,* **59** (9), 973-976 (1955).

9. K. Kinoshita, (1988).

10. K. Bewig and W. Zisman, *The Journal of Physical Chemistry,* **69** (12), 4238-4242 (1965).

11. Y. Li, J. Q. Pham, K. P. Johnston, and P. F. Green, *Langmuir,* **23** (19), 9785-9793 (2007).

12. D. K. Owens and R. Wendt, *Journal of applied polymer science,* **13** (8), 1741-1747 (1969).

13. V. Gurau, M. J. Bluemle, E. S. De Castro, Y.-M. Tsou, J. A. Mann Jr, and T. A. Zawodzinski Jr, *Journal of Power Sources,* **160** (2), 1156-1162 (2006).

14. G. Álvarez, F. Alcaide, O. Miguel, P. L. Cabot, M. V. Martínez-Huerta, and J. L. G. Fierro, *Electrochimica Acta,* **56** (25), 9370-9377 (2011).

15. H. Yu, C. Ziegler, M. Oszcipok, M. Zobel, and C. Hebling, *Electrochimica Acta,* **51** (7), 1199-1207 (2006).

16. K. H. Kangasniemi, D. Condit, and T. Jarvi, *Journal of The Electrochemical Society,* **151** (4), E125-E132 (2004).

17. J. D. Fairweather, D. Spernjak, A. Z. Weber, D. Harvey, S. Wessel, D. S. Hussey, D. L. Jacobson, K. Artyushkova, R. Mukundan, and R. L. Borup, *Journal of The Electrochemical Society,* **160** (9), F980-F993 (2013).

18. U. H. Jung, K. T. Park, E. H. Park, and S. H. Kim, *Journal of Power Sources,* **159** (1), 529-532 (2006).

19. R. N. Wenzel, *Industrial & Engineering Chemistry,* **28** (8), 988-994 (1936).

20. H. Inoue, H. Daiguji, and E. Hihara, *Jsme International Journal Series B-Fluids and Thermal Engineering,* **47** (2), 228-234 (2004).

21. F. E. Hizir, S. O. Ural, E. C. Kumbur, and M. M. Mench, *Journal of Power Sources,* **195** (11), 3463-3471 (2010).

22. H. Lee, J. Kim, J. Park, Y. Joe, and T. Lee, *Journal of Power Sources,* **131** (1–2), 188-193 (2004).

23. O. J. Murphy, G. D. Hitchens, and D. J. Manko, *Journal of power sources,* **47** (3), 353-368 (1994).

24. H. A. Gasteiger, J. E. Panels, and S. G. Yan, *Journal of Power Sources,* **127** (1–2), 162-171 (2004).

25. A. Parthasarathy, C. R. Martin, and S. Srinivasan, *Journal of The Electrochemical Society,* **138** (4), 916-921 (1991).

26. S. Srinivasan, O. A. Velev, A. Parthasarathy, D. J. Manko, and A. J. Appleby, *Journal of Power Sources,* **36** (3), 299-320 (1991).

27. A. Cassie and S. Baxter, *Transactions of the Faraday Society,* **40** 546-551 (1944).

28. S. Ghosh, H. Ohashi, H. Tabata, Y. Hashimasa, and T. Yamaguchi, *International Journal of Hydrogen Energy,* **40** (45), 15663-15671 (2015).

29. M. Uchida, Y. Aoyama, N. Eda, and A. Ohta, *Journal of The Electrochemical Society,* **142** (2), 463-468 (1995).

30. A. G. Star and T. F. Fuller, *Journal of The Electrochemical Society,* **164** (9), F901-F907 (2017).

31. S. Litster and G. McLean, *Journal of Power Sources,* **130** (1–2), 61-76 (2004).

32. A. Fischer, J. Jindra, and H. Wendt, *Journal of Applied Electrochemistry,* **28** (3), 277-282 (1998).

33. A. Kusoglu, A. Kwong, K. T. Clark, H. P. Gunterman, and A. Z. Weber, *Journal of The Electrochemical Society,* **159** (9), F530-F535 (2012).

34. J. T. Gostick, M. W. Fowler, M. A. Ioannidis, M. D. Pritzker, Y. M. Volfkovich, and A. Sakars, *Journal of Power Sources,* **156** (2), 375-387 (2006).

35. W. Shen, Kim, J. W., and Kim, C. J., *IEEE Conference MEMS,* 52-55 (2002).

36. F. Zhang, X. Yang, and C. Wang, *Journal of the Electrochemical Society,* **153** (2), A225-A232 (2006).

37. P. K. Das, A. Grippin, A. Kwong, and A. Z. Weber, *Journal of The Electrochemical Society,* **159** (5), B489-B496 (2012).

38. A. Neumann, R. Good, C. Hope, and M. Sejpal, *Journal of Colloid and Interface Science,* **49** (2), 291-304 (1974).

39. D. Kwok and A. W. Neumann, *Contact angle, wettability and adhesion,* **3** 117-159 (2003).

40. A. D. Santamaria, P. K. Das, J. C. MacDonald, and A. Z. Weber, *Journal of The Electrochemical Society,* **161** (12), F1184-F1193 (2014).

41. T. Furuta, M. Sakai, T. Isobe, S. Matsushita, and A. Nakajima, *Langmuir,* **27** (11), 7307-7313 (2011).

42. F. Zhang, D. Spernjak, A. K. Prasad, and S. G. Advani, *Journal of the Electrochemical Society,* **154** (11), B1152-B1157 (2007).

43. E. C. Kumbur, K. V. Sharp, and M. M. Mench, *Journal of Power Sources,* **161** (1), 333-345 (2006).

44. M. Hickner, N. Siegel, K. Chen, D. Hussey, D. Jacobson, and M. Arif, *Journal of The Electrochemical Society,* **155** (4), B427-B434 (2008).

45. P. Deevanhxay, T. Sasabe, S. Tsushima, and S. Hirai, *ECS transactions,* **50** (2), 335-341 (2013).

46. S. Tsushima, P. Deevanhxay, T. Sasabe, and S. Hirai, *ECS Transactions,* **50** (2), 327-333 (2013).

47. J. D. Fairweather, D. Spernjak, J. Spendelow, R. Mukundan, D. S. Hussey, D. L. Jacobson, and R. L. Borup, *ECS Transactions,* **58** (1), 301-307 (2013).

48. D. S. Hussey, D. Spernjak, A. Z. Weber, R. Mukundan, J. Fairweather, E. L. Brosha, J. Davey, J. S. Spendelow, D. L. Jacobson, and R. L. Borup, *Journal of Applied Physics,* **112** (10), 104906 (2012).

49. A. Iranzo, P. Boillat, J. Biesdorf, and A. Salva, *Energy,* **82** 914-921 (2015).

50. K. Eom, Y. Y. Jo, E. Cho, T.-H. Lim, J. H. Jang, H.-J. Kim, B. K. Hong, and J. H. Lee, *Journal of Power Sources,* **198** 42-50 (2012).

51. K. Eom, G. Kim, E. Cho, J. H. Jang, H.-J. Kim, S. J. Yoo, S.-K. Kim, and B. K. Hong, *International Journal of Hydrogen Energy,* **37** (23), 18455-18462 (2012).

52. M.-A. Goulet, S. Arbour, M. Lauritzen, and E. Kjeang, *Journal of Power Sources,* **274** 94-100 (2015).

53. C.-Y. Jung and S.-C. Yi, *Electrochemistry Communications,* **35** 34-37 (2013).

54. J. T. Gostick, M. A. Ioannidis, M. W. Fowler, and M. D. Pritzker, *Electrochemistry Communications,* **10** (10), 1520-1523 (2008).

55. C. Quesnel, R. Cao, J. Lehr, A.-M. Kietzig, A. Z. Weber, and J. T. Gostick, *The Journal of Physical Chemistry C,* **119** (40), 22934-22944 (2015).

56. X. Li, F. Feng, K. Zhang, S. Ye, D. Y. Kwok, and V. Birss, *Langmuir,* **28** (16), 6698-6705 (2012).

57. K. Kinoshita and J. A. S. Bett, *Carbon,* **13** (5), 405-409 (1975).

58. W. Gu, R. N. Carter, T. Y. Paul, and H. A. Gasteiger, *ECS transactions,* **11** (1), 963-973 (2007).

59. N. Takeuchi and T. F. Fuller, *ECS Transactions,* **16** (2), 1563-1571 (2008).

60. S. Dhanushkodi, M. Tam, S. Kundu, M. Fowler, and M. Pritzker, *Journal of Power Sources,* **240** 114-121 (2013).

61. R. L. Borup, D. D. Papadias, R. Mukundan, D. Spernjak, D. A. Langlois, R. Ahluwalia, K. L. More, and S. Grot, *Ecs Transactions,* **69** (17), 1029-1038 (2015).

62. DOE, U.S. Department of Energy Annual Merit Review Proceedings, 2016.

63. D. Papageorgopoulos, *in* "U.S. Department of Energy ", U.S. Department of Energy Annual Merit Review Proceedings, 2017.

CHAPTER 3. EXPERIMENTAL METHODS FOR WETTABILITY STUDY

This work investigated the changes in wetting properties of CCLs due to carbon corrosion. The sessile drop method was used to determine apparent contact angles, and XPS to study the surface compositional changes. Surface roughness was obtained by AFM and used to parameterize Wenzel's model. Porosity was obtained by FIB-SEM and separately, by a mass-balance approach. The porosity was used to parameterize Cassie-Baxter's model as well as the combined model.

3.1 Fuel Cell Materials and Operations

The membrane-electrode-assemblies (MEAs) with 0.3 mg_{Pt}/cm^2 (Ion Power NR-212) were used in all experiments. TGP-H-060 Toray carbon paper with 5% wet proofing was used as gas diffusion media (Fuel Cell Store). Gaskets were 127 μm (5 mil nominal) PTFE sheets (McMaster-Carr) that were die-cut. Cells were assembled in 25 cm^2 single cell hardware with triple serpentine Poco graphite flowfields (Fuel Cell Technologies). The hardware was joined by eight bolts that were fastened to a torque of 4.0 N-m. Cells were tested using a Scribner 850e fuel-cell test system with an 880 frequency response analyzer. The cells were wet-up for an hour and broken in by sixty cycles on hydrogen and air. Each cycle consisted of three holds: 0.6 V for one minute, open circuit (OCV) for one minute, and 0.2 V for one minute. The characterization of the cells include H_2/air polarization curves and electrochemical impedance spectroscopy (0.5 SLPM H_2 | 1.5 SLPM Air, 70 °C, 75% RH, no back pressure) and H_2/N_2 cyclic voltammetry (0.1 SLPM H_2/0.15 SLPM N_2, 70°C, 75% RH). The beginning-of-life (BOL) state of an MEA was assessed after wet-up, break-in, and characterization and was marked as zero carbon loss. The impedance

response was measured from 10 kHz to 10 mHz with 5% of DC current as perturbation. The electrochemical surface area (ECSA) was obtained by hydrogen adsorption peaks in a CV scanning from 0.1V to 0.8V at 50 mV/sec using a Metrohm Autolab 302N potentiostat/galvanostat.

3.2 Carbon Loss Measurement

Carbon dioxide from the cathode exhaust was detected with a California Analytical Instruments 601 non-dispersive infrared detector (NDIR). The ASTs included potential holds and square-wave cycling. The details of applied potentials are described in Results and Discussions section. All ASTs were performed at 70 °C with 0.25 SLPM H_2 (75% RH) at the anode and 0.25 SLPM N_2 (75% RH) at the cathode. The cathode exhaust was connected to a Nafion membrane tube drier (Perma Pure, model MD-110-48F-4) and then a condenser to eliminate liquid water formation in the NDIR system whose operating temperature was around 40 °C.

3.3 Porosity Analysis

Two approaches to determine the porosity of cathode catalyst layers were used. First, focused-ion-beam scanning electron microscopy (FIB-SEM) was performed on Nova Nanolab 200. Following the disassembly of the fuel cell and drying of the MEA under ambient environment, fast drying silver suspension (Ted Pella) and copper tape (3M) were used to affix approximately 2 mm x 2 mm MEA samples to a SEM stub. The FIB parameters were 30 kV and 10 pA with nominal slice thickness specified at 20 nm. At least 90 slices of image were taken for each CCL. The porosity was calculated by the ratio of void voxels to total voxels [1]. A mass-balance approach was used as a second method to

estimate the porosity. Here, the MEA was freeze-cut by liquid nitrogen and the cross-sectional thickness was determined by SEM. The porosity was calculated using vendor's information on Pt loading and thermogravimetric analysis (TGA) confirmation for loadings of other components.

3.4 Contact Angle Measurement

A small piece (about 1 cm × 1 cm) of an MEA was cut out and taped on a clean glass slide with CCL facing up. The glass slide was placed in a glass casing to minimize disturbances from ambient air; apparent contact angles and sliding contact angles were measured by a goniometer (Model 250 ramé-hart) as shown in Figure 3-1. A 10 µL water droplet was used, and it covered approximately 1 mm^2 area on the CCL. Measurements within the first three seconds were used due to the transient behavior of the water adsorption of the Nafion ionomer. Values from at least four measurements were averaged for each data point shown in plots in the results section. The contact angle of gas diffusion media was measured before and after ASTs.

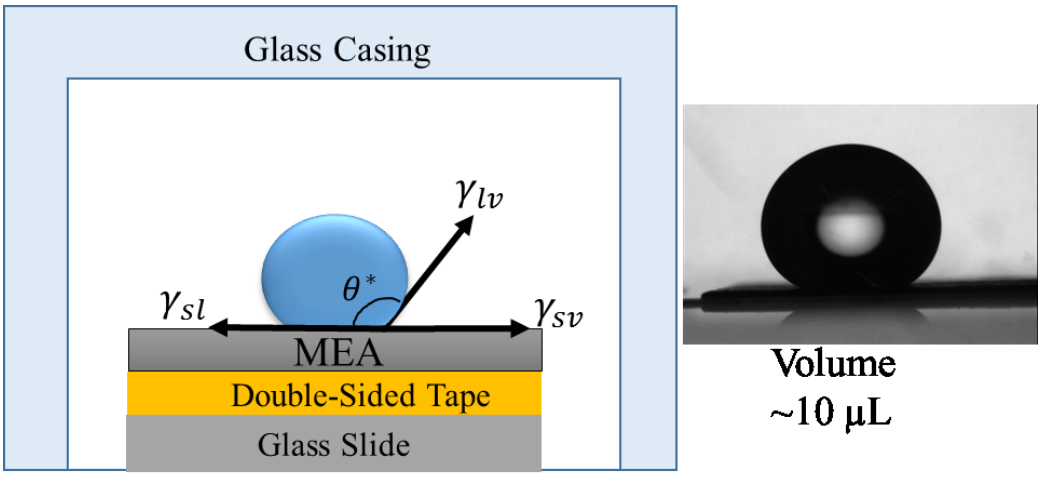

Figure 3-1 Sessile drop measurement setup and an image of water droplet on BOL MEA

3.5 Surface Analysis – XPS and AFM

The surface chemical composition was determined by XPS (Thermo K-Alpha XPS System). The survey and high-resolution scans were set to 160 eV and 40 eV, respectively. The surface morphology was determined using AFM (Veeco Dimension 3100). The cantilever had a spring constant of 5 N/m. The MEA for the AFM measurement was similarly prepared as that for the contact angle measurements. The size of each AFM image was 5 μm × 5 μm with 512 scans/line (lateral resolution ≈ 10 nm). At least two spots were measured for each cathode side of the MEA.

3.6 References

1. A. G. Star and T. F. Fuller, *Journal of The Electrochemical Society,* **164** (9), F901-F907 (2017).

CHAPTER 4. RESULT AND DISCUSSION OF WETTABILITY STUDY

4.1 Cell Performance and Contact Angles

The corrosion-performance landscape was determined by a series of AST protocols including potential holds and square-wave cycling as shown in Table 4-1. The AST potentials below 1 V are proposed to correlate to Pt particle size increase and Pt dissolution, whereas AST potentials above 1 V are used to isolate carbon loss.[1] The potential cycling between 0.4V and 1.3V, for example, ensures passivating surface groups to be continuously formed and reduced. The potential holds at 1.2V or 1.3V are related to start-up and shut-down conditions, in which short-term potential excursion of the cathode increases to 1.2 - 1.5 V due to H_2/air fronts in the anode compartment. The practical operations of PEM fuel cells are dynamic-potential conditions, which can be reasonably approximated by potential cycling ASTs.[2] In this study, the results after potential cycling was the focus of the contact angle model analysis.

Table 4-1 Fuel cell AST protocols and some of the corresponding carbon losses shown in Figure 4-1. All protocols were performed at 75% RH except the fuel cell #6 at 50% RH.

Fuel Cell #	AST Protocol	Carbon Loss ($\mu g/cm^2$)	Percent Carbon Loss (%)
1	None	0	0
2	5 h at 1.2 V	12	3
3	108 cycles of 0.1 V (30 s) and 1.2 V (30 s)	21	6
4	1.2 h at 1.3 V	23	7
5	250 cycles of 0.1 V (30 s) and 1.2 V (30 s)	38	11
6	1500 cycles of 0.4 V (3 s) and 1.3V (3 s) at 50% RH	65	19
7	100 cycles of 0.1 V (30 s) and 1.25 V (30 s)	66	19
8	1500 cycles of 0.4 V (3 s) and 1.3V (3 s)	87	25
9	2500 cycles 0.4 V (3 s) - 1.3 V (3 s)	100	28
10	2000 cycles 0.6 V (3 s) - 1.3 V (10 s)	123	35
11	4000 cycles 0.4 V (3 s) - 1.3 V (3 s)	130	37
12	24 h at 1.3 V	186	53

First, sliding contact angles were measured but the water droplet did not slide at even an tilt angle of 90° (the sample was vertical to the flat stage) for some MEAs, and therefore only static contact angles were compared in the study. The contact angles of gas diffusion media on the cathode side were measured to be 154.8° $\pm$ 0.3° for the pristine and 153.9° $\pm$ 2.4° for the sample after carbon loss of 87 $\mu g/cm^2$. The negligible change in wetting property of the gas diffusion media indicated that the ASTs did not appear to degrade the PTFE-contained gas diffusion media chemically or mechanically.[3, 4] Therefore, transport overpotentials observed in this study were mainly attributed to catalyst layers. The change in apparent contact angles was determined for CCLs after a wide range of carbon mass losses. In Figure 4-1, the apparent contact angles decreased with the extent of corrosion, which was represented by amount of carbon mass loss in the CCL. The BOL CCL was measured to exhibit an apparent contact angle (θ^*) of 143.7° $\pm$ 3.8°, which was marked as the value for zero carbon loss. The apparent contact angles decreased sharply at first followed by a plateau; and similar behavior was observed in its relation with % ECSA loss. After about 130 $\mu g/cm^2$ of carbon loss, the apparent contact angles fell sharply again. This second decrease appears to coincide with the possible collapse of the carbon support[5]. Álvarez et al. observed a decrease from 156° $\pm$ 2° to 102° $\pm$ 4° for Vulcan XC-72R after cycling between 0.6V and 1.4V for an overall period of 24 h in H_2SO_4 solution;[6] and similarly, Kangasniemi et al. reported a decrease from 147° $\pm$ 3° to 111° $\pm$ 7° for Vulcan coated with 10% Teflon after 120 h at 1.2V hold. In comparison, we observed the largest decrease in apparent contact angles from 143.7° $\pm$ 3.8° to 129.0° $\pm$ 2.1° after 6.7 h of square wave at 0.4V (3s) and 1.3V (3s). The shorter AST used in this study, compared to those used by Álvaro et al. and Kangasniemi et al., may account for the smaller decrease in the

apparent contact angles. The shorter protocols (less carbon loss) were chosen because the cells are of no practical use if their performances drop significantly below DOE's target of less-than-10% voltage drop.

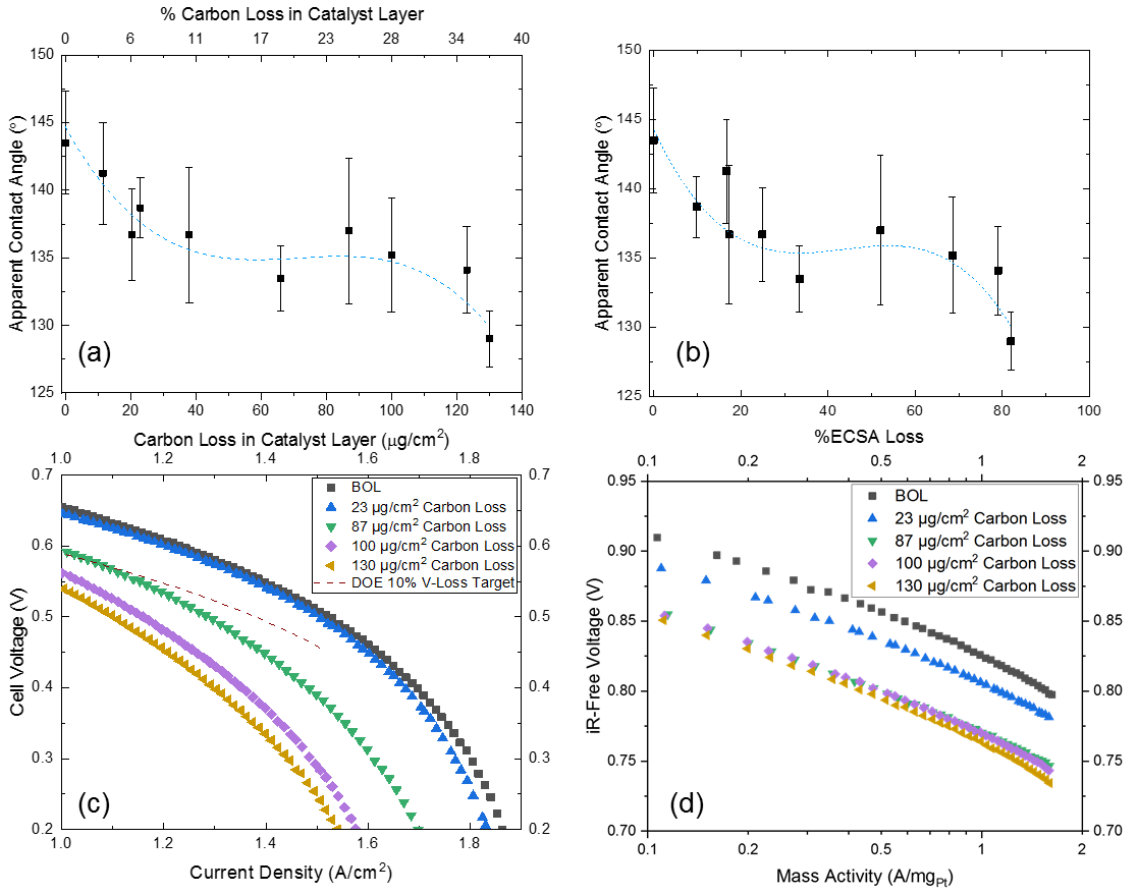

Figure 4-1 (a) Changes in apparent contact angles (θ*) of cathode catalyst layers with respect to carbon mass loss per active area. The error bars represent the standard deviations from at least four measurements. The blue dash line represents a polynomial fit and is used to guide the eyes. (b) Changes in apparent contact angles of CCL with respect to % ECSA loss with the same error bars and blue dash line as noted in (a). (c) Selected polarization curves in H2 | Air. (d) Tafel plots in H2 | Air.

In Figure 4-1b, the cell sustained its performance at medium-to-high current densities after about 23 μg/cm^2 carbon loss (7% total cathode carbon). Although the percent of carbon mass loss was close to 10%, which had been reported to lead to unacceptable performance loss, the high Pt loading and small ECSA change (9% decrease) accounted

for the sustained performance. The cell fell below the DOE's 10% target after 87 μg/cm^2 carbon loss (25% total cathode carbon), and the decrease in cell performance slowed down after further carbon loss. The Tafel plot in Figure 4-1c shows a 20 mV voltage drop from the BOL MEA after 23 μg/cm^2 carbon loss, whereas the difference in the voltages over the current range of 1 A/cm^2 to 1.5A/cm^2 in Figure 4-1b is less. The smaller difference resulted from an approximately 5% less ohmic resistance of the MEA after 23 μg/cm^2 carbon loss. The Tafel plot shows a further 30 mV voltage drop from 23 μg/cm^2 to 87 μg/cm^2, whereas the polarization curves exhibit greater voltage drop in the high current densities. The disparity implied a large amount of carbon support loss led to pore closures or other changes in pore structure, which increased the mass-transfer polarizations.

4.2 Fitting of Surface Texture Models

To examine whether the surface texture was the main cause of the decrease in apparent contact angles, Wenzel's and Cassie-Baxter's models were employed. First, the surface roughness for each CCL was taken from at least two AFM images. Some portions of images appeared to be artificial plateaus/valleys, because the AFM cantilever was not designed for sudden large height variations in more than a micron. However, the actual catalyst layer features can be several microns.[7] Figure 4a shows that the surface roughness decreased after carbon corrosion. Between 87 μg/cm^2 and 123 μg/cm^2 of carbon loss, the roughness values were within their uncertainties. Figure 4b shows a proposed mechanism in which the accelerated stress tests caused the interconnected pores to decrease, and the decrease can be accelerated by the cell hardware compression.[8, 9] The decrease in porosity can be discerned from the larger agglomerates in the AFM image of the sample after 130 μg/cm^2 as well as from the FIB-SEM and mass-balance porosity data. In addition, the decrease in

porosity was seen from the pores approximately 100 nm in diameter spreading on a relatively flat surface of the BOL catalyst layer, whereas the pore sizes were roughly 80 nm in diameter circled in white of the sample with 130 µg/cm^2 carbon loss shown in Figure 4a.

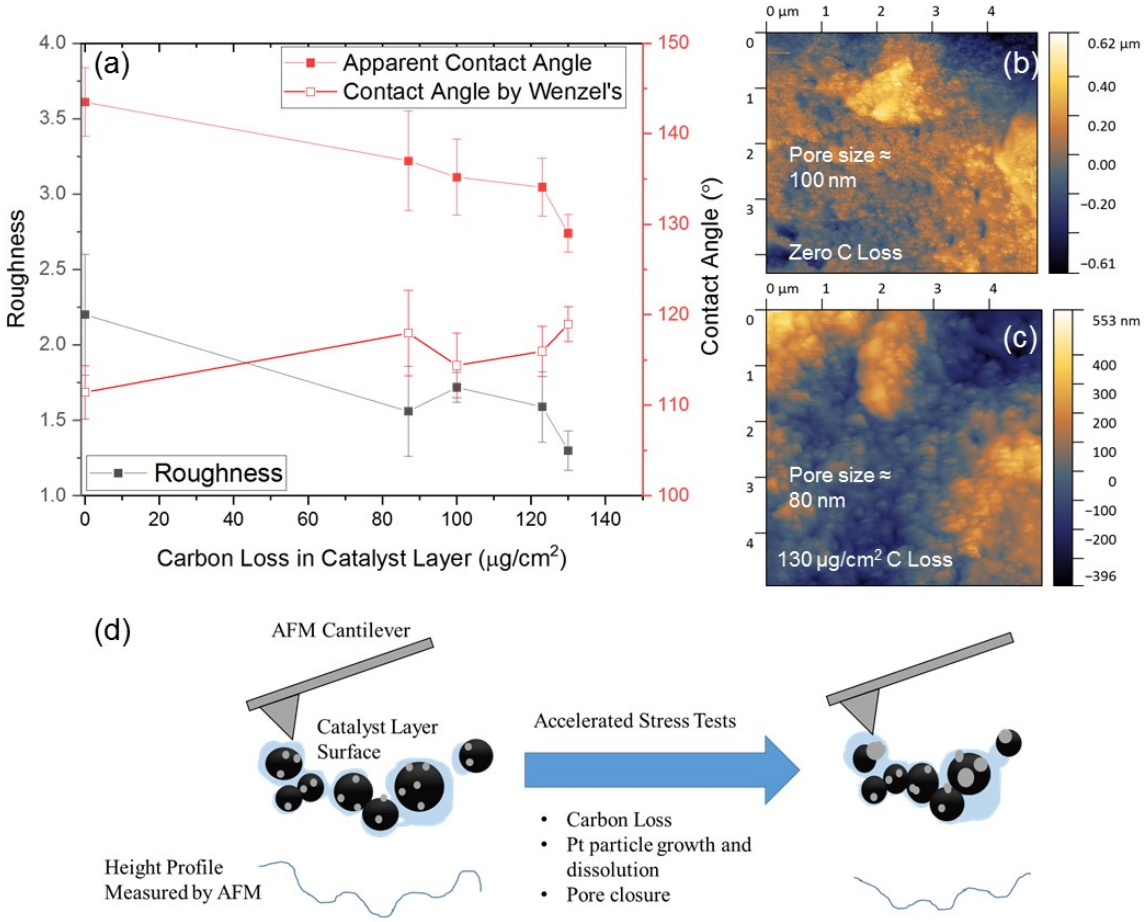

Figure 4-2 (a) Changes in surface roughness and contact angles as a function of cathode catalyst carbon loss (b) an AFM image of the surface of the beginning-of-life CCL, (c) an AFM image of the surface of a CCL after extensive carbon corrosion, and (d) an illustration of the changes in height profile after accelerated stress tests.

Using the apparent contact angle measurements, the roughness value, and the Wenzel's mode shown in equation (2.2), Young's contact angles, θ_c, were calculated. These angles were found to increase from 111° for the BOL CCL to 119° for the CCL sample with 130 µg/cm^2 carbon loss. The calculated Young's contact angles were similar to the contact angle of pure PTFE sheet. The increase in calculated Young's contact angles, which indicate the

microstructure-free contact angles of the CCLs, can be explained by the loss of the hydrophilic component, the carbon support, whose contact angle is less than 90° as reported by other researchers.[10, 11] The contact-angle measurements of compressed carbon black pellets were performed. Once a water droplet was applied, the pellets quickly absorbed the water and swelled, leaving no measurable water on the surface of the pellets. Hence, we were unable to record the contact angle of a carbon black pellet, but we confirmed that the carbon black (Vulcan) was hydrophilic. For the carbon loss, 100 µg/cm^2 represented a 10 wt% loss of the total cathode catalyst layer and a significant 28% of the total carbon mass in the catalyst layer, whereas the losses of ionomer[12] and Pt were smaller.[13] The small or negligible amount of ionomer loss was observed from unchanged XPS C-F peak intensities (near binding energy of 293 eV) shown in Figure 4-3a.

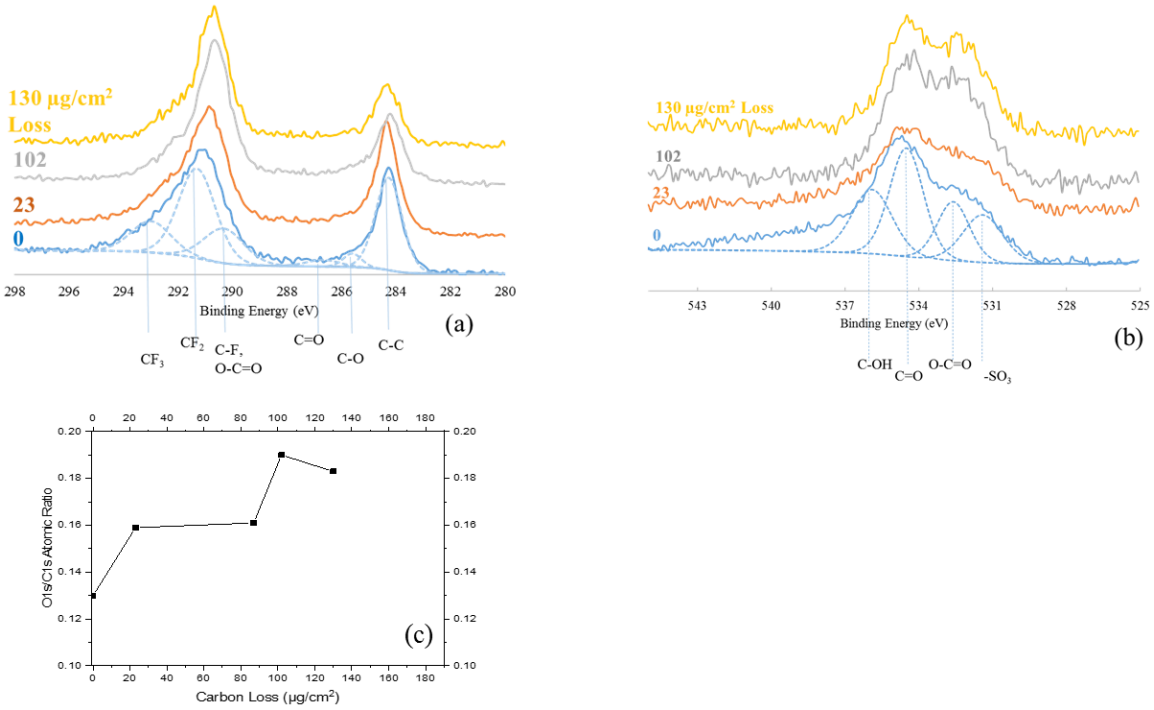

Figure 4-3 (a) Carbon 1s spectra of selected CCLs, (b) oxygen 1s spectra of selected CCLs and peak deconvolutions in XPS, and (c) atomic ratio of oxygen-to-carbon detected by XPS vs. carbon mass loss.

On the other hand, calculations using Cassie-Baxter's model showed that Young's contact angles decreased by 17% and 12% using the porosity values by FIB-SEM and the mass-balance approaches, respectively, as shown in Figure 4-4a. An image of FIB-SEM and its reconstructed image are shown in Figure 4-4b and c. The BOL porosity was calculated after reconstructions of approximately 100 such FIB-SEM images. Since the porosity of catalyst layer was obtained from the top few microns (the surface of CCL in contact with gas diffusion media) in the through-plane direction, it was approximated as the void space for the catalyst layer surface. It is worth noting that despite an increase in the porosity after small amount of carbon corrosion, the calculated contact angle by the FIB-SEM approach still decreased. The increase in porosity in FIB-SEM after initial carbon corrosion can be attributed to the carbon loss without pore closure. That is, it was likely that the after mild carbon corrosion, the ionomer/binder preserved the remaining structure of the electrode such that the porosity increased. The previous study suggested that the FIB-SEM approach cannot include the porosity of interior amorphous carbon that were preferentially corroded, but the mass-balance approach accounted for inter- and intra-particle hollowing.[9] Hence the porosities by FIB-SEM were lower than those by the mass-balance approach. In contrast to the increased Young's contact angle using Wenzel's model, the decrease in Young's contact angles by porosity indicated reduced hydrophobicity, and this may result from 1) increased surface oxide content and 2) degradation of the ionomer or PTFE binder.[12]

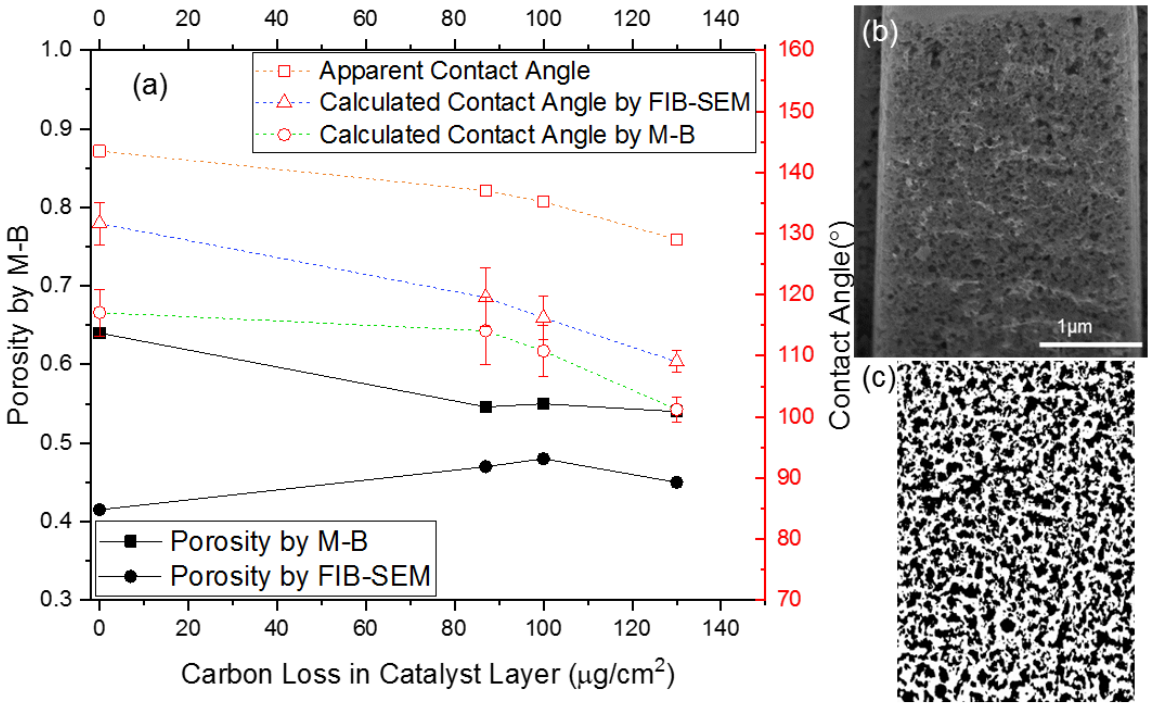

Figure 4-4 (a) Young's contact angles calculated by Cassie-Baxter's model with porosity data obtained from mass balance (M-B) and focused-ion-beam scanning electron microscopy (FIB-SEM).[9] (b) A FIB-SEM image of a catalyst layer after 87 μg/cm^2 carbon loss with SEM parameters: voltage of 4kV and 1.6 nA and FIB parameters: 30 kV and 10 pA. (c) A reconstructed image in a size of 4.33 μm x 2.39 μm for part of the FIB-SEM image.

First, the O_{1s}/C_{1s} ratio increased as shown in Figure 4-3c. The ratio increased from 0.13 for BOL to 0.16 after a small amount of 23 μg/cm^2 carbon loss and increased at slower rates with further carbon loss. The increase in surface oxide content was also observed in the increased O-C=O intensity in the oxygen spectra as shown in Figure 4-3a. Further oxidation of the O-C=O would be released as CO_2 gas. The O/C ratio appeared to reach its plateau after about 100 μg/cm^2 carbon loss, because electrochemical oxidation may continue to occur deeper below the outer surface but the XPS cannot detect the sample a few nanometer below the surface. Figure 4-4shows continuing decreases in Young's contact angle after 87 μg/cm^2 carbon loss using both FIB-SEM and mass-balance porosity data. In Figure 4-5, the smallest Young's contact angles were found using the combined

method. When using the combined model, the calculated Young's contact angles showed minor variations using either MB or FIB-SEM porosities, whereas the surface O/C ratio increased by 40% from the BOL. Hence, the increase in surface oxides after ASTs may alter the surface chemistry of the catalyst layer, but the increase in surface O/C ratio was unlikely to be the main reason for the change in Young's contact angles.

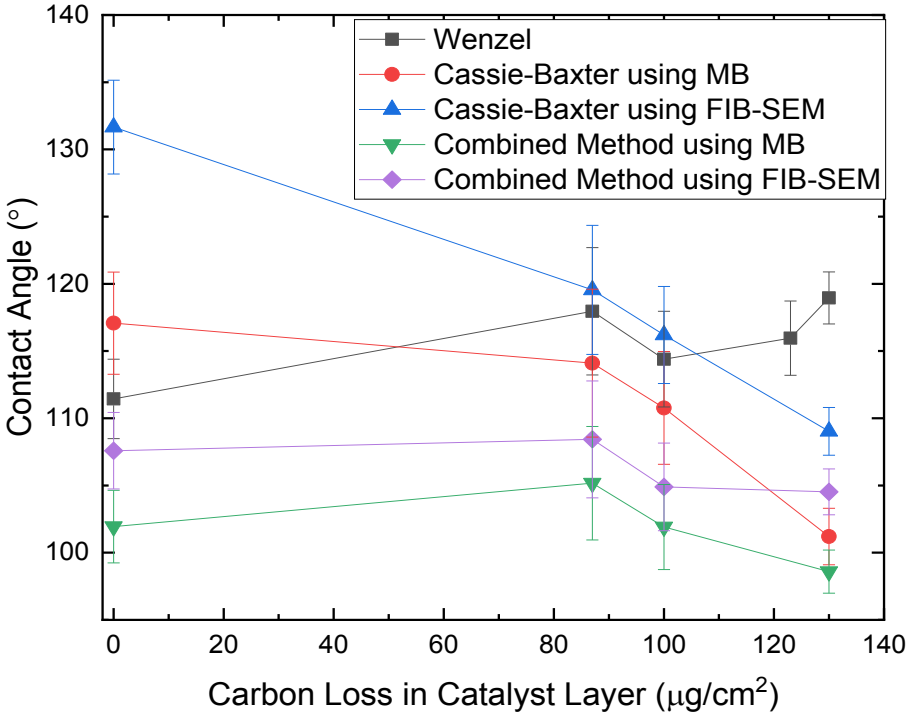

Figure 4-5 Young's contact angles using Wenzel's, Cassie-Baxter's, and a model combining the two. The last two models used porosity data from both mass balance approach and FIB-SEM approach.

A second hypothesis was that degradation of the ionomer via main chain unzipping caused a decrease in apparent contact angles. The fluorine/sulfur ratio of the catalyst layer from XPS was examined. If the ratio decreased, Cassie-Baxter's model would agree with the decrease in Young's contact angle because fluorine resides mostly in the backbone of the ionomer in the catalyst layer. If the fluorine was released significantly, the main chain unzipping would reduce the hydrophobicity of the catalyst layer, leading to a reduced contact angle. However, the BOL CCL showed an F/S ratio of 58 and the F/S ratio

remained the same (between 57 and 59) for the corroded samples. Therefore, the use of Cassie-Baxter's model appeared insufficient and Wenzel's model or the combined model yielded better estimate of the Young's contact angle. The increased Young's contact angles (from 111° to 119°) using Wenzel's model and relatively constant Young's contact angles (from 107° to 105°) using the combined model suggested that despite the reduced apparent contact angle, the cathode catalyst layers sustained the high degree of hydrophobicity when subjected to these ASTs.

In summary, the Wenzel's and Cassie-Baxter's models exhibited opposite trends of inherent wettability of catalyst layers after carbon corrosion and the combined model showed sustained hydrophobicity after carbon corrosion. The additional analysis of surface chemistry with surface geometry do not support the hypothesis that the reduced performance at high current densities can be ascribed to reduced hydrophobicity and greater liquid saturation of the pore structure, before the cell significantly fell below the DOE's 10% target. For future studies, one can consider placing the goniometer inside a humidity box that controls the relative humidity and temperature. In this study, the ambient relative humidity and temperature, with which the MEAs were equilibrated before contact angle measurements, were not controlled. The differences in pre-equilibrated relative humidities or temperatures in the room may have contributed to the large noise-to-signal ratios. In addition, the humidity box with controlled environment can account for the high hydration of ionomer in the catalyst layers, as fuel cells are typically operated at higher relative humidities than the ambient.

4.3 Conclusions

A variety of ASTs were applied to PEM fuel cells made with commercial MEAs and the apparent contact angles were measured over a broad range of carbon mass losses in the cathode. The wetting property of the cathode catalyst layers was investigated via static contact angles coupled with microstructural changes. In Wenzel's model, the Young's contact angle became hydrophobic due to the loss of hydrophilic carbon support. On the other hand, the continuing decreased Young's contact angle after 87 $\mu g/cm^2$ using Cassie-Baxter's model did not correlate well with the plateaued surface oxide content or the constant F/S ratio. Neither the surface oxide nor the ionomer backbone unzipping reflected by the F/S ratio was the main cause for decreased Young's contact angles. The combined model for both roughness and porosity also showed sustained hydrophobicity after up to 130 $\mu g/cm^2$ (37% loss of carbon in the cathode). Therefore, it was more accurate to use surface roughness and Wenzel's model to probe changes in inherent wetting property, which was affected not only by surface oxide content but also by cathode morphology.

The results of sustained hydrophobicity in CCLs suggested the microstructural collapse did not occur to cause a significant change in the wettability of the CCLs until the cell performance fell far below DOE's 10% target. The results also suggested the need to investigate the effect of changes in ionomer distribution and coverage in the catalyst layer on mass-transfer polarization after carbon corrosion, because ionomer weight percentage increases in the catalyst layer as seen in the higher intensity of C-F peak than C-C peak after carbon corrosion.

4.4 References

1. DOE, U.S. Department of Energy Annual Merit Review Proceedings, 2016.

2. R. Mukundan, G. James, J. Davey, D. Langlois, D. Torraco, W. Yoon, A. Z. Weber, and R. Borup, *ECS Transactions,* **41** (1), 613-619 (2011).

3. R. J. F. Kumar, V. Radhakrishnan, and P. Haridoss, *International Journal of Hydrogen Energy,* **37** (14), 10830-10835 (2012).

4. Y. Jiang, J. Hao, M. Hou, H. Zhang, X. Li, Z. Shao, and B. Yi, *RSC Advances,* **5** (126), 104095-104100 (2015).

5. J. D. Fairweather, D. Spernjak, A. Z. Weber, D. Harvey, S. Wessel, D. S. Hussey, D. L. Jacobson, K. Artyushkova, R. Mukundan, and R. L. Borup, *Journal of The Electrochemical Society,* **160** (9), F980-F993 (2013).

6. G. Álvarez, F. Alcaide, O. Miguel, P. L. Cabot, M. V. Martínez-Huerta, and J. L. G. Fierro, *Electrochimica Acta,* **56** (25), 9370-9377 (2011).

7. F. E. Hizir, S. O. Ural, E. C. Kumbur, and M. M. Mench, *Journal of Power Sources,* **195** (11), 3463-3471 (2010).

8. H. Schulenburg, B. Schwanitz, N. Linse, G. n. G. Scherer, A. Wokaun, J. Krbanjevic, R. Grothausmann, and I. Manke, *The Journal of Physical Chemistry C,* **115** (29), 14236-14243 (2011).

9. A. G. Star and T. F. Fuller, *Journal of The Electrochemical Society,* **164** (9), F901-F907 (2017).

10. M. L. Studebaker and C. W. Snow, *The Journal of Physical Chemistry,* **59** (9), 973-976 (1955).

11. K. Kinoshita and J. A. S. Bett, *Carbon,* **13** (5), 405-409 (1975).

12. A. Kusoglu and A. Z. Weber, *Chemical Reviews,* (2017).

13. J. Wang, G. Yin, Y. Shao, S. Zhang, Z. Wang, and Y. Gao, *Journal of Power sources,* **171** (2), 331-339 (2007).

CHAPTER 5. LITERATURE REVIEW ON CARBON SUPPORT FUNCTIONALIZATION AND IONOMER COVERAGE

5.1 Three Schemes of Surface Functionalization for Carbon Support

At ultra-low platinum loadings for cathodes (≤ 0.1 mg cm^{-2}), researchers have reported larger than expected mass-transfer resistances at high current densities.[1-3] Common theories for the reasons behind the high mass-transport resistance include oxygen dissolution kinetics,[2] large local interfacial resistances,[3, 4] and adsorption of the sulfonic acid group from the electrolyte onto Pt that reduces the activity for oxygen reduction.[1]

Doping and surface functionalization are two major approaches to modify the properties of carbon materials.[5] The treatment of carbon materials, such as carbon black, highly oriented pyrolytic graphite (HOPG),[6] carbon nanotubes,[7] and graphene,[8] by nitrogen dopants has been demonstrated. The functionalization changes the surface chemistry of carbon support materials for electrocatalysts with nitrogen-containing functional groups or molecules rather than introducing atomic impurities into the carbon support in the doping process.[9-14] However, during the surface functionalization processes, the atomic impurities such as pyridinic and pyrrolic nitrogen can be incorporated into the graphite layers of the carbon support.[14] The atomic nitrogen impurities are beneficial to electrocatalysts; for example, pyridinic nitrogen can increase electron donation from the functionalized carbon support to Pt particles and thus increase the mass activity.[7, 15] The surface functionalization has been performed with ammonia,[13, 15-17] para-phenylenediamine (pPDA),[11] benzimidazole,[12] ethylenediamine,[18] melamine,[19] and aniline.[20, 21] The surface functionalization may impact the electrocatalyst/support through 1) dispersion: modified nucleation and growth kinetics during catalyst nanoparticle deposition,[22] 2) durability:

enhanced electrocatalyst/support chemical binding,[23] 3) catalytic activity: the modified electronic structure of electrocatalyst nanoparticle.[9] While these kinetic effects of surface functionalization with nitrogen species are extensively studied, the reports on effects of surface functionalization on mass transport are limited.

Recent reports have shown that the surface functionalization (grafting positive functional groups) of carbon support affects the uniformity of ionomer (negative-charged sulfonate groups) distribution on the carbon support, which may further affect the mass-transfer resistance.[11, 13, 24, 25] Yang *et al*. determined a larger ionomer/carbon aggregate size after diazonium reaction of pPDA and a smaller size after diazonium reaction of sulfanilic acid due to their different surface charges. However, no full cell test was conducted to examine the effect of the functionalization on mass transfer.[11] Xin *et al.* found improved performance of MEAs made with carbon support after sulfanilic acid at low relative humidity.[26] Orfanidi *et al*. found reduced mass-transport polarization after ammonia functionalization; however, the study lacks a comparison surface functionalization to validate the beneficial effect of the ammonia functionalization.[13] Current literature has limited comparison studies on the differences in responses to surface functionalization by different types of carbon support and their corresponding full cell performance and durability.[24]

5.2 Ionomer Characterization

There is a strong need for visualization of changes in ionomer distribution after surface functionalization. To visually determine the ionomer coverage and distribution in a catalyst layer before and after surface functionalization of carbon support, the relevant techniques include direct imaging using transmission electron microscopy (TEM) or Scanning

Transmission Electron Microscopy (STEM),[22, 27] staining technique for direct imaging using TEM/STEM,[28, 29] TEM/STEM coupled with Energy Dispersive X-ray Spectroscopy (EDS),[30-32] STEM coupled with electron energy loss spectroscopy (EELS),[31, 33, 34] and Scanning Transmission X-ray Microscopy (STXM).[34-36] The direct imaging of ionomer on Pt/C using TEM/STEM requires nanometer spatial resolution and low acceleration voltage (about 80 kV). Park *et al.* used STEM to study ionomer coverage and traced the edge of 1 to 2 nm thick in TEM images as the ionomer.[22] Lee *et al*. found incomplete coverage of ionomer on the carbon support using TEM.[27] For direct imaging, researchers also employed staining method to enhance the contrast between carbon support and ionomer, the latter of which also contains carbon.[28, 29] Lopez-Haro *et al.* determined a 7 nm on average ionomer thickness of Cs-stained sample using STEM imaging.[28] However, the staining method typically requires Pt-free samples to avoid the low contrast between the Pt and Cs under electron microscopy and thus it cannot image a sample directly cut from a catalyst layer of an MEA.

Researchers also used STEM coupled with EDS or EELS to determine ionomer dispersion in the catalyst layers.[30, 31] More et al. mapped fluorine to represent ionomer dispersed in catalyst layers in 3D at the nm-scale using STEM coupled with EDS,[30] and Cullen *et al.* found an agreement between the EDS-determined I/C ratio (0.964) and the experimentally prepared I/C ratio (1.00).[31] They concluded that EDS is suitable for quantitative analysis of ionomer distribution at low resolution whereas EELS can only be used as a qualitative analysis of ionomer distribution.[31] Sulfur is another element present in the sulfonic acid groups in the Nafion ionomer; however, sulfur cannot be distinctively mapped by EDS because it overlaps with higher-order Pt spectra peaks. Another limitation

of the high-energy-electron technique is the radiation damage that can cause bond breaking, free radical formation, crosslinking, and eventually formation of amorphous carbon.[31, 34] De A Melo et al. determined an I/C volume ratio less than 0.01 using EELS for the experimentally prepared 1.0 I/C volume ratio, indicating significant radiation damage using EELS.[34]

5.3 References

1. T. A. Greszler, D. Caulk, and P. Sinha, *Journal of The Electrochemical Society,* **159** (12), F831-F840 (2012).

2. H. Liu, W. K. Epting, and S. Litster, *Langmuir,* **31** (36), 9853-9858 (2015).

3. A. Z. Weber and A. Kusoglu, *Journal of Materials Chemistry A,* **2** (41), 17207-17211 (2014).

4. A. Kongkanand, N. P. Subramanian, Y. Yu, Z. Liu, H. Igarashi, and D. A. Muller, *ACS Catalysis,* **6** (3), 1578-1583 (2016).

5. Y. Park, J. Yoo, B. Lim, W. Kwon, and S.-W. Rhee, *Journal of Materials Chemistry A,* **4** (30), 11582-11603 (2016).

6. J. F. Evans and T. Kuwana, *Analytical Chemistry,* **51** (3), 358-365 (1979).

7. R. Chetty, S. Kundu, W. Xia, M. Bron, W. Schuhmann, V. Chirila, W. Brandl, T. Reinecke, and M. Muhler, *Electrochimica Acta,* **54** (17), 4208-4215 (2009).

8. X. Wang, X. Li, L. Zhang, Y. Yoon, P. K. Weber, H. Wang, J. Guo, and H. Dai, *Science,* **324** (5928), 768-771 (2009).

9. Y. Zhou, K. Neyerlin, T. S. Olson, S. Pylypenko, J. Bult, H. N. Dinh, T. Gennett, Z. Shao, and R. O'Hayre, *Energy & Environmental Science,* **3** (10), 1437-1446 (2010).

10. Y. Zhou, R. Pasquarelli, T. Holme, J. Berry, D. Ginley, and R. O'Hayre, *Journal of Materials Chemistry,* **19** (42), 7830-7838 (2009).

11. F. Yang, L. Xin, A. Uzunoglu, Y. Qiu, L. Stanciu, J. Ilavsky, W. Li, and J. Xie, *ACS applied materials & interfaces,* **9** (7), 6530-6538 (2017).

12. Z.-F. Li, L. Xin, F. Yang, Y. Liu, Y. Liu, H. Zhang, L. Stanciu, and J. Xie, *Nano Energy,* **16** 281-292 (2015).

13. A. Orfanidi, P. Madkikar, H. El-Sayed, G. Harzer, T. Kratky, and H. Gasteiger, *Journal of The Electrochemical Society,* **164** (4), F418-F426 (2017).

14. G. Bae, D. H. Youn, S. Han, and J. S. Lee, *Carbon,* **51** 274-281 (2013).

15. S. Roy, A. Harding, A. Russell, and K. Thomas, *Journal of the Electrochemical Society,* **144** (7), 2323-2328 (1997).

16. R. Jansen and H. Van Bekkum, *Carbon,* **32** (8), 1507-1516 (1994).

17. S. Ott, A. Orfanidi, H. Schmies, B. Anke, H. N. Nong, J. Hübner, U. Gernert, M. Gliech, M. Lerch, and P. Strasser, *Nature Materials,* **19** (1), 77-85 (2020).

18. W. S. Jung and B. N. Popov, *Carbon,* **122** 746-755 (2017).

19. X. Wang, F. Zhang, Y. Liu, and Z. Wang, *Journal of The Electrochemical Society,* **165** (15), J3052-J3058 (2018).

20. H. Lee, Y.-E. Sung, I. Choi, T. Lim, and O. J. Kwon, *Journal of Power Sources,* **362** 228-235 (2017).

21. T. Kim, T. Xie, W. S. Jung, and B. N. Popov, *International Journal of Hydrogen Energy,* **42** (17), 12507-12520 (2017).

22. Y.-C. Park, H. Tokiwa, K. Kakinuma, M. Watanabe, and M. Uchida, *Journal of Power Sources,* **315** 179-191 (2016).

23. L. Xin, F. Yang, S. Rasouli, Y. Qiu, Z.-F. Li, A. Uzunoglu, C.-J. Sun, Y. Liu, P. Ferreira, and W. Li, *ACS Catalysis,* **6** (4), 2642-2653 (2016).

24. G. S. Harzer, A. Orfanidi, H. El-Sayed, P. Madkikar, and H. A. Gasteiger, *Journal of The Electrochemical Society,* **165** (10), F770-F779 (2018).

25. L. Xin, Y. Kang, F. Yang, A. Uzunoglu, T. Rockward, P. J. Ferreira, R. L. Borup, J. Ilavsky, L. Stanciu, and J. Xie, *in* "Meeting Abstracts", p. 2584-2584. The Electrochemical Society, 2016.

26. L. Xin, F. Yang, J. Xie, Z. Yang, N. N. Kariuki, D. J. Myers, J.-K. Peng, X. Wang, R. K. Ahluwalia, and K. Yu, *Journal of The Electrochemical Society,* **164** (6), F674-F684 (2017).

27. M. R. Lee, H. Y. Lee, S. D. Yim, C. S. Kim, Y. G. Shul, A. Kucernak, and D. Shin, *Fuel Cells,* (2018).

28. M. Lopez-Haro, L. Guétaz, T. Printemps, A. Morin, S. Escribano, P.-H. Jouneau, P. Bayle-Guillemaud, F. Chandezon, and G. Gebel, *Nature communications,* **5** (2014).

29. L. Guetaz, M. Lopez-Haro, S. Escribano, A. Morin, G. Gebel, D. A. Cullen, K. L. More, and R. L. Borup, *ECS Transactions,* **69** (17), 455-464 (2015).

30. K. L. More, *Department of Energy Fuel Cell Annual Report,* (2016).

31. D. A. Cullen, R. Koestner, R. Kukreja, Z. Liu, S. Minko, O. Trotsenko, A. Tokarev, L. Guetaz, H. Meyer, and C. Parish, *Journal of The Electrochemical Society,* **161** (10), F1111-F1117 (2014).

32. M. Schulze, M. v. Bradke, R. Reissner, M. Lorenz, and E. Gülzow, *Fresenius' journal of analytical chemistry,* **365** (1-3), 123-132 (1999).

33. D. A. Cullen, M. Lopez-Haro, P. Bayle-Guillemaud, L. Guetaz, M. Debe, and A. Steinbach, *Journal of Materials Chemistry A,* **3** (21), 11660-11667 (2015).

34. L. G. de A. Melo, A. P. Hitchcock, V. Berejnov, D. Susac, J. Stumper, and G. A. Botton, *Journal of Power Sources,* **312** 23-35 (2016).

35. D. Susac, V. Berejnov, A. P. Hitchcock, and J. Stumper, *ECS Transactions,* **41** (1), 629-635 (2011).

36. A. Hitchcock, J. Wu, V. Lee, N. Appathurai, T. Tyliszczak, H.-W. Shiu, D. Shapiro, V. Berejnov, D. Susac, and J. Stumper, *Microscopy and Microanalysis,* **22** (S3), 1290-1291 (2016).

CHAPTER 6. EXPERIMENTAL METHODS FOR FUNCTIONALIZATION STUDY

In this study, three different schemes of surface functionalization using three types of carbon support (Vulcan, Ketjen black, and a proprietary carbon X) were investigated, and the effects of this functionalization on the cell performance are reported. STEM images and EDS elemental maps were used to analyze the changes in ionomer surface coverage in the catalyst layer due to surface functionalization of carbon support. Lastly, the impact of surface functionalization on the durability of carbon support was examined following DOE's accelerated stress test (AST) protocols.

6.1 Carbon Functionalization and Verification

Carbon supports tested in this study include Vulcan XC-72R (Cabot Corporation), Ketjen black EC-600JD (Fitz Chem Corporation), and a specialty carbon support, X (Kolon Industries). A description of the reaction routes to the different schema for functionalization is shown in Figure 6-1. In scheme 1, a diazonium reaction, 400 mg of carbon support was dispersed in a solution containing 400 mL of deionized water, 56 mg of para-phenylenediamine (pPDA) (≥ 97%, VWR), and 56 μL of concentrated nitric acid. After sonicating and stirring for 2 hours, 37 mg of $NaNO_2$ (Reagent Grade, VWR), which was previously diluted in 2 mL of DI water, was added to the carbon support mixture dropwise to minimize the side reaction of $NaNO_2$ with pPDA. The mixtures with Vulcan and Ketjen Black were held at 70 °C overnight, whereas the mixture with carbon support X sat for 24 hours due to its lower reactivity. In scheme 2, the pre-oxidation step was carried out by heating 400 mg of carbon support in a 60 mL 30% HNO_3 solution under reflux for 4 hours. A batch of carbon support X was pre-oxidized in 50% HNO_3 for 6 hours.

The pre-oxidized carbon support was then filtered, dried, and reacted with pure NH_3 gas at 50 sccm flow rate in a tube furnace at 200 °C for 4 or 6 hours for carbon support X. Scheme 3 was identical to scheme 1 except that the 56 mg pPDA was replaced by equal molar amount (90 mg) of 4-aminobenzene sulfonic acid (sulfanilic acid) (Reagent Grade, VWR).

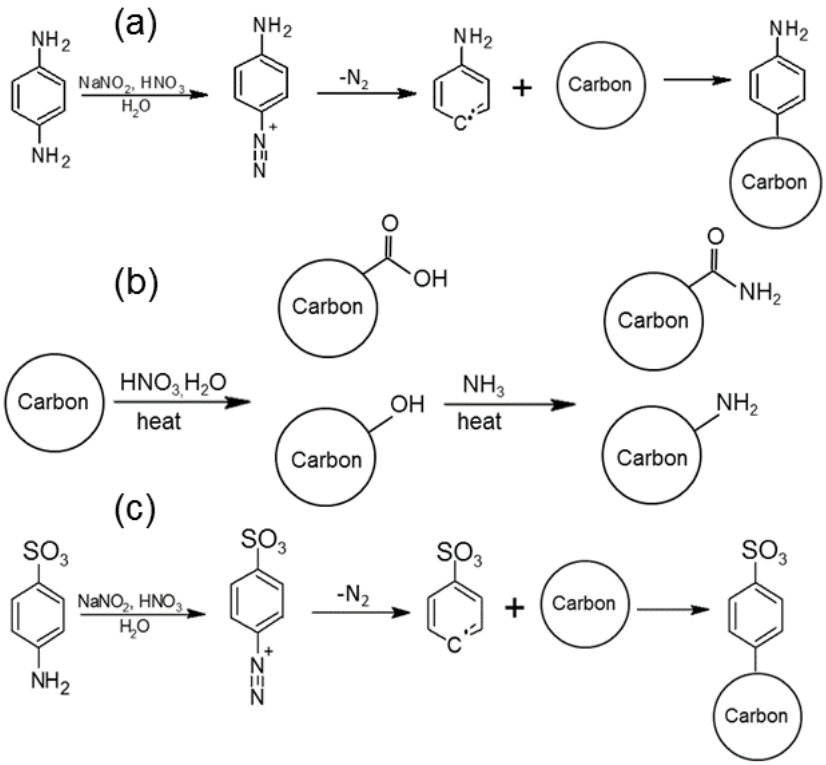

Figure 6-1 (a) Scheme 1 diazonium reaction with para-phenylenediamine for creating positive surface charge in solution, (b) scheme 2 amination for creating positive surface charge, and (c) scheme 3 diazonium reaction with sulfanilic acid for generating negative surface charge.

The following techniques were used to verify and characterize the surface functional groups on carbon black: X-ray photoelectron spectroscopy (XPS) (Thermo K-Alpha XPS, Thermo Fisher Scientific), nitrogen physisorption for Brunauer-Emmett-Teller (BET) surface area and Barrett-Joyner-Halenda (BJH) adsorptive pore volumes (ASAP 2050 analyzer, Micromeritics), contact angle measurement (Model 250 goniometer, ramé-hart instrument), zeta potential (Zetasizer Nano ZS, Malvern Panalytical), and X-ray diffraction (X'Pert Pro Alpha-1, Panalytical). The XPS instrument was equipped with a

monochromatic Al Kα X-ray source (hv =1486.6 eV) and the analysis chamber was 5e-8 mbar or lower. The survey scan was at 160 eV, and the high-resolution was at 40 eV. In BET tests, about 100 mg of sample was measured out each time and degassed at 200 °C for 18 h prior to the adsorption experiment. For contact angle measurements, 12 mg carbon support and 20 mg 60 wt% PTFE solution (50 wt% PTFE in the solid) were mixed in 5 mL DI water/IPA (volume: volume = 4:1). A drop of the mixture was added to a clean glass slide and dried and repeated for a total of 0.5 mL of the mixture. The samples for zeta-potential measurements were prepared by dissolving 1 mg carbon support in 10 mL DI water. X-ray diffraction (XRD) was performed on carbon support or Pt-deposited carbon support powder in ambient environment. 2Theta was measured from 17° to 90° at a step size of 0.32° and at a scan rate of 1 min per step.

6.2 Pt Synthesis and MEA Fabrication

The Pt nanoparticle synthesis was based on the "unprotected" colloidal method by Wang et al.[1] 95.3 mg of carbon support was mixed in 95 mL ethylene glycol, which acted as both a solvent and a reducing agent, for 2 h. The pH of the solution was increased to 11 by adding 0.17 mL of 2 M NaOH. In order to obtain 20 wt% Pt/C catalyst, 0.589 mL of 8 wt% H_2PtCl_6 solution was then added to the mixture and stirred at room temperature overnight. The reaction was carried out at 160 °C for 3 h. Anode catalyst inks were made of 5% Nafion 212 solution, commercial TKK 20% Pt/Vulcan with ionomer/carbon weight ratio = 0.66, DI water, and IPA. Cathode catalyst inks were made of the same ionomer solution and solvents with in-lab made 20 wt% catalysts. The catalyst inks were coated on Nafion 211 membrane via a direct spray-coating method to create a 4.8 cm^2 active area.

The Pt loadings were kept at 0.1 mg/cm^2 for both anode and cathode, unless otherwise noted.

6.3 Fuel Cell Materials and Operation

The cells were assembled with TGP-H-060 Toray carbon paper with 5% wet proofing as gas diffusion media (Fuel Cell Store), and 152 μm (6 mil nominal) PTFE sheets as gaskets (McMaster-Carr). The cell hardware was triple serpentine Poco graphite flowfields that were fastened to a torque of 5.0 N-m (Fuel Cell Technologies). The cells were tested on a Scribner 850e with a model 880 frequency response analyzer. The cells were wet-up for an hour and broke in by sixty cycles on hydrogen and air. Each cycle consisted of being held at 0.6 V for 1 min, open-circuit voltage (OCV) for 30 s, and then 0.3V for 1 min.

The H_2/air polarization curves and electrochemical impedance spectroscopy were performed at differential conditions (2 SLPM H_2 | 5 SLPM Air, 80 °C, 100% RH, 150 kPa_{abs} back pressure). The H_2 cross-over test was performed (0.2 SLPM H_2/0.1 SLPM N_2, 80°C, 100% RH) from 0.08V to 0.4V at 1 mV/s. The electrochemical surface area (ECSA) was obtained from cyclic voltammetry from 0.05 V to 0.6 V at 20 mV/s (0.05 SLPM H_2/0.4 SLPM N_2, 80°C, 100% RH) using a Metrohm Autolab 302N potentiostat/galvanostat. The proton resistance in the catalyst layer was determined from H_2/N_2 impedance spectroscopy scanning from 10 kHz to 1 Hz (0.4 SLPM H_2/0.4 SLPM N_2, 80°C, 100% RH).[2] The limiting current measurement was performed using 4% O_2 in N_2 and mass-transfer resistance was calculated based on Baker's method.[3]

The accelerated stress tests were conducted following the protocols by DOE.[4] For carbon-specific corrosion, potential cycling between 1.0 V and 1.5 V at 0.5 V/s was used.

The carbon loss was determined from the cathode CO_2 exhaust and was recorded by a non-dispersive infrared detector (NDIR) (California Analytical Instruments model 601).

6.4 Limiting Current Analysis

The limiting current analysis for local transport resistance is based on Baker method. The total transport resistance is a function of gas pressure, as expressed by

$$R_{total} = \frac{4Fx_{O_2,dry}}{i_{lim}} \frac{(p - p_w)}{RT} \tag{6.1}$$

The total transport resistance can be divided into resistance in the flow channel, R^{ch}, the GDL, R^{GDL}, and the other, R^{other}

$$R_{total} = R^{ch} + R^{GDL} + R^{other} \tag{6.2}$$

After substituting the expression for each term, the total resistance becomes

$$R_{total} = \left[\frac{A^{ch}a}{D_{OM}} + B^{ch}\frac{2Nl^{ch}d^{ch}}{Q_{dry}}\left(\frac{273}{T}\right)\frac{p - p_w}{p_{atm}}\right] + \left[\frac{1}{D_{OM}}\left(f\ell^{GDL}\frac{D_{OM}}{D_{O_2}^{GDL}}\right)\right] + \left[\frac{A_{other}}{D_{OM}} + R_{P-I}\right] \tag{6.3}$$

where D_{OM} is the diffusion coefficient of the oxygen relative to the gas mixture in the flow channel, and other parameters are tabulated in . Since the limiting current technique was conducted at dilute concentrations of O_2, the diffusion coefficient of oxygen relative to the mixture gas can be approximated by Blanc's law

$$\frac{1}{D_{OM}} = \frac{1}{pD_{ON}}\left[p + p_w\left(\frac{D_{ON}}{D_{OW}} - 1\right)\right] \tag{6.4}$$

where the product pD_{ON} and ratio D_{ON}/D_{OW} are independent of the pressure, though each diffusivity coefficient are inversely related to the total pressure, p. When the total transport

resistance is plotted against the total pressure, the slope, $\frac{\partial R_{total}}{\partial p}$, and y-intercept are

$$\frac{\partial R_{total}}{\partial p} = B^{ch}\frac{2NL^{ch}d^{ch}}{Q_{dry}}\left(\frac{273.15}{T}\right) + \frac{1}{pD_{ON}}\left(aA^{ch} + f\ell^{GDL}\frac{D_{OM}}{D_{O_2}^{GDL}} + A^{other}\right) \tag{6.5}$$

$$intercept = R^{P-I} + \frac{p_W}{pD_{ON}}\left(\frac{D_{OM}}{D_{OW}} - 1\right)\left(aA^{ch} + fl^{GDL}\frac{D_{OM}}{D_{O_2}^{GDL}} + A^{other}\right) - B^{ch}\frac{2NL^{ch}d^{ch}}{Q_{dry}}\left(\frac{273.15}{T}\right) \tag{6.6}$$

The slope and the y-intercept are determined from the trend line. Therefore, the pressure-independent transport resistance, R_{P-I}, is calculated as

$$R_{P-I} = intercept - p_w\left(\frac{\partial R_{total}}{\partial p}\right)\left(\frac{D_{ON}}{D_{OW}} - 1\right) - \frac{p_w D_{ON}}{p_{atm}D_{OW}}B^{ch}\frac{2Nl^{ch}d^{ch}}{Q_{dry}}\left(\frac{273.15}{T}\right) \tag{6.7}$$

Table 6-1 Parameters used in limiting current analysis from literature and measurement

Symbol	Meaning	Value	Source
a	Half of the flow channel width	2.5E-4 m	Measured
$\boldsymbol{A^{ch}}$	Dimensionless coefficient, flow-rate-independent part of the channel transport resistance	1.12	Baker[3]
$\boldsymbol{A^{other}}$	Pressure-dependent part of the other transport resistance	Is not needed for the final R_{NP} calculation	Baker[3]
$\boldsymbol{B^{ch}}$	Dimensionless coefficient, flow-rate-dependent part of the channel transport resistance	1.01	Baker[3]
$\boldsymbol{d^{ch}}$	Channel depth	0.00075 m	Measured
$\boldsymbol{D_{ON}}$	Diffusivity of oxygen relative to nitrogen	$1.5*0.181(T/333.15)^{1.5}$ = 0.449 cm^2/s	Richard[5]
$\boldsymbol{D_{OW}}$	Diffusivity of oxygen relative to water vapor	$1.5*0.181(T/273.15)^{1.5}$ = 0.442 cm^2/s	Richard[5]
$\boldsymbol{f}$	Non-dimensional parameter, which is interpreted as a shape factor that converts the resultant mass flux for the anisotropic, two-dimensional diffusion to an	1.410	Baker[3]

	equivalent isotropic, one-dimensional term		
l^{ch}	Channel length	0.01865 m	Measured
N	Number of parallel channels	3	Measured
p_{atm}	Atmosphere pressure	101,325 Pa	Fact
p_W	Water saturation pressure at a particular temperature	-2846.4+411.24(T-273.15)-10.554(T-273.15)^2+.16636(T-273.15)^3= 47,684 Pa	Mench[6]
Q_{dry}	Inlet dry air flow rate in each channel	2.778e-5 m^3/s (5 L/min)	Measured
T	Cell temperature	353.15 K	Measured

6.5 Ionomer Imaging using STEM/EDS

The sample solution was prepared by mixing the electrocatalyst and ionomer at an I/C ratio of 0.66 for beginning-of-life samples and by scrapping off the cathode catalyst layer from an MEA after an AST. The materials were then dissolved in DI water/IPA (weight: weight = 1:1). The solution was sonicated and a drop of it was deposited on a copper grid. The high-angle annular dark-field (HAADF) STEM images were collected on Hitachi HD-2700 (200 kV) equipped with EDS. The field of view for STEM images was relatively large approximately 500 nm × 500 nm to minimize the radiation damage on the ionomer. Then EDS was measured on a smaller area of the STEM image for 7 min. The STEM/EDS imaging analysis include binarization and determination of fluorine pixel locations using ImageJ and selection of edge fluorine pixels based on Poisson's distribution using MATLAB (see A.2 Analysis and Calculations of Ionomer Coverage)

6.6 References

1. Y. Wang, J. Ren, K. Deng, L. Gui, and Y. Tang, *Chemistry of Materials,* **12** (6), 1622-1627 (2000).

2. K. Neyerlin, W. Gu, J. Jorne, A. Clark, and H. A. Gasteiger, *Journal of The Electrochemical Society,* **154** (2), B279-B287 (2007).

3. D. R. Baker, D. A. Caulk, K. C. Neyerlin, and M. W. Murphy, *Journal of The Electrochemical Society,* **156** (9), B991-B1003 (2009).

4. DOE, *Energy Efficiency & Renewable Energy* (2017).

5. T. Richard, *Calculating the Oxygen Diffusion Coefficient in Air*, Cornell (1996). http://compost.css.cornell.edu/oxygen/oxygen.diff.air.html

6. M. M. Mench. John Wiley & Sons, Inc, 2008.

CHAPTER 7. RESULT AND DISCUSSION OF FUNCTIONALIZATION STUDY

7.1 Carbon Support Functionalization

XPS was used to confirm occurrence of the surface functionalization. For scheme 1 functionalization, a reference sample was made by including all the starting materials except $NaNO_2$. The resulting XPS showed an absence of N, which confirmed that there was sufficient filtration and that the surface N content was unlikely from the starting materials. The surface elemental compositions of carbon support were determined using high-resolution scans shown in Figure 7-1.

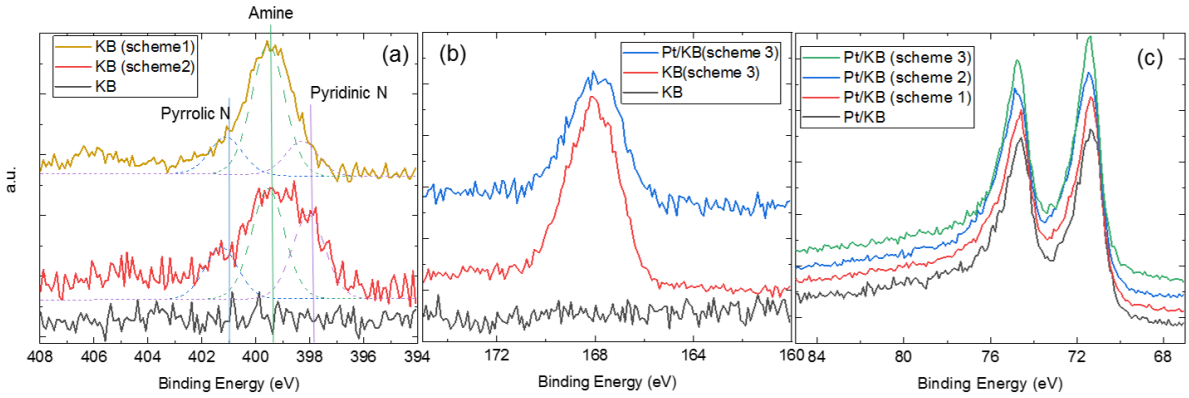

Figure 7-1 (a) Nitrogen 1s XPS spectra of KBs and peak deconvolution functionalized KBs into pyrrolic, amine, and pyridinic N, (b) Sulfur 2p spectra of KBs and KB after Pt deposition, and c) Platinum 4f spectra of KBs after Pt deposition.

In Table 1, KB exhibited a higher degree of functionalization evidenced by the higher atomic% N after schemes 1 and 2 and the higher atomic% S after scheme 3 than V and X carbon supports for the same amount of reaction time, because the pristine KB contained more amorphous carbon and higher oxygen content that are more prone to surface reactions than V and X carbon support.[1, 2] The carbon support X was highly crystalline as observed from TEM images, and a lower surface nitrogen content (0.6 atomic%) was obtained when

the support was reacted for the same duration as the Vulcan and KB. The durations of the surface functionalization schemes 1 and 2 were extended for carbon support X to achieve a similar degree of surface functionalization as those of Vulcan and KB. In addition to the extended reaction time, a more concentrated 50% nitric acid was used to pre-oxidize the X instead of the 30% nitric acid for Vulcan and KB.

Table 7-1 XPS results of pristine and functionalized carbon support for C 1s, O 1s, N 1s, and S 2p spectra. X (scheme 1) 24 h denotes 24 h of reaction instead of overnight reaction for other scheme 1 samples. X (scheme 2) 6 h, 50% denotes 6 h of pre-oxidation reaction in 50% HNO_3 whereas other scheme 2 samples were reacted in 30% HNO_3. Scheme-3 functionalization was not conducted for support X due to low performance of the scheme 3 observed in both KB and V. The adverse effect of the scheme 3 is discussed in detail in fuel cell performance.

Description	**Atomic% C**	**Atomic% O**	**Atomic% N**	**Atomic% S**
KB	98.8	1.2	0	0
KB (scheme 1)	93.5	2.8	3.7	0
KB (scheme 2)	95.0	2.2	2.8	0
KB (scheme 3)	89.1	9.7	0	2.2
V	99.4	0.6	0	0
V (scheme 1)	95.8	2.1	2.1	0
V (scheme 2)	97.1	1.5	1.4	0
V (scheme 3)	89.8	8.8	0	1.5
X	99.7	0.3	0	0
X (scheme 1) 24 h	95.5	2.3	2.1	0
X (scheme 2)	98.7	0.7	0.6	0
X (scheme 2) 6 h, 50%	95.7	2.5	1.7	0

The pristine KB exhibited a high BET surface area of 1009 m^2/g and the surface area decreased by 25-30% after scheme 1, scheme 2, and scheme 3 functionalization shown in Table 7-3Figure 7-3a. An insignificant amount of microporosity was observed in the pristine and the functionalized samples; hence the decrease in the surface area was attributed to the closure of some mesopores after the functionalization schemes. In comparison, Jung et al. found a threefold decrease in BET surface area after doping 1 atomic% N on the surface of KB using ethylenediamine.[3] Dowlapalli et al. observed a

similar decrease after diazonium reaction with sulfanilic acid.[2] Orfanidi et al. reported a 24% decrease in BET surface area after grating 0.9% N on Vulcan carbon support.[4] The BJH adsorptive/desorptive volumes exhibited a similar trend as the BET surface area and decreased between 20% and 25%. For Vulcan carbon, the pristine sample had a BET surface area of 230 m^2/g, which decreased by 42% after scheme 1. Although the decreases in mesopore volume and surface area may raise a concern for facilitating gas diffusion in the electrode, the locations of Pt particles and ionomer also play important roles in the diffusion process. Moreover, it was reported that the ECSAs of electrocatalysts did not correlate to the BET surface area of carbon support.[3-5] On the other hand, the surface areas of the carbon support X increased slightly after both scheme 1 and scheme 2 functionalization. This growth is attributed to increased defect sites and pore openings from the highly crystalline and graphitic pristine X, as demonstrated by the distinctive long, thick graphitic layers in TEM images and the sharp peak near 25° in XRD in Figure 7-2. The thick graphitic layers and the sharp XRD peak were absent in Vulcan or Ketjen black samples.

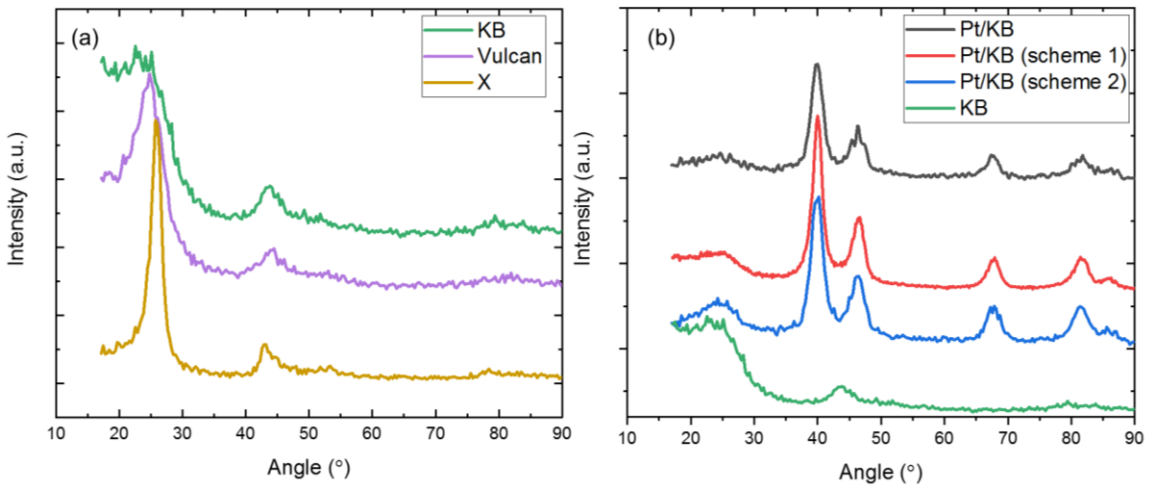

Figure 7-2 (a) XRD patterns of Ketjen black, Vulcan, and carbon support X. b) XRD of Ketjen black and platinized Ketjen blacks. Diffraction peaks between 24° and 26° indicate the graphitic structure of carbon supports. The scheme 2 functionalization appeared to

increase the graphitic feature of the Ketjen black, whereas scheme 1 did not affect it.

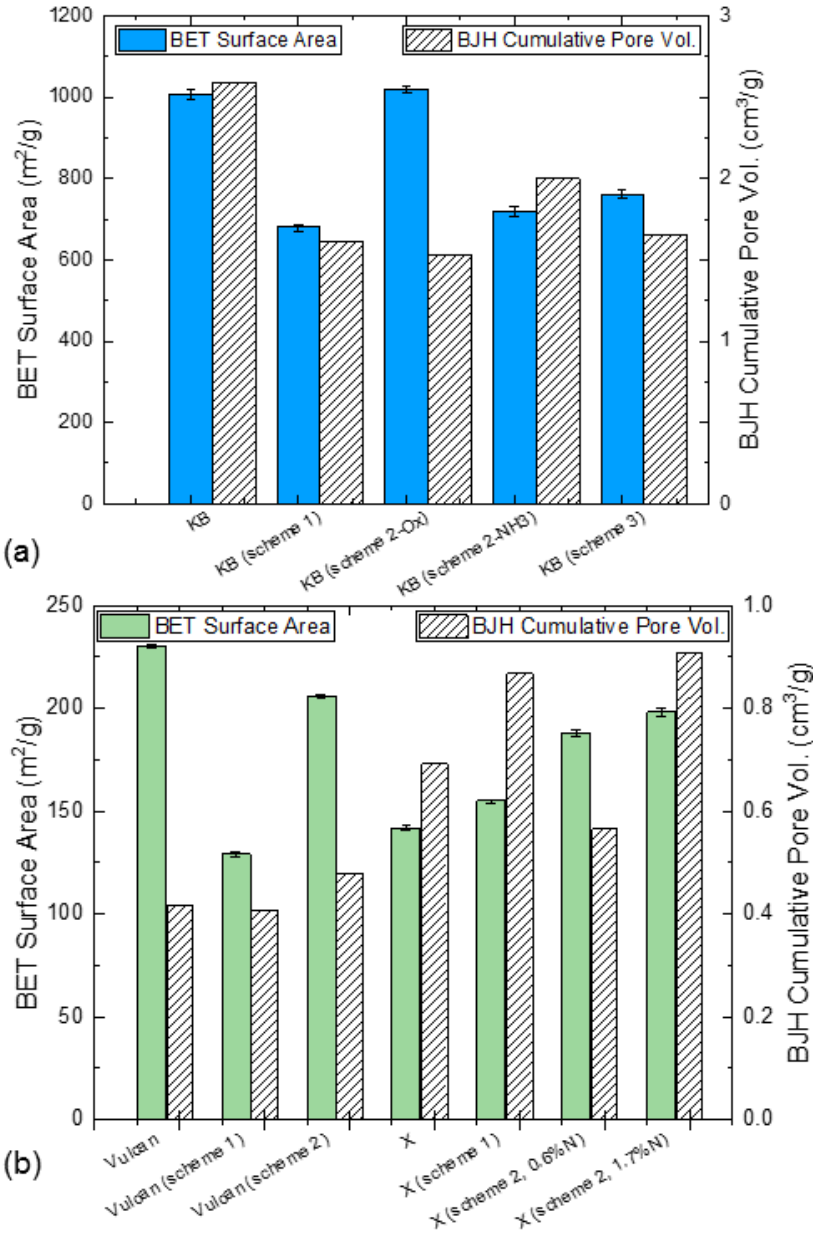

Figure 7-3 BET surface areas and BJH cumulative pore volumes of (a) KB and (b) Vulcan and carbon support X. The latter two were not in the same figure as KB because KB samples have four to five times higher surface areas or pore volumes than Vulcan and X.

In preparing the samples for contact angle measurements, the dried carbon solution did not form a uniform layer on glass slides. With the non-uniformity and large PTFE content (50 wt% in the solid), the contact angle measurements were not used to estimate the change in the hydrophilicity of the functionalized carbon support. Furthermore, the carbon powder

was compressed into a 10-mm-in-diameter using stainless steel die with 10 mm in diameter. A flat, smooth surface was achieved for the carbon pellet. Nevertheless, when a water droplet was placed on the surface of the carbon pellet, the pellet immediately absorbed the water and expanded. Although the prepared carbon solution that contains PTFE may help maintain the structure of the pellet when water droplet was placed, the stainless steel die require solid sample for compressing. Hence, the results of water contact angle measurements were not tabulated in this study.

Instead, the relative changes in surface hydrophilicity between the pristine and functionalized samples were compared using zeta potentials. The zeta potentials are plotted in the Figure 7-4and they represent the surface charge of carbon support in a solution, which was polar, aqueous in this study. An increase in surface charge leads to a decrease in water contact angle and an increase in surface hydrophilicity. For Vulcan carbon support, the zeta potential increased from -12.3 $\pm$ 3.7 mV to +20.1 $\pm$ 2.6 mV after scheme 1 and +18.7 $\pm$ 1.6 mV after scheme 2 functionalization. The increased zeta potentials indicated an increase in hydrophilicity of the carbon support with amine functional groups after the two functionalization schemes. On the other, the zeta potential of scheme 3 Vulcan sample decreased to -31.5 $\pm$ 7.7 mV, indicating that the sulfonate groups increased surface hydrophobicity.

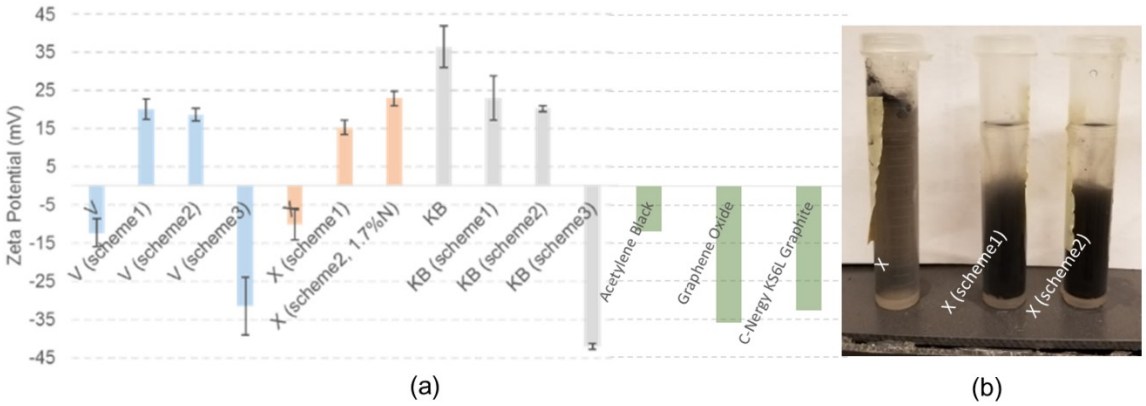

Figure 7-4 (a) Zeta potentials of pristine and functionalized carbon support in water and (b) pristine X after sonication for 1 minute and functionalized X after sonication for only 3 seconds.

Similar trends occurred in KB and carbon support X samples except that the pristine KB exhibited a positive zeta potential because the KB has a large BET surface area of 1,007 m^2/g and surface hydroxyl groups.[6, 7] Despite that, all three types of carbon support reached zeta potentials of +20 $\pm$ 5 mV after scheme 1 and 2 functionalization. In summary, the carbon support characterizations verified the occurrence of surface functionalization for all three schemes, showed the changes in BET surface area and pore volumes, and illustrated the changes of the surface charges of the carbon supports.

Table 7-2 BET surface areas and BJH pore volumes of carbon and Pt-deposited carbon samples

Sample	BET Surface Area (m^2/g)	BJH Pore Volume (cm^3/g)
KB	1007 $\pm$ 14	2.590
Pt/KB	1013 $\pm$ 13	1.893
KB (scheme1)	680 $\pm$ 8	1.616
Pt/KB (scheme1)	971 $\pm$ 8	1.946
KB (scheme2)	720 $\pm$ 12	2.002
Pt/KB (scheme2)	956 $\pm$ 7	1.634
KB (scheme3)	761 $\pm$ 11	1.652
Pt/KB (scheme3)	585 $\pm$ 10	1.518

7.2 Fuel Cell Performance

In Figure 7-5, Tafel plots show that both scheme 1 and scheme 2 improved the mass

activities of the electrocatalysts, while scheme 3 had the opposite effect on the electrocatalyst supported on both KB and Vulcan. The improved mass activities were likely due to the functionalization that increased electron donation from the functional sites of the carbon support to the Pt particles.[8, 9] The XPS plot shows that KB after scheme 1 was grafted with nearly all amine functional groups centered on binding energy of 399.3 eV, whereas the KB after scheme 2 contained 45% amine, 35% pyridinic N, and 20% pyrrolic N. Hence, the further improvement of the mass activities by scheme 2 relative to that of scheme 1 implied the benefit of pyrrolic/pyridinic nitrogen in scheme 2 despite its lower surface nitrogen content than that of scheme 1. The benefit of pyridinic nitrogen in carbon support has been discussed by other researchers.[4, 10] The improvement in the mass activities may also result from the formation of atomic C-N as the active sites for ORR in the absence of Pt particles.[11]

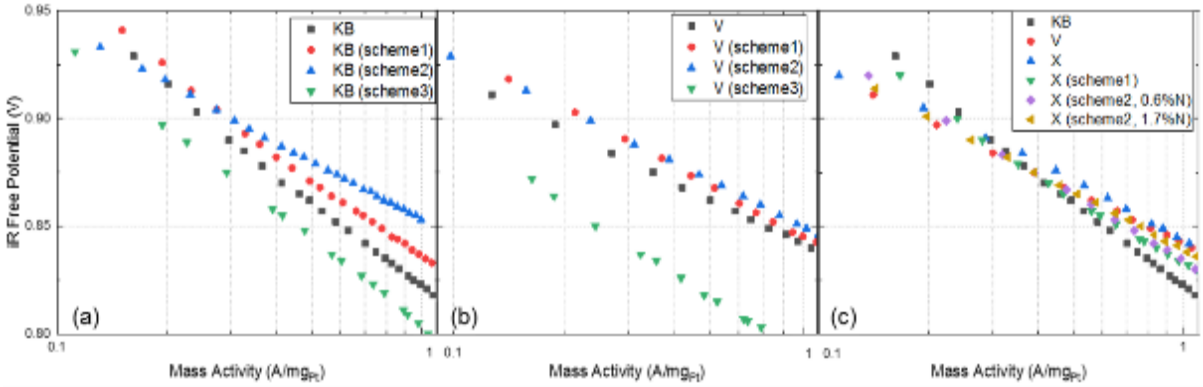

Figure 7-5 Tafel plots of (a) KB samples, (b) Vulcan samples, and (c) X sample in comparison with pristine KB and V samples under 2 l min−1 H2 | 5 l min−1 O2, 80 °C, 100% RH, and 150 kPa$_{abs}$.

In theory, the sulfonate functional groups on the carbon support provides additional proton conduction in the catalyst layer and may enhance the overall performance.[12, 13] However, despite the same Pt particle size as the pristine KB sample (3.4 ± 0.7 nm shown in Table 7-3), the lower performance of scheme 3-functionalized samples indicated the

poison effect to Pt electrocatalyst by sulfonate surface group causing sluggish kinetics, which has been discussed by other researchers.[8, 14, 15] As a result of the poison effect by the sulfonate surface group, scheme 3 functionalization was not performed on the carbon support X. In addition to the poison effect of sulfonate groups on carbon support, scheme 3 also caused severe agglomeration of Pt particles on carbon support as shown in the TEM images in Table 7-3, in which Pt particle sizes were obtained from STEM or TEM images and particle size distributions. The particle size distributions were taken from at least 50 particles and multiple electron images may be needed to produce the histograms shown in the Table 7-3.

Table 7-3 Pt particle sizes obtained from STEM or TEM images and particle size distributions. The particle size distributions were taken from at least 50 particles and multiple electron images may be needed to produce the histograms shown in the Table. t

Catalyst Info. and Particle Size	Image	Catalyst Info. and Particle Size	Image
Pt/KB 3.4 $\pm$ 0.7	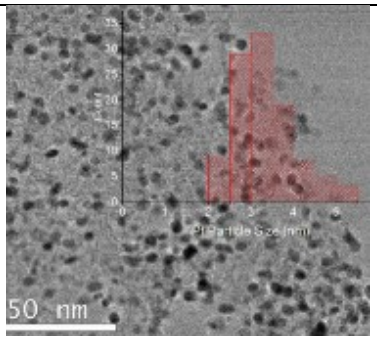	Pt/KB (scheme 3) 3.4 $\pm$ 0.6	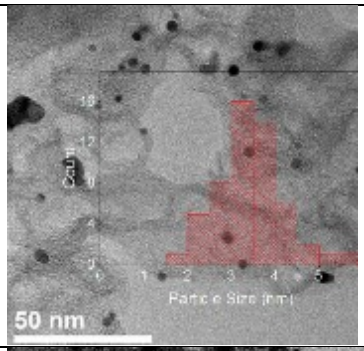
Pt/KB (scheme 1) 3.3 $\pm$ 0.7	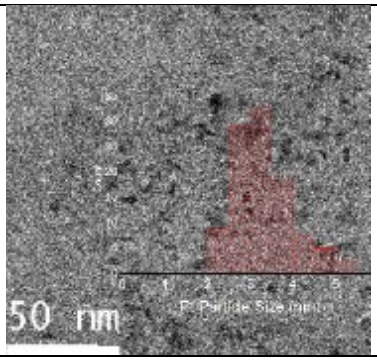	Pt/V 3.6 $\pm$ 1.0	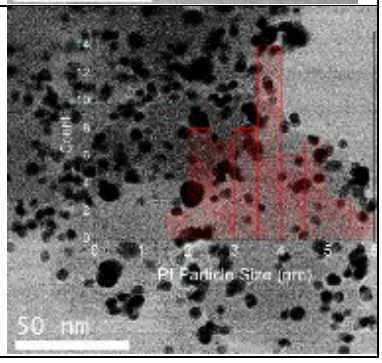

Pt/KB (scheme 2) 2.8 ± 0.9	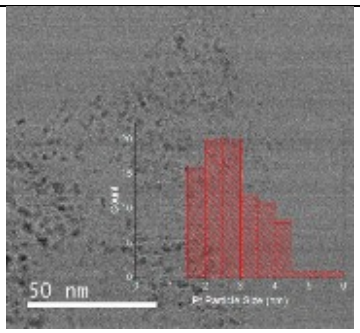	Pt/V (scheme 1) 3.6 ± 0.4	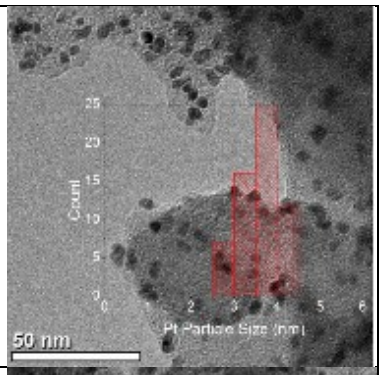
Pt/V (scheme 2) (1.4%N) 3.5 ± 0.5	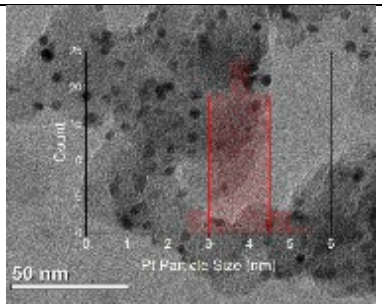	Pt/X (scheme 1) 3.1 ± 0.6	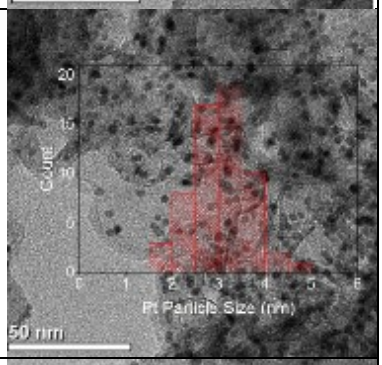
Pt/V (scheme 2) (3.4%N) 3.1 ± 0.5	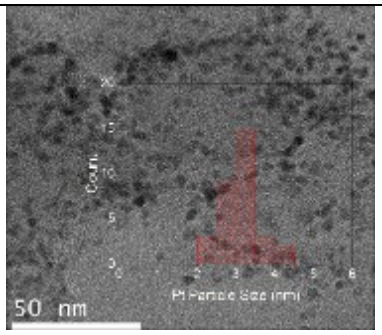	Pt/X (scheme 1) 5,000 cycles of 1.0 V – 1.5 V 4.1 ± 1.1	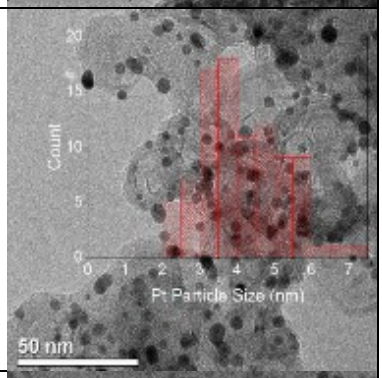
Pt/V (scheme 2) (4.6%N) 3.7 ± 0.9	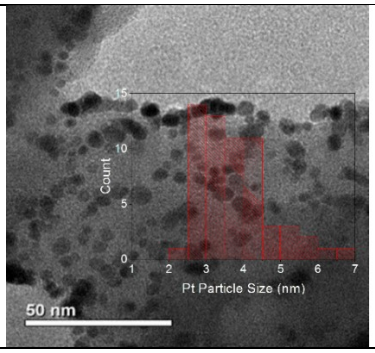	Pt/X (scheme 2， 0.6%N) 3.1 ± 0.6	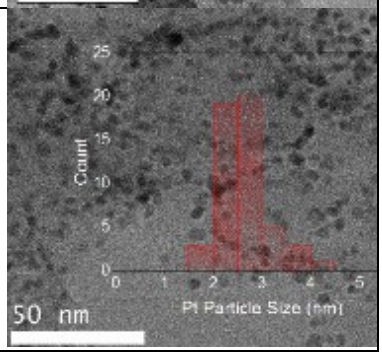

Pt/V (scheme 3) 3.3 ± 0.5	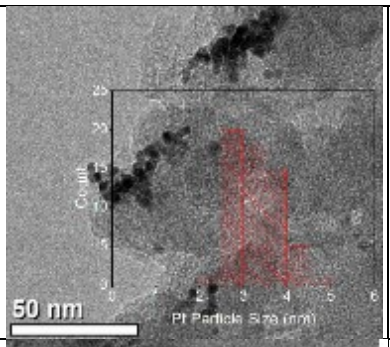	Pt/X (scheme 2， 1.7%N) 3.1 ± 0.7	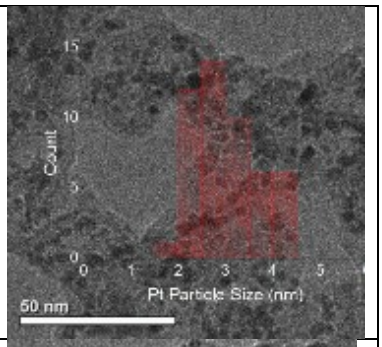
Pt/X 3.0 ± 0.7	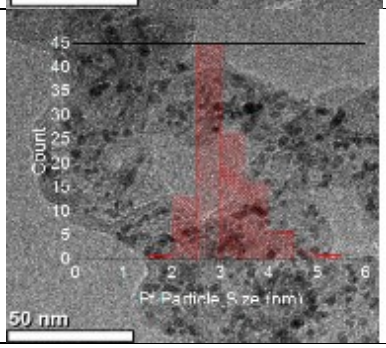	Pt/X (scheme 2， 1.7%N) 5,000 cycles of 1.0 V – 1.5 V 3.1 ± 0.7	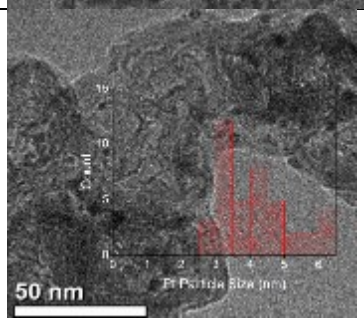

The type of carbon support appeared to affect the level of mass activity improvement. That is, the more graphitic carbon support with smaller BET surface area showed a lesser degree of mass activity improvement, corresponding to the difference in carbon reactivity of the surface functionalization found in XPS results. For example, both Vulcan and X were grafted with 2.1 atomic% N after scheme 1 functionalization; however, the mass activity was increased by 15% in Vulcan and 4% in carbon support X.

Furthermore, Pt particle size and distribution also impacted the kinetics, though their impacts appeared to be less significant than the functionalization and the type of carbon support. For example, in compared to 3.4 nm ± 0.7 nm of Pt/KB catalyst, Pt/KB (scheme 2) had a Pt size 2.8 nm ± 0.9 nm and a 10% increase in mass activity. On the other hand, Pt/V had a larger particle size and a wider size distribution (3.6 nm ± 1.0 nm) than those of Pt/V (scheme 3) sample (3.3 nm ± 0.5 nm), but the latter had a significantly worse mass activity and overall performance than the former shown in Figure 7-5and Figure 7-6. Figure 7-6 shows that the type of carbon support played a substantial role in the cell performance

in medium to high current densities. Despite the similar mass activities of the three types of carbon support shown in Figure 7-5c., the cathode using Vulcan support exhibited the highest performance in the medium to high current densities. The improved performance was attributed to the higher portion of Pt particles located on outer surface of the Vulcan support than that of the KB, allowing the reaction sites more accessible, as reported by other researchers.[5] The improved performance could also be due to a difference in ionomer distributions. Among KB samples, both scheme 1 and scheme 2 improved the cell performance, while scheme 3 worsened the performance, correlating to the trend in mass activities observed in the Tafel plot of Figure 7-5a.

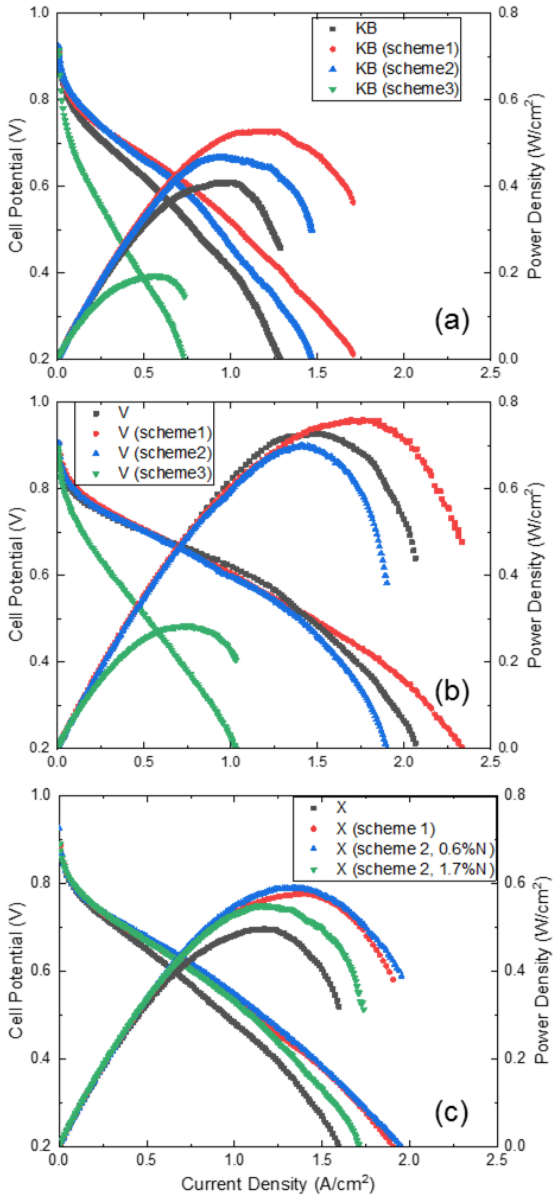

Figure 7-6 Polarization curves of BOL samples with cathodes made of (a) KB, (b) Vulcan, and (c) carbon support X at 80°C, 100% RH, 150 kPa_{abs}, 2 L/min H_2 | 5 L/min Air.

Similar to the trend of the KB samples, Vulcan after scheme 1 exhibited the highest performance at medium to high current densities. In contrast to the results from previous reports,[4] the ammonia-treated Vulcan (scheme 2) was not found to improve cell performance at medium to high current densities. Two additional MEAs of Pt/V (scheme 2) and one additional batch of Pt/V (scheme 2) as well as its corresponding MEA were made and tested. The same trend was observed at medium to high current densities, and

the lack of improvement on mass transfer may be attributed to the partial closure of mesopores of the carbon support after the scheme 2 functionalization that is shown in BET and BJH results.

The cell performance of pristine and functionalized carbon support X samples exceeded those of the KB samples but trailed behind those of the Vulcan samples. For the carbon support X, scheme 1 and scheme 2 both enhanced the max power density by 14% while the mass activity of the functionalized X only increased by 4%. Therefore, the greater improvement of the power density was attributed to the functionalization. The effect of degree of functionalization was studied on X (scheme 2) with one 0.6% N sample and one 1.7% N sample and it was found that prolonged oxidation and amination did not improve the mass activities or performance at high current densities.

Although the polarization curves illustrated the improvements by scheme 1 and scheme 2 functionalization at medium to high current densities, the improvement of mass transport needed to be further examined by individual voltage losses. A theoretical transport polarization (Nernstian loss), $V_{\text{Transport Theo}}$, was calculated by

$$V_{\text{Transport Theo}} = \frac{RT}{F}\left(\frac{1}{4}+\frac{\gamma_{O_2}}{\alpha}\right)\ln\left(1-\frac{i}{i_{\text{lim}}}\right), \tag{7.1}$$

where γ_{O_2} is the kinetic reaction order with respect to partial pressure of O_2, α is the transfer coefficient ($\alpha = 1$), and i and i_{lim} are geometric and limiting current densities.[16] The theoretical transport polarization was expected to underestimate the experimental polarization due to the additional transport resistance local to Pt catalysts that have been discussed in various reports.[17-19] The experimental transport polarization was determined by

$$V_{\text{Transport}} = V_{\text{cell}} - \left[\underbrace{U^{\theta}}_{\text{Equilibrium V}} - \underbrace{b \log\left(\frac{i + i_x}{i_o}\right)}_{\text{Kinetic}} - \underbrace{i R_{\Omega}}_{\text{Ohmic}} - \underbrace{i R_{\text{H}^+,\text{CL}}}_{\text{Proton in Electrode}} \right], \quad (7.2)$$

where the equilibrium voltage, U^{θ}, is 1.18 V at 80 °C, b is the Tafel slope, and i_o is the exchange current density of the Pt. Both b and i_o are determined from polarization curves under $H_2|O_2$. i_x is the cross-over current density, R_{Ω} is the membrane resistance determined from the built-in iR interrupt technique of the fuel cell test station, and $R_{\text{H}^+,\text{CL}}$ is the proton resistance in the catalyst layer determined from EIS under $H_2|N_2$. The kinetic polarizations correlate well to the trends shown in Tafel plots of Figure 7-5, and membrane resistances were very similar among the samples around 0.07 Ω-cm^2. The proton resistances of catalyst layers varied more than the membrane resistances, ranging from 0.2 Ω-cm^2 to 0.6 Ω-cm^2 as shown in Table 7-4. The proton resistances were higher for KB samples than Vulcan and X samples due to the greater amount of pores in the primary KB carbon particles on which the deposited ionomer did not contribute to the proton conduction path in the catalyst layer.[20]

Table 7-4 Experimentally determined MEA parameters. Tafel slope is obtained from polarization curve under 2 L/min H_2 |5 L/min O_2, 80 °C, 150 kPa_{abs}, corrected for iR and H_2 cross-over. Proton resistance in CL is determined from EIS under 0.4L/min H_2 |0.4 L/min N_2, 80 °C, ambient pressure. Membrane resistance is obtained from EIS under 2 L/min H_2 |5 L/min Air, 80 °C, 150 kPa_{abs}. ECSA is calculated from cyclic voltammogram between 0.05V and 0.4 V under 0.05 L/min H_2 |0.4 L/min N_2. Carbon loss is measured from cathode CO_2 exhaust by a non-dispersive infrared (NDIR) instrument during potential cycling at 0.25 L/min H_2 |0.25 L/min N_2. Non-pressure dependent mass-transfer resistance, R_{NP}, is determined from 1 L/min H_2 |5 L/min 4% O_2 in N_2 using 4 different pressures.

Cell Information	Tafel Slope (mV/dec)	Proton Resistance in CL (ohm-cm^2)	Membrane Resistance (ohm-cm^2)	ECSA (m^2/g$_{Pt}$)	C Loss 500 cycles (µg/cm^2)	C Loss 5,000 cycles (µg/cm^2)	R_{NP} (s/cm)
KB	130	0.55	0.052	50	15.6	NA	1.61
KB (scheme 1)	120	0.32	0.060	45	21.4	NA	1.12
KB (scheme 2)	94	0.52	0.055	44	34.6	NA	1.55
KB (scheme 3)	134	0.39	0.061	26	22.8	NA	2.12
V	82	0.22	0.052	55	7.3	41.7	0.50
V (scheme 1)	83	0.36	0.062	51	15.6	79.0	0.48
V (scheme 2)	88	0.24	0.057	54	9.4	52.2	0.61
V (scheme 3)	110	0.19	0.067	39	10.8	60.1	1.67

X	95	0.22	0.064	66	1.8	39.5	1.24
X (scheme 1)	95	0.32	0.060	67	2.8	43.4	0.61
X (scheme 2, 0.6%N)	94	0.29	0.055	57	3.5	43.7	0.73
X (scheme 2, 1.7%N)	86	0.33	0.058	54	4.4	44.7	1.08

Figure 7-7 shows the higher mass-transfer voltage losses in KB samples than Vulcan and carbon support X samples. One reason was that Pt particles tended to deposit in large and deep pores of KB, whereas the Pt particles were more prevalent on the surfaces of Vulcan and carbon support X, which has been reported by other researchers and observed in the STEM and TEM images in the supporting information. Among the KB samples, the trend of the mass-transfer voltage losses followed:

KB(scheme 3) > pristine KB > KB(scheme 2) > KB (scheme 1),

which is the opposite of the cell performance at medium to high current densities shown in Figure 7-6a. At these current densities, the increased performance resulted from the lower mass-transfer voltage losses.

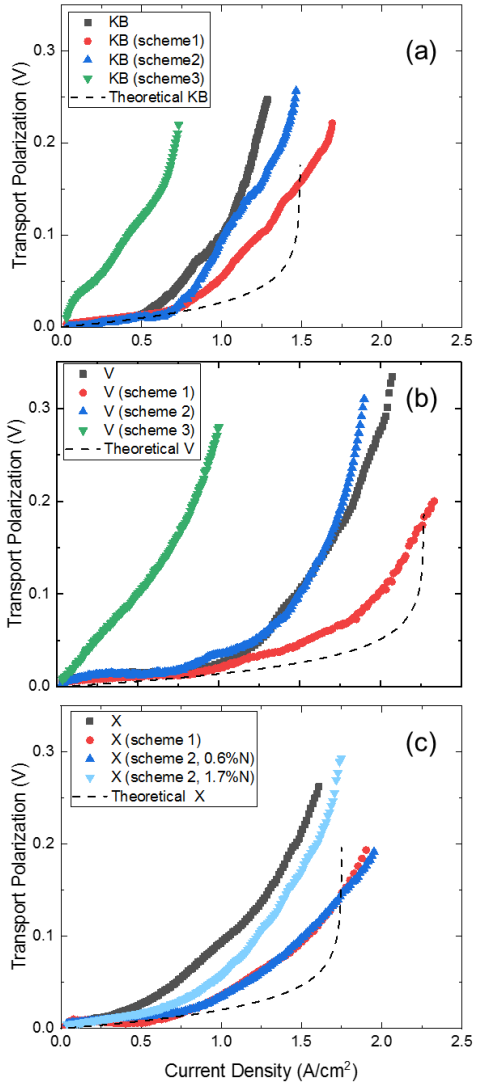

Figure 7-7 Experimental and theoretical transport polarizations of (a) KB samples, (b) Vulcan samples, and (c) X samples.

Compared to the scheme-3 functionalized samples with a large mass-transfer polarization of 0.1 V at a current density of 0.4 A/cm^2, the pristine KB sample reached the same amount of mass-transfer polarization near 1.0 A/cm^2. The larger mass-transfer polarization of the scheme-3 functionalized KB likely resulted from a decrease in pore area and volume after Pt deposition on the KB (scheme 3), whereas the Pt deposition on other KB samples did not significantly changed their BET surface areas shown in Table 7-2.The reduction in pore area and volume rendered less accessible Pt active sites, which decreased the effective Pt loading in the cathode. Many researchers have reported the larger

local/interfacial transport resistance when cathode Pt loading is decreased.[17, 19] Furthermore, scheme 3 functionalization affected distribution of Pt particles, because TEM images in the Supporting Information show significant Pt agglomeration. The local mass-transport resistance was determined to increase from 1.61 s/cm in Pt/pristine KB to 2.12 s/cm in Pt/KB (scheme 3) using Baker's limiting current technique in Table 7-4.Hence, it was evident that the scheme 3 (sulfonate groups) adversely affected the local mass transport.

The larger mass-transfer polarization of the scheme-3 functionalized KB possibly resulted from less accessible Pt active sites that decreased the effective Pt loading in the cathode. Many researchers have reported the larger local/interfacial transport resistance when Pt loading is decreased.[17, 19] Considering that the scheme 3 sample was only grafted with 2.2 atomic% sulfur content and its BET surface area only decreased by 24%, the smallest percent reduction of all schemes, it was evident that the poison effect of Pt adversely affected the local mass-transport resistance.

In Vulcan samples, the trend of the mass-transfer polarizations followed the opposite of the cell performance. It is worth noting that the plots of the pristine and the scheme-2 functionalized Vulcan samples overlapped over the majority of the current densities. Among carbon support X samples, the trend of mass-transfer polarization differed from those of the KB and Vulcan and followed the order of pristine X > scheme 1 > scheme 2. The reduction in mass-transfer polarization after scheme 2 was likely caused by a combination of an ionomer-carbon support interaction and an increase in BET surface area, the latter of which was absent in KB and Vulcan samples.

7.3 Ionomer Coverage

To analyze the impact of ionomer-carbon support interaction, a novel method using STEM/EDS images to estimate ionomer coverage was developed and its procedures are detailed in the Figure 7-8 captions. As an input parameter, 7 nm ionomer film thickness was chosen based on calculations by Lopez-Haro et al.[21] According to Kusoglu et al., the thickness of the Nafion ionomer wall is approximately 3 nm to 4 nm, and hence 4 nm was chosen as the maximum distance between two nearest F pixels, which were marked as ionomer coverage in step (f) in Figure 7-8.[22] In other words, if a distance between two adjacent F pixels exceeded 4 nm, it was unlikely that the portion of the carbon edge between the two points was covered by the ionomer. More details on the selection of F pixels for ionomer coverage are described in the Supporting Information.

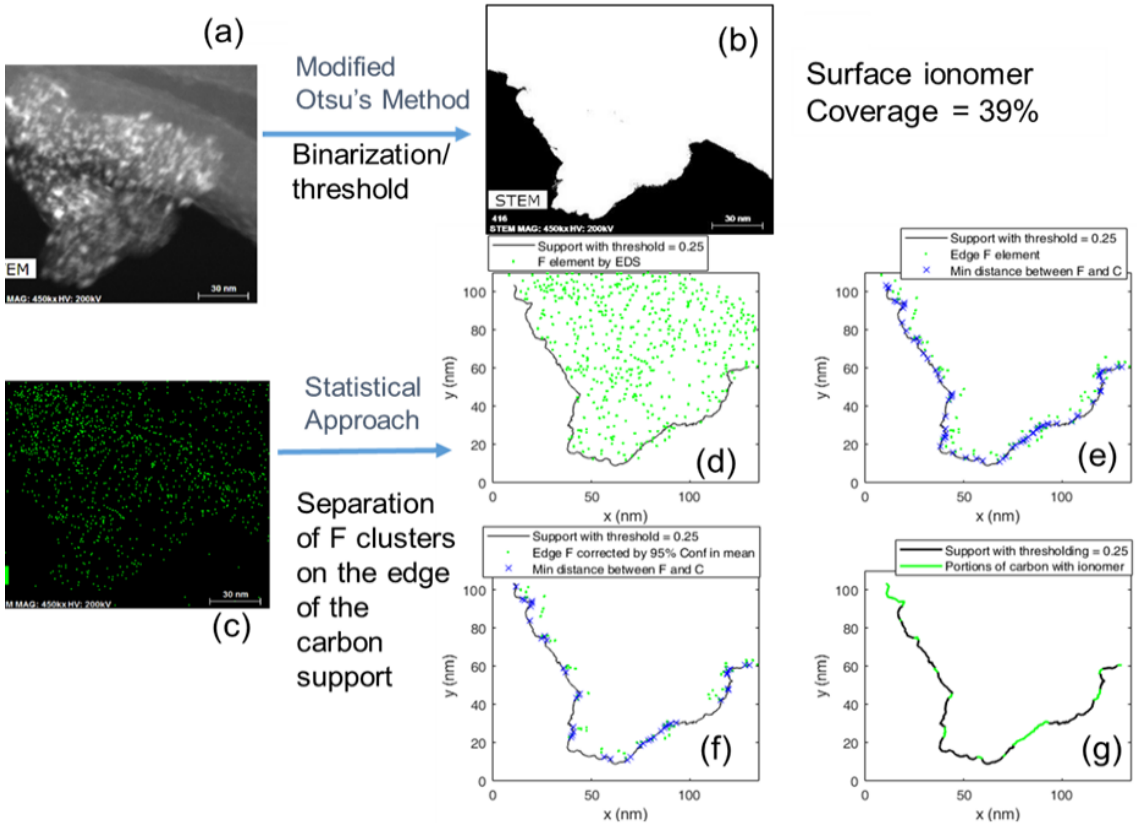

Figure 7-8 Procedures to calculate percent surface ionomer coverage on carbon support using STEM/EDS: a) collect a STEM image with clear edges of an agglomerate, b) separate

the edges using a proper threshold (0.26 for this sample), c) map the F element, d) reconstruct the F on the separated edges of the agglomerate, e) filter the F pixels within 7 nm of the edges, f) omit the F pixels with adjacent distance greater than the upper mean distance of 95% confidence level of Poisson distribution and label the points (x) on the edge of the carbon support with the shortest distance between the F pixels and the carbon edge, and g) highlight the carbon support edges that are mostly likely covered by the remaining F pixel clusters. The calculated ionomer coverage is 39% for an I/C (KB after scheme 1) weight ratio of 0.65.

In Table 7-5, the averaged surface ionomer coverage increased from 26% to 30% after scheme 1 and to 33% after scheme 2 functionalization for KB samples, though large uncertainties were observed. In addition, the functionalization appeared to lead to a more uniform ionomer distribution as is evident from the smaller standard deviation of Pt/X (scheme 2, 0.6% N) than that of Pt/X. The large uncertainties in ionomer coverage resulted from a tradeoff between a large field of view for mitigating radiation damage and a small field of view for obtaining detailed elemental mapping.

The ionomer coverage results in this study were lower than some published values due to differences in measurement/calculation techniques. Ikeda et al. used a cyclic voltammetry approach and Lopez-Haro et al. applied STEM imaging of Cs-stained ionomer on carbon support. The former found that ionomer coverage only increased by 10% for a twofold increase in I/C ratio, whereas the latter determined that the ionomer film thickness did not vary but coverage nearly doubled for a twofold increase in I/C ratio. In this study, the ionomer coverage increased almost linearly with I/C ratio but the absolute value of the ionomer coverage only increased by 50% when the I/C ratio was nearly tripled. One cause may be the inclusion of ionomer in the binarization step of carbon support. The inclusion of ionomer led to overestimation of the carbon support circumference and thus a lower coverage value. Another cause for the lower ionomer coverage in this study was likely the removal of a portion of F pixels above the upper limit of the 95% confidence

level of Poisson's distribution from step (e) to step (f) in Figure 7-8. Since the increase in ionomer coverage was less significant than the improvement in cell performance, the difference suggested the importance of not only how much the ionomer covered the carbon support but also how the ionomer was distributed on the carbon support. The former was examined through the STEM/EDS approach while the latter was more challenging to image.

Another important experimental condition to consider is hydration of the ionomer. Under the vacuum environment of STEM/EDS measurement, the ionomer is dry, whereas the fuel cells were operated at 100 % RH. Therefore, the volume expansion of the ionomer due to hydration should be accounted for in the ionomer coverage values used in the modified agglomerate model. Weber group found expansion of Nafion 212 in through- and in-plane directions at different temperatures.[23] Extracting the data from the plot, the one-dimensional expansions as a function of temperature are

$$\%expasion_{through-plane} = 0.1244\ (T - 273.15) + 6.680 \tag{7.3}$$

$$\%expasion_{in-plane} = 0.1042\ (T - 273.15) + 4.258 \tag{7.4}$$

Therefore, the experimental surface ionomer coverage was corrected for its 2-D expansion in the through-plane direction listed in Table 7-5. The new coverage values approached 50%, or half of the carbon support being covered by the ionomer. The impact of the surface functionalization remained the same.

Table 7-5 Published ionomer coverage results and experimental results using STEM images with fluorine EDS maps.

Sample description	Surface coverage averaged and individual values (%)	Average layer thickness (nm)	Surface coverage after correction (%)
Published Result for KB, I/C = 0.75[24]	55	N/A	
Published Result for KB, I/C = 0.50[24]	52	N/A	
Published Result for Vulcan, I/C = 0.5[21]	79.5 ± 2.3	7.2 ± 2.1 (output)	
Pt/KB, I/C = 0.38	20 ± 6 (20, 13, 19, 28)	7 (input)	27± 8
Pt/KB, I/C = 0.66	26 ± 6 (26, 28, 18, 32)	7 (input)	35± 8
Pt/KB, I/C = 1.06	31 ± 3 (29, 33, 34, 27)	7 (input)	42± 4
Pt/KB (scheme1), I/C = 0.66	30 ± 8 (22, 39, 30)	7 (input)	41± 11
Pt/KB (scheme2), I/C = 0.66	33 ± 7 (34, 25, 42)	7 (input)	45± 9
Pt/X, I/C = 0.66	26 ± 11 (38, 17, 22)	7 (input)	35± 15
Pt/X (scheme 2, 0.6% N), I/C = 0.66	33 ± 7 (29, 40, 30)	7 (input)	45± 9

7.4 References

1. F. Xu, M.-x. Wang, Q. Liu, H.-f. Sun, S. Simonson, N. Ogbeifun, E. A. Stach, and J. Xie, *Journal of the Electrochemical Society,* **157** (8), B1138-B1145 (2010).

2. M. R. Dowlapalli, P. Atanassov, J. Xie, and G. Rice, *ECS Transactions,* **1** (8), 41-50 (2006).

3. W. S. Jung and B. N. Popov, *Carbon,* **122** 746-755 (2017).

4. A. Orfanidi, P. Madkikar, H. El-Sayed, G. Harzer, T. Kratky, and H. Gasteiger, *Journal of The Electrochemical Society,* **164** (4), F418-F426 (2017).

5. G. S. Harzer, A. Orfanidi, H. El-Sayed, P. Madkikar, and H. A. Gasteiger, *Journal of The Electrochemical Society,* **165** (10), F770-F779 (2018).

6. Y. Sun, I. Sinev, W. Ju, A. Bergmann, S. r. Dresp, S. Kühl, C. Spöri, H. Schmies, H. Wang, and D. Bernsmeier, *ACS Catalysis,* **8** (4), 2844-2856 (2018).

7. A. Shukla, A. Hamnett, A. Roy, S. Barman, D. Sarma, V. Alderucci, L. Pino, and N. Giordano, *Journal of Electroanalytical Chemistry,* **352** (1-2), 337-343 (1993).

8. S. Roy, A. Harding, A. Russell, and K. Thomas, *Journal of the Electrochemical Society,* **144** (7), 2323-2328 (1997).

9. L. Xin, F. Yang, S. Rasouli, Y. Qiu, Z.-F. Li, A. Uzunoglu, C.-J. Sun, Y. Liu, P. Ferreira, and W. Li, *ACS Catalysis,* **6** (4), 2642-2653 (2016).

10. S. Ott, A. Orfanidi, H. Schmies, B. Anke, H. N. Nong, J. Hübner, U. Gernert, M. Gliech, M. Lerch, and P. Strasser, *Nature Materials,* **19** (1), 77-85 (2020).

11. E. F. Holby and P. Zelenay, *Nano Energy,* **29** 54-64 (2016).

12. Y. Liu, M. W. Murphy, D. R. Baker, W. Gu, C. Ji, J. Jorne, and H. A. Gasteiger, *Journal of The Electrochemical Society,* **156** (8), B970-B980 (2009).

13. L. Xin, F. Yang, J. Xie, Z. Yang, N. N. Kariuki, D. J. Myers, J.-K. Peng, X. Wang, R. K. Ahluwalia, and K. Yu, *Journal of The Electrochemical Society,* **164** (6), F674-F684 (2017).

14. S. S. Kocha, J. W. Zack, S. M. Alia, K. Neyerlin, and B. S. Pivovar, *ECS Transactions,* **50** (2), 1475-1485 (2013).

15. R. Subbaraman, D. Strmcnik, A. P. Paulikas, V. R. Stamenkovic, and N. M. Markovic, *ChemPhysChem,* **11** (13), 2825-2833 (2010).

16. P. Zihrul, I. Hartung, S. Kirsch, G. Huebner, F. Hasché, and H. A. Gasteiger, *Journal of The Electrochemical Society,* **163** (6), F492-F498 (2016).

17. A. Z. Weber and A. Kusoglu, *Journal of Materials Chemistry A,* **2** (41), 17207-17211 (2014).

18. A. Kongkanand and M. F. Mathias, *The journal of physical chemistry letters,* **7** (7), 1127-1137 (2016).

19. T. A. Greszler, D. Caulk, and P. Sinha, *Journal of The Electrochemical Society,* **159** (12), F831-F840 (2012).

20. Y. Liu, C. Ji, W. Gu, J. Jorne, and H. A. Gasteiger, *Journal of The Electrochemical Society,* **158** (6), B614-B621 (2011).

21. M. Lopez-Haro, L. Guétaz, T. Printemps, A. Morin, S. Escribano, P.-H. Jouneau, P. Bayle-Guillemaud, F. Chandezon, and G. Gebel, *Nature communications,* **5** (2014).

22. A. Kusoglu and A. Z. Weber, *Chemical reviews,* **117** (3), 987-1104 (2017).

23. S. Shi, A. Z. Weber, and A. Kusoglu, *Journal of Membrane Science,* **516** 123-134 (2016).

24. K. Ikeda, N. Nonoyama, and Y. Ikogi, *ECS Transactions,* **33** (1), 1189-1197 (2010).

CHAPTER 8. MODEL DEVELOPMENT FOR IONOMER COVERAGE

8.1 Literature Review on Modeling Ionomer Coverage in Electrode

A number of modeling (the agglomerate model and kinetic-gas model) and experimental techniques (oxygen or hydrogen limiting current measurements) have been developed to investigate the local transport resistance of cathode.[1-6] Many of the publications have found that ionomer thin films in the CCL are more resistive to the oxygen diffusion to Pt sites than bulk ionomer films and that the oxygen permeation through the ionomer is the dominant resistance especially at low Pt loadings.[1, 3, 7]

The first implementation of agglomerate model in PEM fuel cells was published by Ridge et al. in 1989.[8] They used cylindrical agglomerates through which oxygen diffuses while simultaneously reacting. Their model only focused on cathode and GDL and neglected the anode and the membrane. The first full PEM fuel cell was developed by Springer et al. at Los Alamos National Laboratory in 1991.[9] The Fuller research group had previously employed a flooded agglomerate with thin film model describing oxygen transport through the ionomer in the cathode catalyst layer shown in Figure 8-1a. An approximate analytical solution is obtained with a pseudo-steady-state approximation.[10]

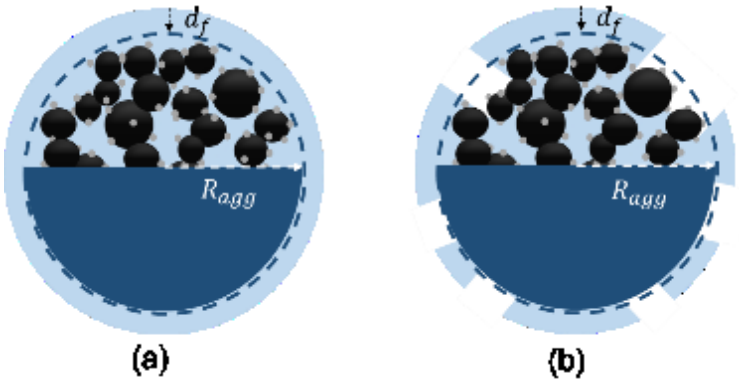

Figure 8-1 (a) Illustration of an agglomerate model for ionomer diffusion and (b) an agglomerate model with partial ionomer coverage.

In the agglomerate model developed by Setzler and Fuller, only one oxygen partial pressure was defined. The oxygen partial pressure in the ionomer film, $p_{O_2,f}$, is calculated as

$$p_{O_2,f} = p_{O_2} - \frac{H_{O_2,i}\, j_{ORR}\, R_{agg}}{3\, D_{O_2,i}\,(1 - \varepsilon_g)\left(\frac{1}{d_f} - \frac{1}{R_{agg}}\right)}. \quad (8.1)$$

The detail of each parameter and variable can be found in LIST OF SYMBOLS AND ABBREVIATIONS section. It is worth noting that j_{ORR} denotes the rate of the oxygen reduction reaction on a volumetric basis. The second term on the right-hand side of the equation describes the change in oxygen partial pressure due to ionomer film transport resistance, which should increase with either the ionomer film thickness, d_f, or the agglomerate radius, R_{agg}. The authors determined 840 nm and 27.1 nm for agglomerate diameter and ionomer film thickness, respectively, after fitting the model to experimental data. In comparison, other publications with agglomerate models have used agglomerate size ranging from 100 nm to 2000 nm listed in Table 8-1.[11-14]

Table 8-1 Literature values for agglomerate sizes used in PEM fuel cells.

Author (Year)	**Agglomerate Diameter (nm)**	**Ionomer Film Thickness (nm)**
Jaouen (2002)[11]	1,000	0 - 50
Guo (2004)[12]	2,000	3,550
Secanell (2007)[13]	500 – 2,000	0 - 80
Xing (2014)[15]	500 – 1,000	An equation based on mass conservation
Setzler (2015)[10]	420	27.1
Kulikovsky (2017)[14]	100	30
Mashio (2017)[16]	40	3
Darling (2018)[17]	150	3
Darling (2020)[18]	150 – 300	3

As part of the surface functionalization study in CHAPTER 7, SEM and STEM images of electrodes prepared at the Fuller laboratory were measured. They show a large variation

in size of the possible carbon/ionomer agglomerates between approximately 400 nm and 900 nm as illustrated in Figure 8-2 a and b; nevertheless, well-defined boundaries do not exist. Other researchers have suggested the use of well-defined carbon primary particle as an agglomerate in the model.[16] In addition, the experimental values found in the literature have reported thinner ionomer thickness than 27.1 nm used by Setzler and Fuller.[19, 20] The variations in agglomerate size and ionomer film thickness and their difference from the experimental values suggest that it is better to treat the agglomerate model as a purely empirical description of internal and external mass-transfer limitations rather than a literal model describing the catalyst layer microstructure.

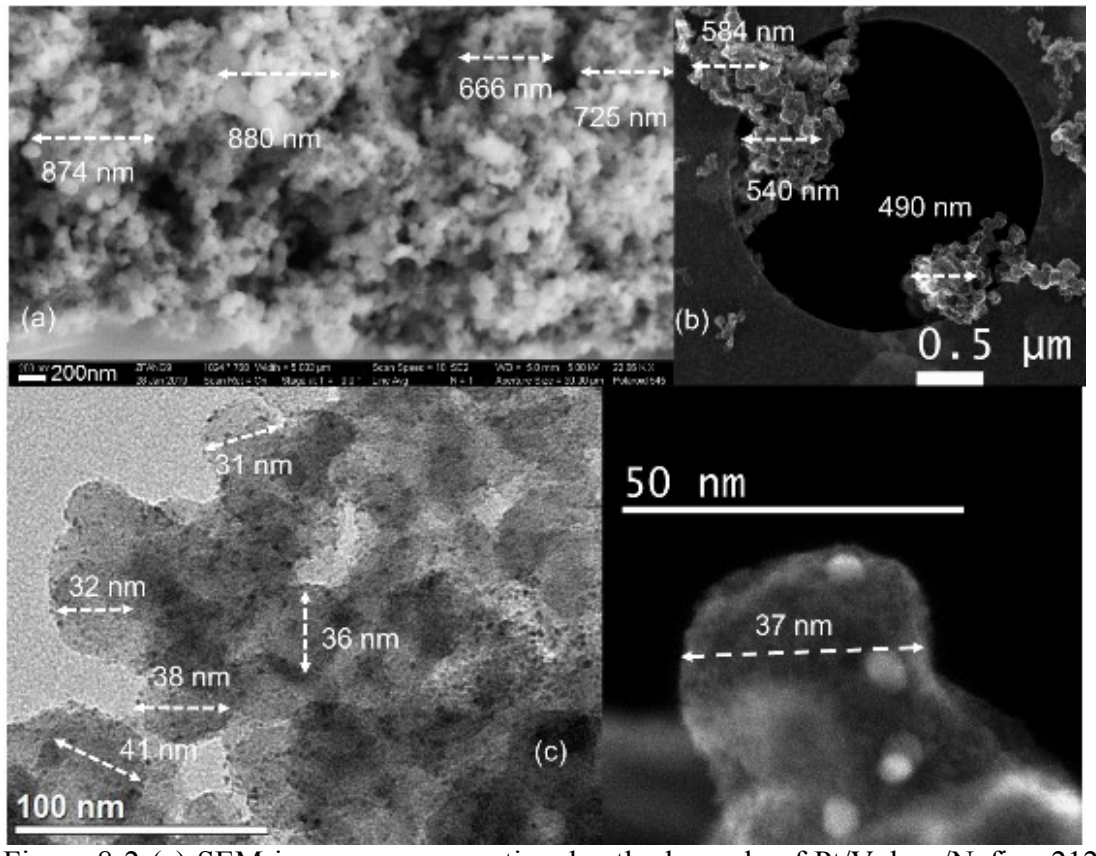

Figure 8-2 (a) SEM image a cross-sectional cathode made of Pt/Vulcan/Nafion 212, (b) secondary electron (SE) image from STEM measurement of Vulcan (3.8 atom%N by XPS)/Nafion 212, (c) TEM image of Vulcan/Nafion 212 ionomer, and d) SE image from TEM measurement of Pt/Ketjen black/Nafion 212. All of the samples have I/C ratio = 0.65 $\pm$ 0.02.

The ionomer thickness values found in the literature vary greatly, and there are no accepted standard techniques to measure it. In fact, the assumption that the ionomer completely covers the support that is described with a single parameter of thickness has not been verified. Here, a different line is pursued—the agglomerate model is modified with partial ionomer coverage shown in Figure 8-2 b. It is worth exploring if the observed geometries of the catalyst layer, such as the carbon particle size （~40 nm） via electron microscopy, can be used in the model to approximate the fuel cell performance.

In this chapter, two approaches for modification of the agglomerate model with partial ionomer coverage are explored. First, the ionomer coverage is simply incorporated in ORR kinetics with the agglomerate size remaining the same as Setzler and Fuller. Second, a multi-process transport for oxygen through carbon particles with or without ionomer coverage is developed. The location of Pt particles is also factored in for the difference in Pt distributions in Vulcan and Ketjenblack (KB) carbon supports. The experimental ionomer coverage values determined from STEM/EDS analysis in the section 7.3 Ionomer Coverage are used. The effect of the ionomer coverage on 1) cell performance at high-current density region and 2) mass-transfer resistance of CCL is investigated.

8.2 Direct Incorporation of Ionomer Coverage in ORR Kinetics

Since the electrochemical reaction requires the triple-phase boundaries in the cathode (ionomer, oxygen, and catalyst), the agglomerate without ionomer coverage is assumed to be inactive. The first scenario is an incorporation of ionomer coverage in surface ORR rate expression in Setzler's model and it is modified to

$$r_{ORR} = x_{i,surf}\, k_0 \left(\frac{p_{O_2}}{p_{ref}}\right)^m \Gamma_v \exp\left(-\frac{\alpha_{0c} F}{RT}\left(\Phi_1 - \Phi_2 - U^\theta\right)\right) \tag{8.2}$$

where $x_{i,surf}$ is the fraction of ionomer surface coverage, k_0 is the Butler-Volmer rate constant, Γ_v is the vacant catalytic sites, and the other terms can be found in LIST OF SYMBOLS AND ABBREVIATIONS section.

The second scenario is treating the ionomer coverage as a volumetric value and adds it to the macroscopic homogeneous volumetric reaction rate, j_{ORR}

$$j_{ORR} = x_{i,surf}\, \eta\, k'\left(P_{O_2,f}\right)^m \left(1 - \varepsilon_g\right)\left(1 - \frac{d_f}{R_{agg}}\right) \tag{8.3}$$

where η is the effectiveness factor describing the ratio of the average rate of reaction in the absence of mass-transfer limitation, k' is the equivalent homogenous rate constant, and other terms can be found in LIST OF SYMBOLS AND ABBREVIATIONS section. It is worth noting that in the equivalent homogeneous rate constant expression shown in eq. (8.4), the r_{ORR} does not contain the $x_{i,surf}$ term.

$$k' = \frac{a_{Pt}\, r_{ORR}}{\left(P_{O_2}\right)^m} \tag{8.4}$$

The simulated polarization curves for KB show an additional polarization of about 30 mV in the kinetics region compared to the simulation without accounting for the ionomer coverage term, $x_{i,surf}$, as illustrated by Figure 8-3b. It is worth noting that the difference in cell potentials between using the ionomer coverage in surface and volumetric reaction rate is minimal at low current densities (<0.5 A/cm^2) and the voltage loss increases significantly at high current densities (90 mV drop at the limiting current). This shows the importance of ionomer coverage in the CCL for high current densities, but its specific

impact on mass-transfer resistance needs other formulations. In addition, the plot reveals the insufficient resistance formulation in the Setzler and Fuller model. The experimental KB cell performance is significantly lower than the simulated performance at high currents, even though the physical and electrochemical parameters such as Pt loading, electrode thickness, ECSA, etc., are accounted for.

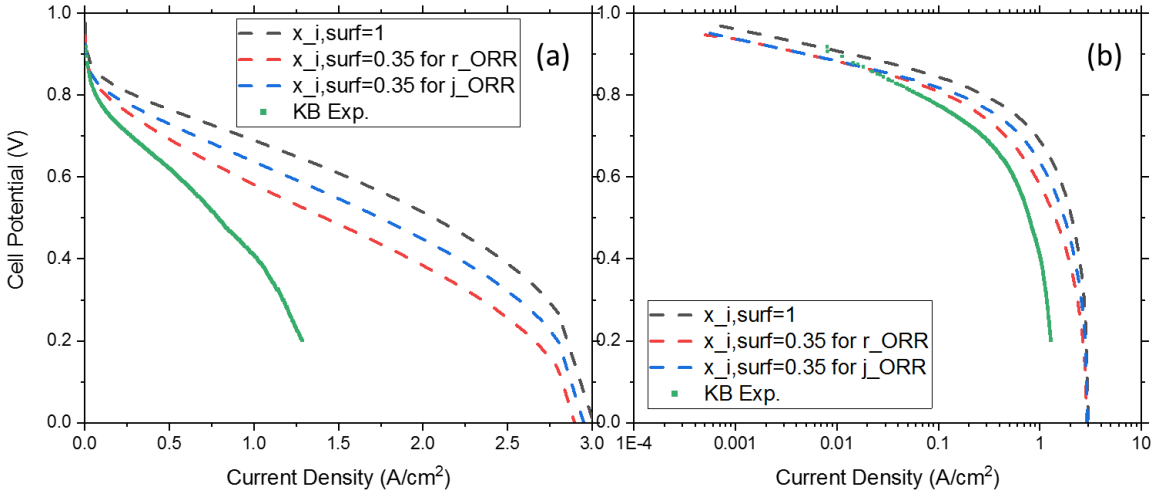

Figure 8-3 Simulated polarization curves for full and partial ionomer coverage using the agglomerate model (radius = 420 nm and ionomer film thickness = 27 nm) and the experimental polarization curve of Pt/KB at the operating condition of Air, 80 °C, 100%RH, and 150 kPa_{abs} at (a) linear and (b) log scales. Note: ohmic resistance is not corrected in (b).

8.3 Incorporation of Local Gas Transport and Resistance

Researchers have recently considered the addition of local gas transport to the classical agglomerate models. Mashio et al. modeled local gas transport process in the vicinity of the Pt surface and considered Pt particles both on the surface and inside the carbon support.[16] In addition, the authors employed an ionomer coverage parameter in the classical agglomerate model. The incorporation of local gas transport was found to improve the model's agreement with the experimentally measured transport resistance and that interfaces between ionomer/Pt and water/Pt interfaces contribute the most the local

transport resistance. However, the authors had to lower the oxygen permeation coefficients in ionomer and in water by a factor 5 to 20 to match the experimental transport resistance. Schuler et al. employed the agglomerate model and hydrogen limiting current technique and they concluded that the Knudsen resistance and diffusional resistance of oxygen in the ionomer instead of the interfaces (Pt/ionomer and ionomer/gas) account for the most of the total CCL transport resistance (50% to 70%).[21] The conclusion contrasts with the results of an earlier publication by the same research group.[1] In addition, the authors did not consider partial ionomer coverage or the porosity of the primary carbon particle. Darling *et al*. formulated agglomerate models for oxygen transport resistance in both high-surface (KB) and low-surface carbon support (Vulcan).[17, 18] They found that the nanoscale contributions to oxygen transport resistance are five times higher in KB than Vulcan, while the ratio of CCL transport resistances made of these two types of carbon support is only 1.4. However, the authors only considered complete ionomer coverage.

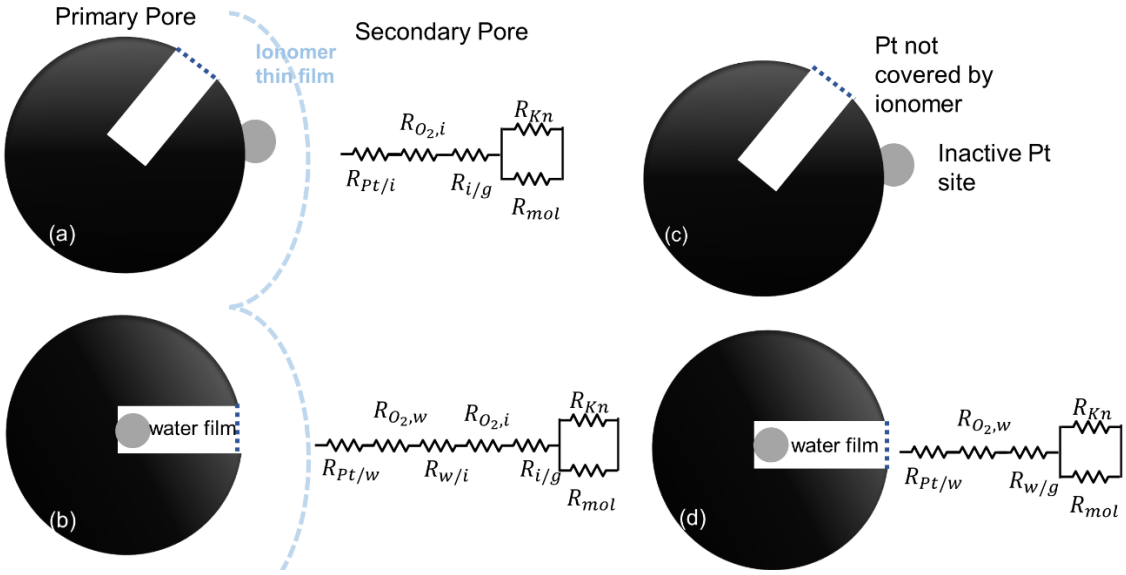

Figure 8-4 (a) Transport with Pt on the surface of the carbon primary particle covered by ionomer, b) transport with Pt inside carbon primary pore covered by ionomer, c) inactive Pt site without ionomer coverage and d) transport with Pt inside carbon primary pore filled with water film and the carbon particle without ionomer coverage.

In this study, four configurations of oxygen transport in the CCL are proposed and shown in Figure 8-4a, where $R_{Pt/i}$ is the interfacial resistance due to interaction between Pt and sulfonate in the ionomer, $R_{O_2,i}$ is the diffusional resistance of oxygen in the ionomer, $R_{i/g}$ is the dissolution resistance between ionomer and gas, R_{Kn} is the Knudsen diffusion resistance in the secondary pores of the CCL, and R_{mol} is the molecular diffusion resistance in the secondary pores of the CCL. In Figure 8-4b, the additional terms, $R_{Pt/w}$, $R_{O_2,w}$, and $R_{w/i}$ denote interfacial resistance between Pt and water, diffusional resistance of oxygen in water, and dissolution resistance between water and ionomer, respectively. It is worth noting that of all these resistances, only R_{mol} is pressure-dependent. The local transport resistance includes all but R_{mol} and R_{Kn}. The followings are a summary of main assumptions in this study:

1. Primary pores of carbon support are filled with liquid water under normal operating condition either with or without ionomer coverage
2. In the secondary pores of CCL, only water vapor is present, and thus transport through the gas phase is considered
3. Pt particles on the surface of carbons support without ionomer coverage are inactive
4. The sum of interfacial resistances at gas/water and water/Pt is similar to the sum of interfacial resistances at gas/ionomer and ionomer/Pt.
5. The thickness of ionomer thin film is constant despite different ionomer coverage

For the first assumption, although the water saturation of the primary pore is not necessarily one at high RH, the saturation is still high. Researchers have used theoretical studies to show[22] or have assumed[16, 18] that the primary pores of carbon support are filled

with water at high RH. Platinum particles in these water-filled pores without ionomer may remain active due to weak proton conduction via condensed water.[21] Hence, in this work, the primary pores where Pt particles reside are assumed to be filled with water and the Pt particles are active at normal operating condition (80 °C and 100%RH). The active Pt particles are in the configurations (a) (b) and (d) in Figure 8-4. On the other hand, the Pt particles on the surface of carbon support without ionomer coverage are rendered inactive as illustrated in Figure 8-4 (c). At low humidity and low oxygen condition (80 °C, 62%RH, 4vol% O_2 in N_2) of the limiting current tests by Baker *et al.*, the primary pores of carbon support are assumed to be free of water thus rendering the Pt sites inside the pores inactive.[4] The equivalent resistance circuits for normal and limiting-current operating conditions are shown in Figure 8-5. The fraction of ionomer coverage, $x_{i.surf}$, and the fraction of Pt particles on the surface of carbon support, $x_{Pt.surf}$, are accounted for in the model.

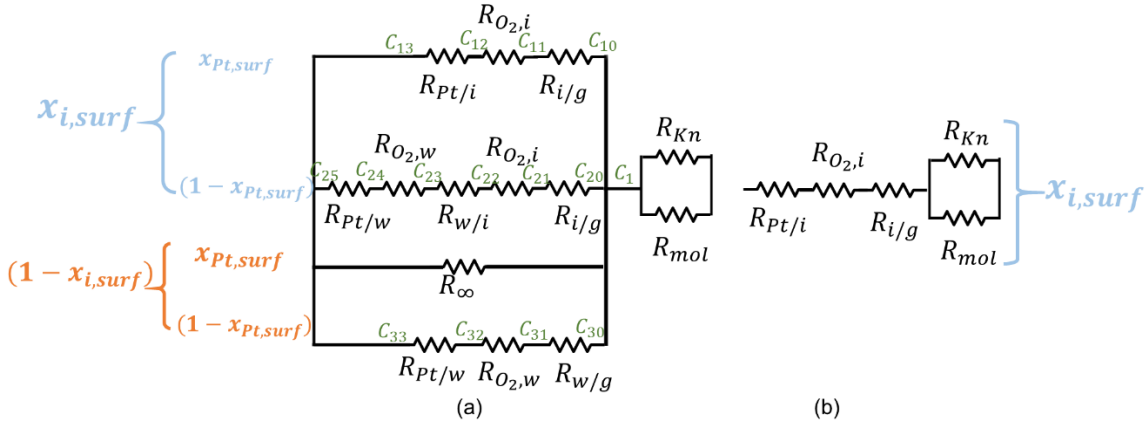

Figure 8-5 Circuit model for a) normal operating condition (80 °C, 62%RH, air) and b) dry limiting current condition (80 °C, 62%RH, 4vol% O_2 in N_2). x_{ISC} is fraction of ionomer coverage on carbon support and Y is the fraction of Pt particles on the surface of carbon support.

First, the pressure-dependent portion of the CCL transport resistance is derived from the 1-D equation of continuity for oxygen at limiting current using Taylor's expansion and it becomes

$$R_{O_2,P-D}^{CL} = \frac{\ell^{CL}}{3\, D^{CL,eff}} \tag{8.5}$$

where ℓ_{CL} is the catalyst layer thickness; and the effective catalyst layer oxygen diffusivity, $D^{CL,eff}$, is based on oxygen diffusivity in cathode gas mixture and the Knudsen diffusion coefficient.[21] The oxygen diffusivity in a gas mixture is estimated from the binary diffusivities D_{j-O_2}, and mole fractions x_j.

$$D_{O_2} = \left(\sum_j \frac{x_j}{D_{j-O_2}} \right)^{-1} \tag{8.6}$$

Knudsen diffusivity is calculated as

$$D_{Kn,O_2} = \frac{d_{sp}}{3} \sqrt{\frac{8RT}{\pi M_{O_2}}} \tag{8.7}$$

Then the D_{CL}^{eff} is calculated as

$$D^{CL,eff} = \frac{\varepsilon_g^{CL}}{\tau^{CL}} \left(\frac{1}{D_{O_2}} + \frac{1}{D_{Kn,O_2}} \right)^{-1} \tag{8.8}$$

Therefore, the transport resistance in the secondary pores of CCL becomes

$$R_{O_2,P-D}^{CL} = \frac{\ell^{CL}}{3} \frac{\tau^{CL}}{\varepsilon_g^{CL}} \left(\frac{1}{D_{O_2}} + \frac{1}{D_{Kn,O_2}} \right) \tag{8.9}$$

At the ionomer/gas interface, through ionomer, and at Pt/ionomer interface, the oxygen fluxes at agglomerate-scale, $n_{O_2,1}$, are

$$n_{O_2,1} = -k_{i/g}\, (C_{10} - C_{11}) \tag{8.10}$$

$$n_{O_2,1} = -\frac{D_{O_2,i}\left(R_{agg} + d_f\right)}{R_{agg}} \frac{(C_{11} - C_{12})}{d_f} \tag{8.11}$$

$$n_{O_2,1} = -k_{\frac{Pt}{i}}\, (C_{12} - C_{13}), \tag{8.12}$$

where $k_{i/g}$ is mass-transfer coefficient for oxygen permeation at ionomer/gas interface and $k_{Pt/i}$ is mass transfer coefficient at the Pt/ionomer interface. Since all of the oxygen fluxes are equal to each other at steady state, the sum of the local transport resistance in the configuration (a) of Figure 8-4 or the top of the 3 parallel circuits in Figure 8-5 becomes,

$$R_{O_2,1} = \frac{(C_1 - C_{13})}{n_{O_2,1}}, \tag{8.13}$$

where $x_{i,surf}$ is the fraction of ionomer surface coverage, $x_{Pt,surf}$ is the fraction of Pt particles on the surface of the carbon support, and C_1 is the oxygen concentration in the gas phase on top of the ionomer thin film. C_1 is related to C_{10} by Henry's law. After rearrangement and assuming C_{13} to be negligible at limiting current, the resistance $R_{O_2,1}$ becomes

$$R_{O_2,1} = \frac{H_{O_2,i}}{RT}\left[\frac{1}{k_{i/g}} + \frac{1}{k_{Pt/i}} + \frac{R_{agg}\, d_f}{(R_{agg} + d_f)\, D_{O_2.i}}\right], \tag{8.14}$$

where the sum of $\frac{1}{k_{i/g}}$ and $\frac{1}{k_{Pt/i}}$ have been determined by Kudo *et al*. be 135 s/m by varying the ionomer thin film thickness. Furthermore, Jinnouchi *et al*. used transition state theory-based molecular dynamics simulation and found that the O_2 permeation flux in unit of A-m^{-2}Pa^{-1} (not the same as $n_{O_2,1}$ in unit of mol-m^{-2}s^{-1}) at the Pt/ionomer interface is about 1/100 of the flux at the ionomer/gas interface. Based on this, the $k_{Pt/i} = (C_{10} - C_{11})/(C_{12} - C_{13})k_{i/g} = 1/100\, k_{i/g}$.

The transport resistance for oxygen diffusing all the way to Pt sites in the pores of carbon support shown in the configuration (b) (or the middle circuit of the three parallel circuits in Figure 8-5) is derived similarly as that for the configuration (a). However, two derivations by Darling *et al*. are employed to model resistance from C_{22} to C_{24}, including

entry transport and one-dimensional diffusion in the water-filled primary pore.[18] Thus, the transport resistance in configuration (b), $R_{O_2,2}$ becomes

$$R_{O_2,2} = \frac{H_{O_2,i}}{RT}\left[\frac{1}{k_{i/g}} + \frac{1}{k_{Pt/w}} + \frac{R_{agg}d_f}{(R_{agg}+d_f)D_{O_2.i}} + \frac{\pi d_{pore}H_{O_2,i}}{2D_{O_2,i}\,RT} + \frac{4d_{Pt}^2\ell_{pore}H_{O_2,w}}{d_{pore}^2\,D_{O_2,w}\,RT}\right]. \tag{8.15}$$

For oxygen diffusion to Pt sites on the surface of carbon support that is absent of ionomer as shown in configuration (c) of Figure 8-4, the Pt sites are assumed to be inactive and the local transport resistance, R_∞, is thus infinitely large. For pores of carbon support that are absent of ionomer coverage shown in configuration (d) of Figure 8-4, the transport resistance, $R_{O_2,3}$ is

$$R_{O_2,3} = \frac{H_{O_2,w}}{RT}\left[\frac{1}{k_{w/g}} + \frac{1}{k_{Pt/w}} + \frac{4d_{Pt}^2\ell_{pore}}{d_{pore}^2\,D_{O_2,w}}\right], \tag{8.16}$$

where the interfacial resistances at water/gas and Pt/water locations are unknown and are assumed to be the same as the sum of ionomer/gas and Pt/ionomer interfacial resistances. Hence, the total transport resistance for CCL becomes

$$R_{O_2}^{CL} = R_{O_2,P-D}^{CL} + \frac{1}{A_{Pt}}\left[\frac{1}{\frac{R_{O_2,1}}{x_{i,surf}x_{Pt.surf}}} + \frac{1}{\frac{R_{O_2,2}}{x_{i,surf}(1-x_{Pt.surf})}} + \frac{1}{\frac{R_{O_2,3}}{(1-x_{i,surf})(1-x_{Pt.surf})}}\right]^{-1}, \tag{8.17}$$

where the third path with inactive Pt in Figure 8-5a is not shown in the equation because the inverse of it is zero.

Table 8-2 Model parameters sourced from the literature, measured/calculated from known quantities, or assumed.

Symbol	Meaning	Value	Source
A_{Pt}	Effective surface area of Pt per unit area of MEA	44 m^2_{Pt}/m^2_{MEA}	Measured
d_f	Thickness of ionomer thin film	7 nm	Lopez-Haro[19]
d_{Pt}	Diameter of Pt particle	3.4 nm	Measured
d_{pore}	Diameter of carbon support pore	4 nm	Darling[18]
d_{sp}	Diameter of secondary pore for Knudsen diffusivity	40 nm	Setzler[23]
$D_{O_2,i}$	Oxygen diffusivity in ionomer	$1.22\text{x}10^{-10}$ m^2/s	Lin[24] and Setzler[10]
$D_{O_2,w}$	Oxygen diffusivity in liquid water	$4.90\text{x}10^{-9}$ m^2/s	Harris[25]
$H_{O_2,i}$	Henry's constant of O_2 in ionomer thin film	$2.04\text{x}10^4$ Pa-m^3/mol	Lin[24] and Setzler[10]
$H_{O_2,w}$	Henry's constant of O_2 in water thin film	$1.26\ \text{x}10^6$ Pa-m^3/mol	Mashio[16]
$\frac{1}{k_{i/g}}+\frac{1}{k_{Pt/i}}$	Sum of the interfacial resistances at ionomer/gas and at Pt/ionomer	135 s/m	Kudo[26]
$\frac{1}{k_{i/g}}+\frac{1}{k_{Pt/w}}$	Sum of the interfacial resistances at ionomer/gas and at Pt/water	135 s/m	Assumed
$\frac{1}{k_{w/g}}+\frac{1}{k_{Pt/w}}$	Sum of the interfacial resistances at water/gas and at Pt/water	135 s/m	Assumed
ℓ_{pore}	Depth of carbon support pore	4 nm	Darling[18]
R_{agg}	Agglomerate radius	40 nm	Measured
$x_{i.surf}$	Fraction of carbon support covered by ionomer	0.35 to 0.45	Measured
$x_{Pt.surf}$	Fraction of Pt on the surface of carbon support	0.95 for Vulcan 0.38 for KB	Kongkanand[27]
ε_g^{CL}	Porosity of gas pore	0.4	Star[28]
τ^{CL}	Tortuosity of gas pore	1.61	Star[28]

The $R_{O_2}^{CL}$ was compared to the CCL transport resistance, $R_{O_2,Setzler}^{CL}$ obtained from the model by Setlzer and Fuller and the latter was calculated by

$$R_{O_2,Setzler}^{CL}=\frac{4P_{O_2}^{CL}F}{R\,T\,i_{\lim}}, \tag{8.18}$$

where $P_{O_2}^{CL}$ is the oxygen partial pressure taken at CCL|GDL interface, i_{lim} is the limiting current density at normal operation condition (100%RH, 80°C, Air). Figure 8-6 shows an inverse relationship between the fraction of ionomer coverage and the total O_2 transport resistance in the CCL for both high-surface-area carbon KB and low-surface-area Vulcan. The model reveals that the ionomer coverage does not significant affect the total transport resistance of the CCL after $x_{i.surf}$ exceeds about 0.5. This ionomer coverage onset value is similar to those determined using STEM/EDS technique between 0.35 and 0.45 listed in Table 7-5. In addition, the ratio of Pt/KB resistance to Pt/V resistance is between 1.3 and 1.7, which matched the range of 1.06 to 1.7 reported by other researchers, who used a more simplified agglomerate model.[18]

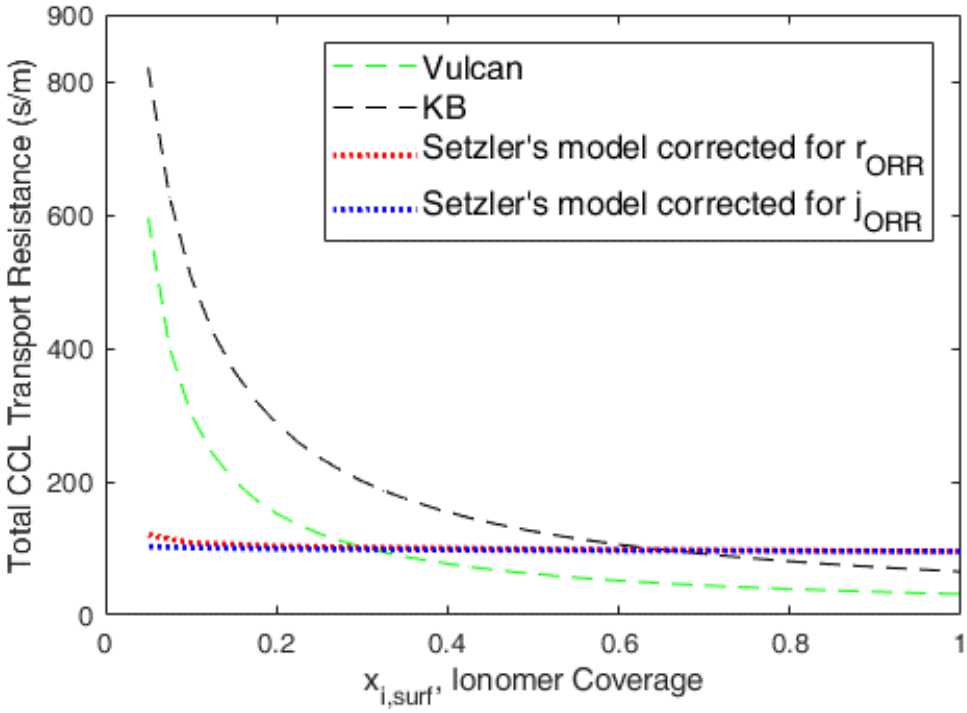

Figure 8-6 Simulated total CCL transport resistance for Vulcan and KB (dashed lines) using this model compared to correcting ionomer coverage in Setzler's model for r_{ORR} and j_{ORR} (dotted lines).

The following discussion focuses on comparing and contrasting the modeling results

with those by Setzler and Fuller's model. First, unlike the liquid water films in the carbon pores assumed in this model, Setzler and Fuller's model is strictly one-phase (gaseous). In addition, 40 nm agglomerate size and 7 nm ionomer thickness are used in this model compared to 420 nm and 27 nm employed in Setzler and Fuller's model. Despite the difference, the simulated total CCL transport resistance using Setzler and Fuller's model have matched the simulated values of this model (~96 s/m) at $x_{\mathrm{i,surf}}$ = 0.7 for KB and at $x_{\mathrm{i,surf}}$ = 0.35 for Vulcan. This match suggests that at Setzler and Fuller's model can account for sufficient transport resistance of the CCL only at high ionomer coverages, whereas at lower ionomer coverage, which was observed in KB samples (section 7.3), additional local transport resistance needs to be factored in. If the 40 nm agglomerate size and 7 nm ionomer thickness are input in the Setzler and Fuller's model, the transport resistance of CCL is calculated to be only 20 s/m, which is about 1/3 of the resistance using the original agglomerate dimensions for KB. The discrepancy indicates that the local transport resistance accounts for the majority of the CCL transport resistance. It also suggests the use of carbon primary particle dimensions in the agglomerate model is applicable when the local transport is formulated.

On the other hand, when the ionomer coverage term were directly incorporated in the rate or flux expressions (discussed in section 8.2), Figure 8-6s shows the minimal effect of ionomer coverage on the transport resistance, which are increased by 25 and 15 s/m for the rate and flux expressions between 0.05 ionomer coverage to full ionomer coverage. The increases of 25 and 15 are insignificant compared to 750 s/m increase for KB carbon support from 0.05 ionomer coverage to full ionomer coverage. In addition to insensitive change of transport resistance to the ionomer coverage, the direct-incorporation approach

also appears to underestimate the transport resistance compared to the equivalent circuit model approach. The two differences (insensitivity and underestimation) between the two models implicate that: 1) the direct incorporation of ionomer in the rate expressions is insufficient, and 2) the simulated polarization will be substantially lowered if the local transport resistance is added to the Setzler and Fuller's model, which may better match the experimental cell performance.

Variable Ionomer Film Thickness

A major assumption in the model described in section 8.3 is a uniform ionomer thickness for the full range of ionomer coverage ($x_{i,surf} \in [0,1]$). The uniform ionomer thickness is improbable considering the conversation of mass. Furthermore, researchers have reported non-uniform distribution of ionomer in the carbon support.[20, 29, 30] Hence, it is worth adding a variable thickness of the ionomer thin film in the model. The thickness, d_f, varies with the ionomer coverage relative to a reference thickness of 7.2 nm at $x_{i,surf}$ = 79.5%.[19] The ionomer film thickness is $0.795/x_{i,surf}$*7.2 based on conservation of mass. Figure 8-7 show that a thicker ionomer thin film occurs at low ionomer coverage and increases the CCL transport resistance from that predicted by uniform ionomer thickness.

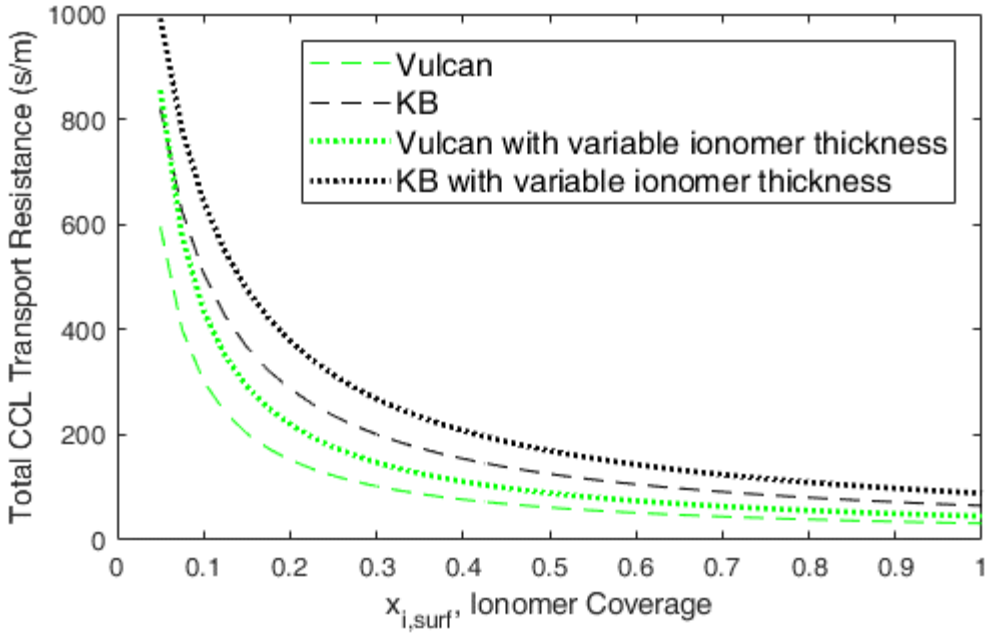

Figure 8-7 Simulated total CCL transport resistance as a function of ionomer coverage for Vulcan and KB carbon support with or without variable ionomer thickness.

8.4 Conclusion

Three different formulations for incorporating fraction of ionomer coverage are explored. Using the direct incorporation in ORR reaction rate or flux, transport resistances are insignificantly affected by the ionomer coverage. On the other hand, when local oxygen transport is added to the transport model for oxygen in the CCL, the transport resistance scales in a 1/x shape with the ionomer coverage for both KB and Vulcan carbon supports. Furthermore, when a variable thickness of the ionomer is utilized, the trend of the decreasing transport resistance with ionomer coverage remains the same. The new transport model supports the use of the dimensions of primary carbon particles (about 40 nm in diameter) in the agglomerate model, whereas the majority of prior models use much larger agglomerate sizes (100 nm to 2,000 nm).

8.5 References

1. N. Nonoyama, S. Okazaki, A. Z. Weber, Y. Ikogi, and T. Yoshida, *Journal of The Electrochemical Society,* **158** (4), B416-B423 (2011).

2. A. Kongkanand and M. F. Mathias, *The journal of physical chemistry letters,* **7** (7), 1127-1137 (2016).

3. A. Z. Weber and A. Kusoglu, *Journal of Materials Chemistry A,* **2** (41), 17207-17211 (2014).

4. D. R. Baker, D. A. Caulk, K. C. Neyerlin, and M. W. Murphy, *Journal of The Electrochemical Society,* **156** (9), B991-B1003 (2009).

5. T. A. Greszler, D. Caulk, and P. Sinha, *Journal of The Electrochemical Society,* **159** (12), F831-F840 (2012).

6. F. B. Spingler, A. Phillips, T. Schuler, M. C. Tucker, and A. Z. Weber, *International Journal of Hydrogen Energy,* **42** (19), 13960-13969 (2017).

7. F. C. Cetinbas, X. Wang, R. K. Ahluwalia, N. N. Kariuki, R. P. Winarski, Z. Yang, J. Sharman, and D. J. Myers, *Journal of The Electrochemical Society,* **164** (14), F1596-F1607 (2017).

8. S. Ridge, R. E. White, Y. Tsou, R. Beaver, and G. Eisman, *Journal of the Electrochemical Society,* **136** (7), 1902 (1989).

9. T. E. Springer, T. Zawodzinski, and S. Gottesfeld, *Journal of the Electrochemical Society,* **138** (8), 2334-2342 (1991).

10. B. P. Setzler and T. F. Fuller, *Journal of The Electrochemical Society,* **162** (6), F519-F530 (2015).

11. F. Jaouen, G. Lindbergh, and G. Sundholm, *Journal of The Electrochemical Society,* **149** (4), A437-A447 (2002).

12. Q. Guo and R. E. White, *Journal of The Electrochemical Society,* **151** (4), E133-E149 (2004).

13. M. Secanell, K. Karan, A. Suleman, and N. Djilali, *Electrochimica Acta,* **52** (22), 6318-6337 (2007).

14. A. Kulikovsky, *Journal of The Electrochemical Society,* **164** (4), F379-F386 (2017).

15. L. Xing, X. Liu, T. Alaje, R. Kumar, M. Mamlouk, and K. Scott, *Energy,* **73** 618-634 (2014).

16. T. Mashio, H. Iden, A. Ohma, and T. Tokumasu, *Journal of Electroanalytical Chemistry,* **790** 27-39 (2017).

17. R. M. Darling, *Journal of The Electrochemical Society,* **165** (9), F571 (2018).

18. R. M. Darling and S. Burlatsky, *Journal of the Electrochemical Society,* (2020).

19. M. Lopez-Haro, L. Guétaz, T. Printemps, A. Morin, S. Escribano, P.-H. Jouneau, P. Bayle-Guillemaud, F. Chandezon, and G. Gebel, *Nature communications,* **5** (2014).

20. Y.-C. Park, H. Tokiwa, K. Kakinuma, M. Watanabe, and M. Uchida, *Journal of Power Sources,* **315** 179-191 (2016).

21. T. Schuler, A. Chowdhury, A. T. Freiberg, B. Sneed, F. B. Spingler, M. C. Tucker, K. L. More, C. J. Radke, and A. Z. Weber, *Journal of The Electrochemical Society,* **166** (7), F3020 (2019).

22. R. F. De Morais, P. Sautet, D. Loffreda, and A. A. Franco, *Electrochimica Acta,* **56** (28), 10842-10856 (2011).

23. B. P. Setzler. Georgia Institute of Technology, 2015.

24. G. Lin, W. He, and T. Van Nguyen, *Journal of the Electrochemical Society,* **151** (12), A1999 (2004).

25. K. R. Harris and L. A. Woolf, *Journal of the Chemical Society, Faraday Transactions 1: Physical Chemistry in Condensed Phases,* **76** 377-385 (1980).

26. K. Kudo, R. Jinnouchi, and Y. Morimoto, *Electrochimica Acta,* **209** 682-690 (2016).

27. A. Kongkanand, V. Yarlagadda, T. R. Garrick, T. E. Moylan, and W. Gu, *ECS Transactions,* **75** (14), 25-34 (2016).

28. A. G. Star and T. F. Fuller, *Journal of The Electrochemical Society,* **164** (9), F901-F907 (2017).

29. D. Susac, V. Berejnov, A. P. Hitchcock, and J. Stumper, *ECS Transactions,* **41** (1), 629-635 (2011).

30. D. A. Cullen, R. Koestner, R. Kukreja, Z. Liu, S. Minko, O. Trotsenko, A. Tokarev, L. Guetaz, H. Meyer, and C. Parish, *Journal of The Electrochemical Society,* **161** (10), F1111-F1117 (2014).

CHAPTER 9. RECOMMENDATIONS

9.1 Recommendations for Wettability Study

The wettability study concluded with the small decreases in hydrophobicity of the CCL with carbon corrosion when the cell performance dropped below the DOE's 10% target. Only one type of commercial MEAs made of Vulcan at 0.3 mg_{Pt}/cm^2 with 46wt% to 50wt% Pt/C was used in the study. The Pt loading was much higher than the DOE's target of 0.1 mg/cm^2 or other MEAs in the recent publications (past 3 years), which typically use electrocatalysts with lower Pt weight percentage (i.e. 20 wt% Pt/C). Thus, the study can be expanded to MEAs with lower Pt loadings. A challenge to the expansion of the study lies in the expensive, time-consuming FIB-SEM experiments for the determination of porosities. In addition, since the C-F bond is a key part of the surface analysis and the chemical elements of different CCL samples are the same, the future measurements of XPS survey scans are recommended to be reduced or omitted to minimize the radiation damage of ionomer. The high-resolution scans of fluorine and carbon should be performed first.

9.2 Recommendations for Surface Functionalization Study

The surface functionalization study concluded with the improvements of mass activity and ionomer distribution on the carbon support after functionalization with nitrogen-containing surface groups as well as the adverse effect of the surface sulfonate groups on the cell performance. In terms of durability, it was found that the surface functionalization increased carbon loss and accelerated performance loss for two types of commercial carbon supports, Vulcan and KB, whereas the durability of the highly graphitic. Ammonia scheme

2 functionalization had been performed at elevated temperatures from 400 °C to 700 °C; however despite the improved durability (as evidenced from lower carbon loss), the elevated temperatures lowered the initial cell performance compared to the scheme 2 reacted at 200 °C. It is recommended to further explore ways to improve the durability of functionalized Vulcan and KB carbon supports. For example, the carbon supports can be functionalized using the same scheme-2 procedure with an addition of an annealing step in 2% H_2 in N_2 at elevated temperatures to reduce surface oxides while possibly retaining the surface nitrogen functional groups.

9.3 Recommendations for Transport Modeling

The equivalent-circuit formulations for the agglomerate model supports the applicability of the use of primary carbon dimensions with local gas transport in the agglomerate model. In this study, two interfacial resistance parameters were assumed, whereas most of the individual resistance terms can be experimentally determined or estimated. In the future, in order to better validate the model with experimental data, a more comprehensive set of tests can be performed.

Table 9-1 Sensitivity studies of transport resistances.

Experimental Variable	**Affected Term**	**How is it determined**
Gas pressure, p	R_{mol}	Changes with a factor of p
Molecular weight	R_{Kn}	Changes with $(MW)^{0.5}$
I/C ratio or ionomer thickness	$R_{i/g} + R_{Pt/i}$	y-intercept at zero I/C
Relative humidity	$R_{Pt/w} + R_{w/g}$	Possibly y-intercept of a CCL sample without ionomer
Pt loading in CCL	Sum of local transport resistance terms	Scales with 1/(roughness factor)

APPENDIX A.

A.1 Calculations of Transport Polarization from EIS

The mass-transport polarization is first calculated from Warburg impedance from EIS by fitting the experimental EIS to an equivalent circuit that consists of ohmic resistance (R_Ω), constant phase element (CPE), charge-transfer resistance (R_{ct}), and finite Warburg impedance (Z_W) as shown Figure A-1a. The fitting is performed in a Python file.

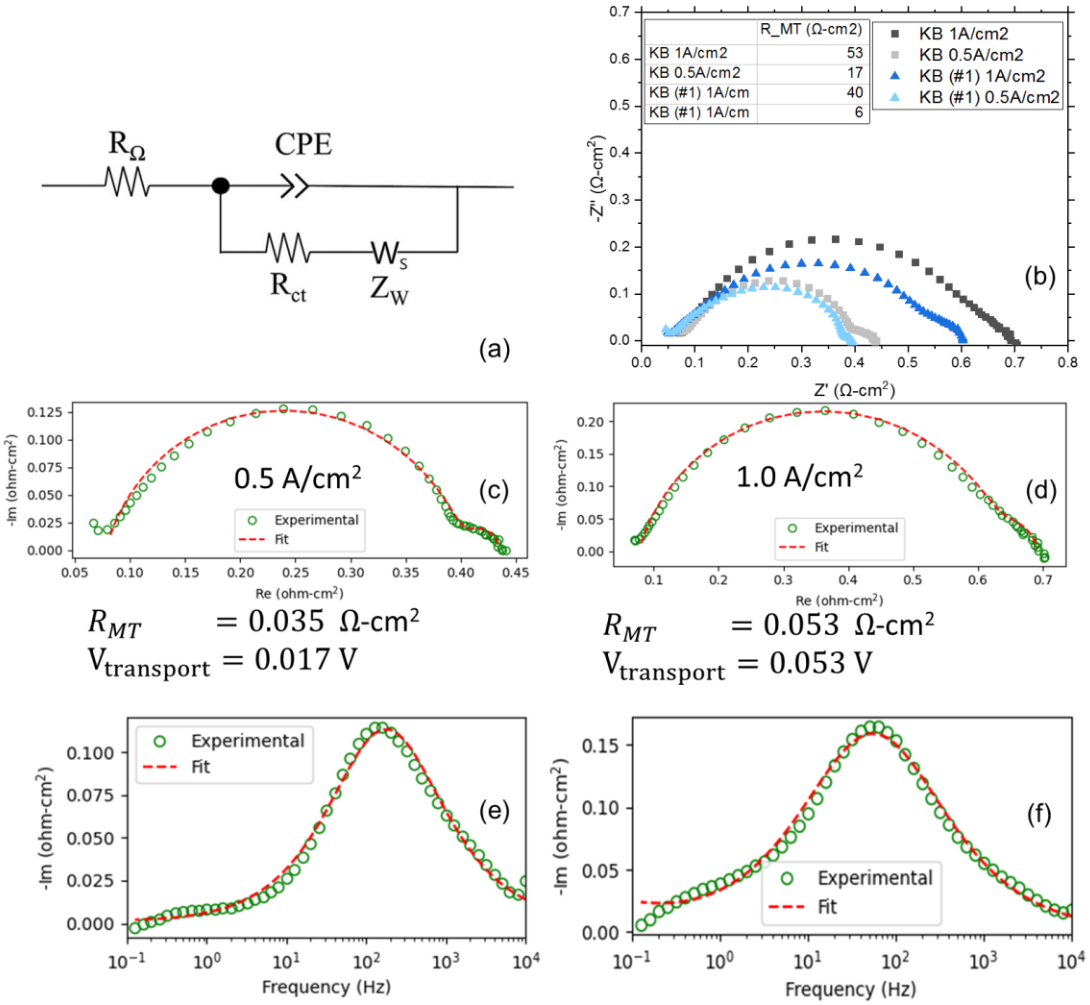

Figure A-1 (a) Equivalent circuit for fuel cells, b) experimental EIS of fuel cells made with 20% Pt/KB and 20% Pt/KB (scheme 1) at two different current densities, Nyquist and Bode plots of experimental and fitted EIS of fuel cell made with 20% Pt/KB catalyst at (c, e) 0.5 A/cm^2 and (d, f) 1.0 a/cm^2. The operating condition was 2 SLPM H_2/ 5 SLPM air, 80°C, 100% RH, 150 kPa_{abs}.

The mass-transfer resistance (R_{MT}) is calculated from the finite Warburg impedance,

$$Z_W = \frac{R_{MT}\, tanh(j\omega\tau)^{0.5}}{(j\omega\tau)^{0.5}} \quad (A.1)$$

Then the mass-transfer polarization is calculated by multiplying R_{MT} with current density at which the EIS is performed. The results were listed in the Table A-1. The EIS results further confirmed the trend observed in polarization curves.

Table A-1 Mass-transport polarization of KB and V samples calculated from EIS.

	Mass-Transport Polarization @ 0.5 A/cm^2 (mV)	**Mass-Transport Polarization @ 1.0 A/cm^2 (mV)**	**Mass-Transport Polarization @ 1.5 A/cm^2 (mV)**
KB	17	53	NA
KB (scheme 1)	6	40	NA
KB (scheme 2)	2	52	NA
KB (scheme 3)	30	Cell did not reach 1.0 A/cm^2	NA
V	<0.1	7	67
V (scheme 1)	<0.1	7	64
V (scheme 2)	<0.1	5	80
V (scheme 3)	<0.1	255	Cell did not reach 1.5 A/cm^2

The Python code is shown below.

```
import numpy as np
import matplotlib.pyplot as plt
import math

data = np.loadtxt(r'C:\Users\zfang9\Desktop\FC\MEA040\EIS91_05Acm.txt',
skiprows=1)
frequencies_long = data[:,0]
Z = 4.8*(data[:,1]+1j*data[:,2])
frequencies = frequencies_long[np.nonzero((frequencies_long <= 1e4) &
(frequencies_long >.1))]
Z = Z[np.nonzero((frequencies_long <= 1e4) & (frequencies_long >.1))]
Re = np.real(Z)
Im = -np.imag(Z)

from impedance.models.circuits import CustomCircuit
circuit='R0-p(CPE1,R1-Ws)' #for
initial_guess=[.09, 1e-5, 0.3, 1, .05, .1]
circuit = CustomCircuit(circuit, initial_guess=initial_guess)
circuit.fit(frequencies, Z)
Z_fit = circuit.predict(frequencies)
print(circuit)

fig=plt.figure()
ax = fig.add_subplot(1,1,1)
ax.plot(Re,Im,'o', color='green', mfc='none',  label='Experimental')
```

```
ax.plot(np.real(Z_fit)*1,-np.imag(Z_fit)*1,'--',color='red',label='Fit')
ax.set_aspect(aspect=1)
plt.xlabel('Re (ohm-cm$^2$)')
plt.ylabel('-Im (ohm-cm$^2$)')
plt.legend(facecolor='white', )  # , shadow=True, loc=2)#, title='title for
legend')

fig=plt.figure()
ax = fig.add_subplot(1,1,1)
ax.plot(frequencies,Im,'o', color='green', mfc='none',  label='Experimental')
ax.plot(frequencies,-np.imag(Z_fit)*1,'--',color='red',label='Fit')
ax.set_xscale('log')
plt.xlabel('Frequency (Hz)')
plt.ylabel('-Im (ohm-cm$^2$)')
plt.legend(facecolor='white', )  # , shadow=True, loc=2)#, title='title for
legend')
plt.xlim(0.1 , 1e4)
#plt.ylim(0, 5000)
plt.show()
```

A.2 Analysis and Calculations of Ionomer Coverage

A.2.1 Extraction of location data of STEM/EDS images via ImageJ

The goal of the first step is to determine the edges of carbon support. First, load the Z-contrast STEM image. Convert the image type from RGB to 8 bit. Then convert the image from pixels to unit of nm under *Analyze* tab and *Set Scale* command. Under the *Image* tab, adjust the threshold of the binarization (Crtl + Shift + T). The default algorithm may either underestimate or overestimate the size of the carbon support edge, so it is wise to manually adjust the grey scale ([0, 255]). Use *Wand tracing tool* to trace the edge of the carbon support. Then save the processed image as *XY Coordinates* in a text file. Lastly, copy and paste the coordinate data to an Excel spreadsheet to ensure the coordinates are continuous with the correct starting and ending points.

The second image processing step is to find the coordinates of the fluorine pixels. Load the EDS image. Convert the image type from RGB to 8 bit. Then convert the image from pixels to unit of nm under *Analyze* tab and *Set Scale* command. Under *Process* tab, use *Find Maxima* to select all the fluorine pixels. Then save as *XY Coordinates* in a text file.

Lastly, paste the coordinate data to the Excel spreadsheet containing the coordinates of the carbon support edge. It is necessary to remove the maxima that represent the scale bar instead of the actual F pixels in the EDS images.

A.2.2 Ionomer coverage analysis by STEM/EDS

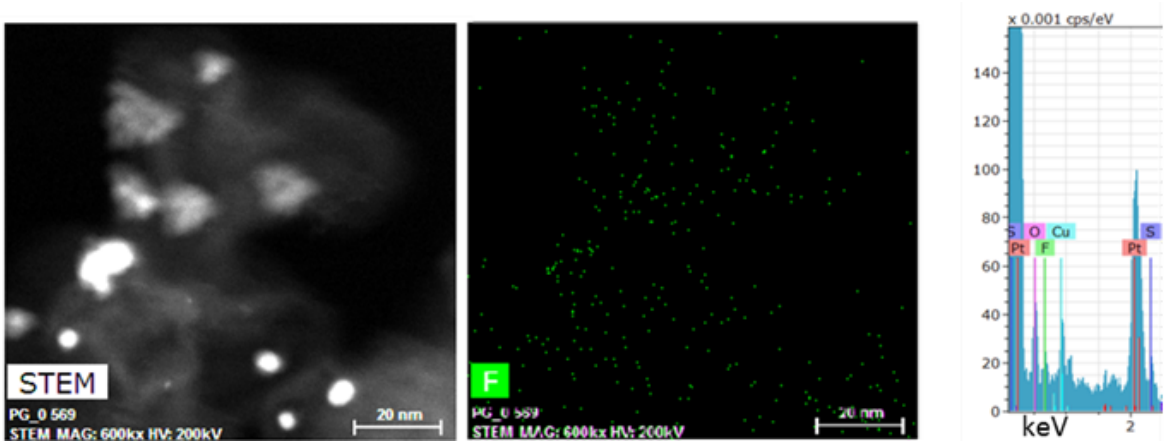

Figure A-2 (a) STEM image, b) F mapping by EDS, and c) the spectra of the EDS showing peaks of Pt, O, F, Cu, and questionable S due to the secondary peaks of Pt.

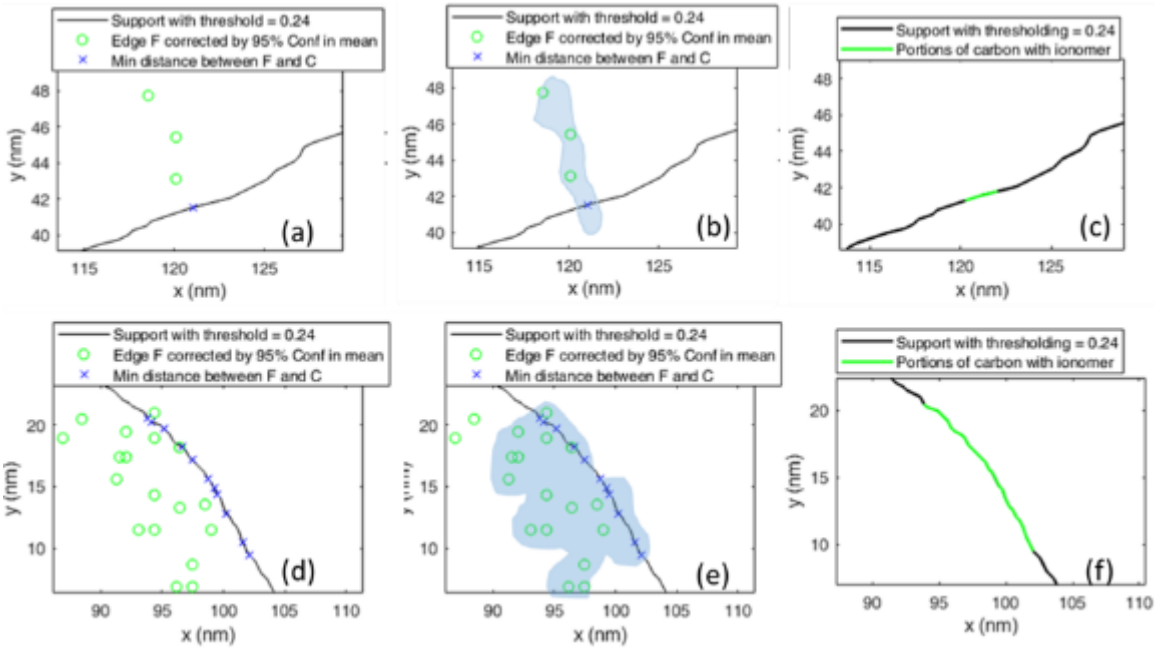

Figure A-3 (a) Three F pixels (o) and their nearest point (x) on the edge of the carbon support and (b) a possible way of ionomer distribution near the edge of the carbon support, (c) the calculated ionomer coverage on the carbon support for these three F pixels, (d) a common distribution of F pixels, (e) a possible way of ionomer distribution near the edge of the carbon support, and (f) the calculated ionomer coverage on the carbon support for

the F pixels in (d).

A.2.3 Selected results of ionomer coverage calculation

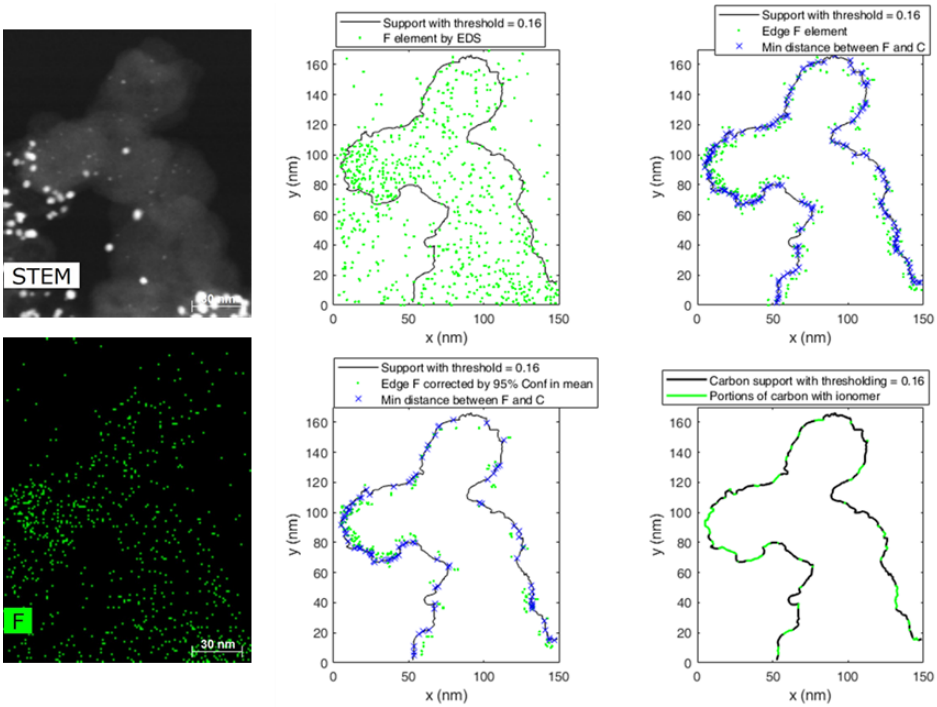

Figure A-4 Ionomer coverage of Pt/KB (pristine) = 20% for an I/C weight ratio of 0.38

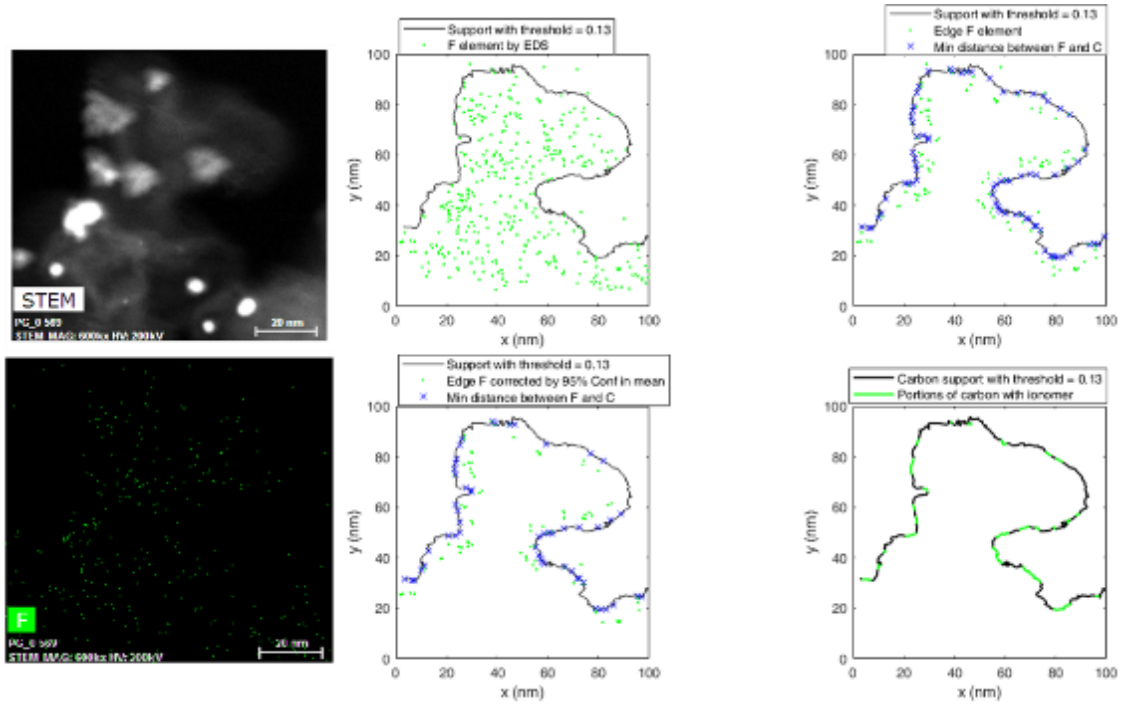

Figure A-5 Ionomer coverage of Pt/KB (pristine) = 16% for an I/C weight ratio of 0.66 $\pm$ 0.2

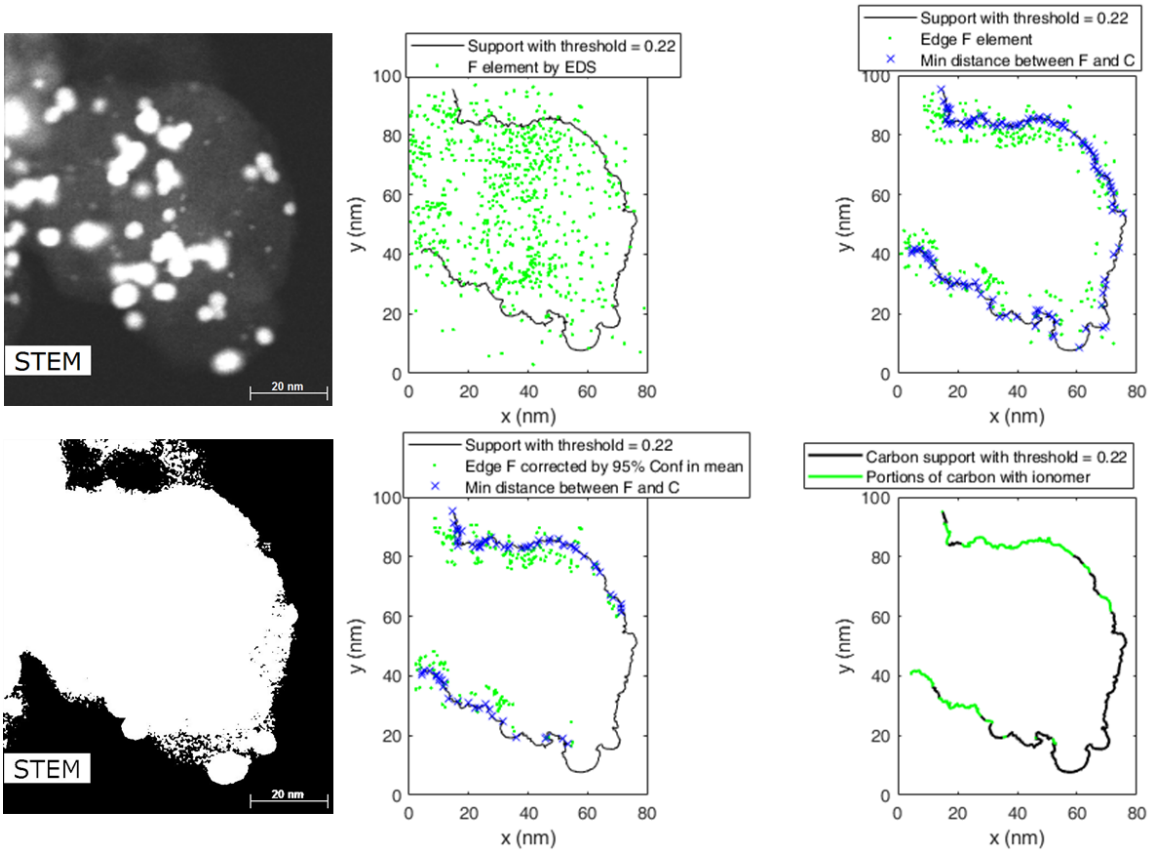

Figure A-6 Ionomer coverage of Pt/KB (pristine) = 33% for an I/C weight ratio of 1.06.

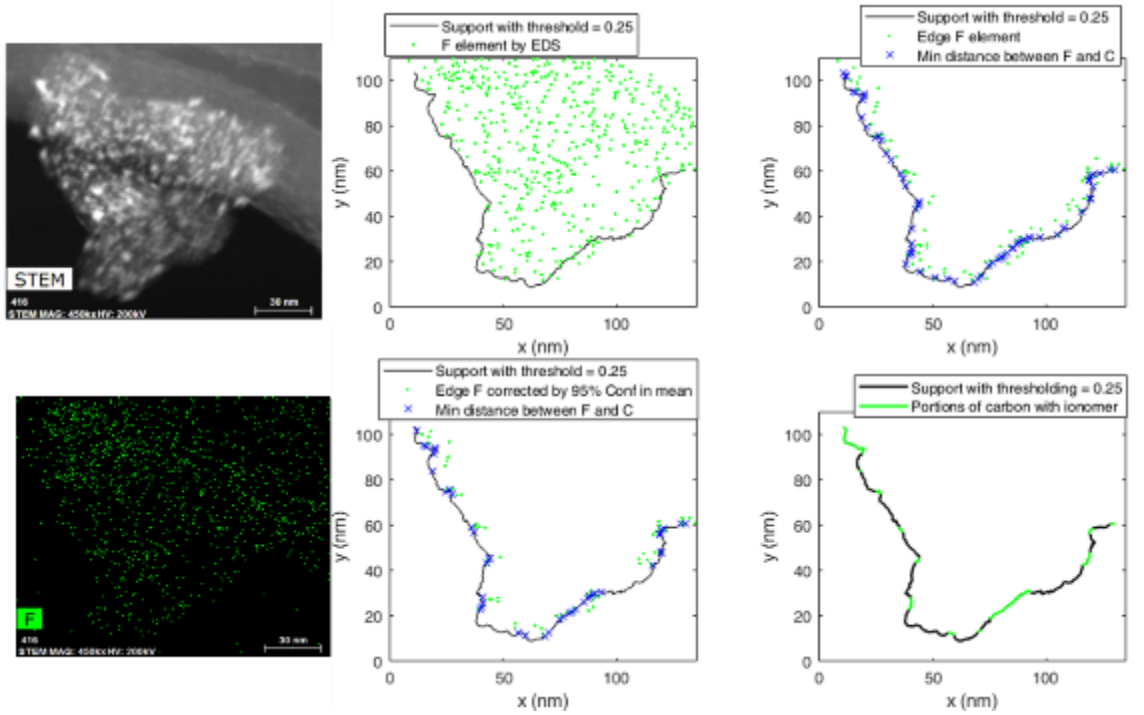

Figure A-7 Ionomer coverage of Pt/KB (scheme 1) = 39% for an I/C weight ratio of 0.66 $\pm$ 0.2

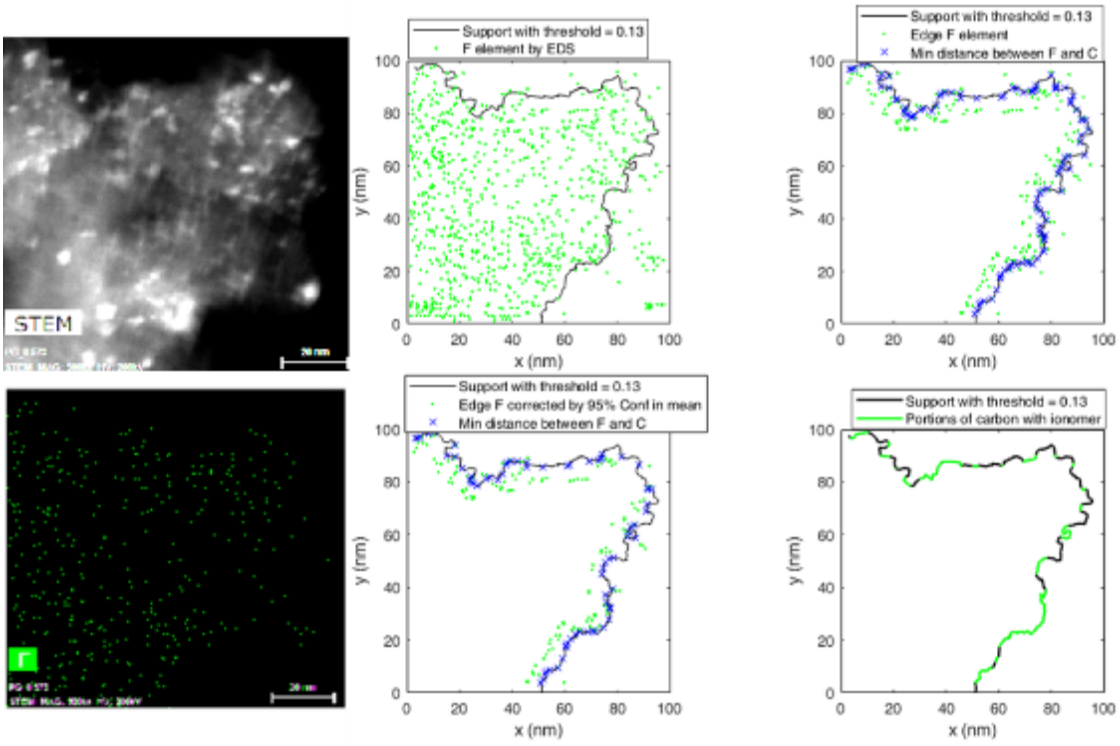

Figure A-8 Ionomer coverage of Pt/KB (scheme 2) = 34% for an I/C weight ratio of 0.66 $\pm$ 0.2

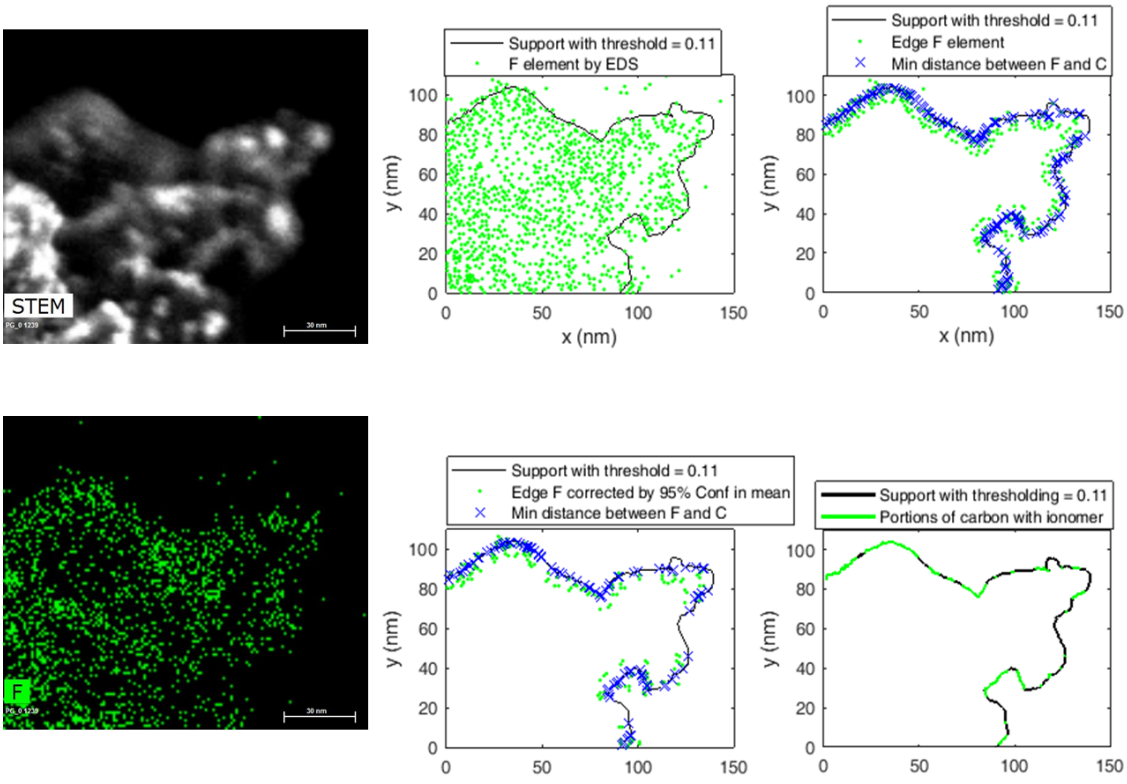

Figure A-9 Ionomer coverage of Pt/KB = 38% for an I/C weight ratio of 0.66 $\pm$ 0.2

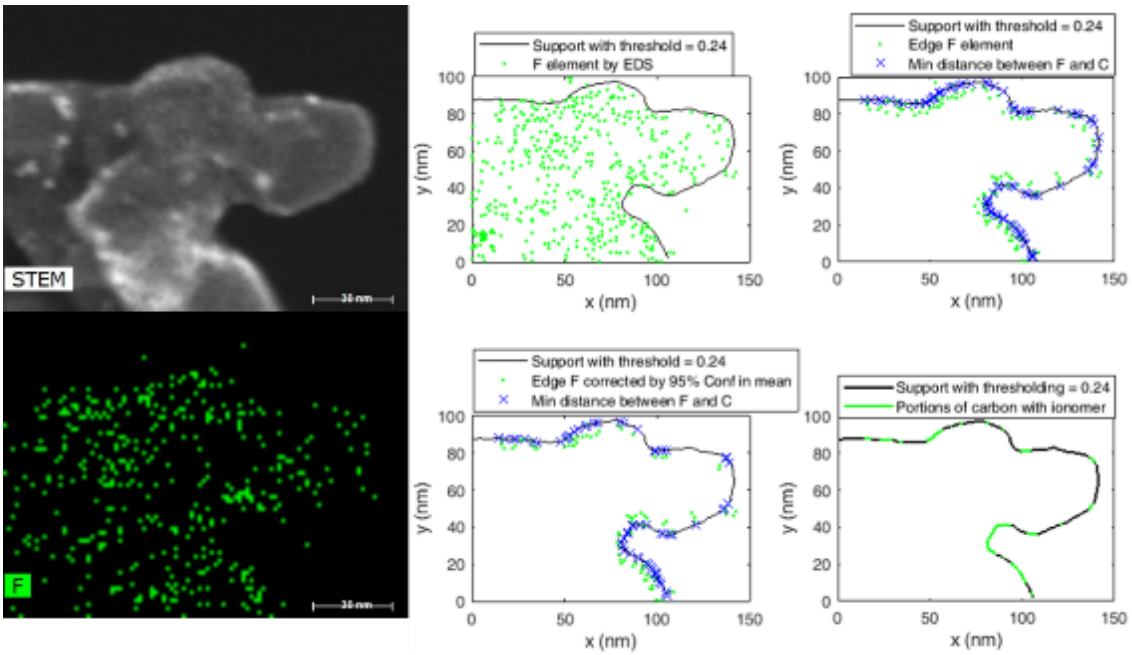

Figure A-10 Ionomer coverage of Pt/KB (scheme 2, 0.6% N) = 29% for an I/C weight ratio of 0.66 ± 0.2

A.2.4 Matlab Code

```
clear all
tic
i_thickness = 7;%nm
i_width = 4;%nm
sample = 'ink135_1';
 Directory = fullfile('C:\Users\zfang9\Documents\FC Research\Kolon
Research\TEM and STEM\Pt_Pristine Ketjen\PtC 019\I to C ratio =
1.06\EDS');
Filename = strcat(sample,'.xlsx');
delimiterIn = ' ';
Results = importdata(fullfile(Directory, Filename),delimiterIn);
X = Results.data;

x =X(:,1); x = x(find(x>0));
y =X(:,3); y = y(find(y>0));
%Reduce the size of input of carbon support edge
 divi = 5;
 for nn = 1:1:round(length(x)/divi)
        bb = divi*nn-(divi-1);
        xs(nn) = x(bb); ys (nn) = y(bb);
 end
 x=xs'; y = ys';
  x_F_all = X(:,10); x_F_all = x_F_all(find(x_F_all>0));
  y_F_all = X(:,12); y_F_all = y_F_all(find(y_F_all>0));

%find F points within 7nm from the carbon support e
   DistCF = zeros(length(x_F_all),1);
```

```
   DistCF1 = zeros(length(x),1);

   for k = 1:length(x_F_all)
       for kk = 1:length(x)
           DistCF1 (kk) = sqrt((x(kk)-x_F_all(k))^2+(y(kk)-
y_F_all(k))^2);
       end
       DistCF(k) = min(DistCF1);
   end

  DistCF_7nm = DistCF;x_F_7nm=x_F_all; y_F_7nm = y_F_all;
   for kkk = 1:length(x_F_all)
       if DistCF(kkk)>=i_thickness
           DistCF_7nm(kkk) = 0;
           x_F_7nm(kkk) = 0;
           y_F_7nm(kkk) = 0;
       end
   end
    %shorten the vectors of x_F and y_F
   DistCF_7nm_short=[];x_F_7nm_short = [];y_F_7nm_short = [];
       for kkkk = 1:length(DistCF_7nm)
           if DistCF_7nm(kkkk) >=eps
               DistCF_7nm_short = [DistCF_7nm_short;DistCF_7nm(kkkk)];
               x_F_7nm_short = [x_F_7nm_short; x_F_7nm(kkkk)];
               y_F_7nm_short = [y_F_7nm_short; y_F_7nm(kkkk)];
           end
       end

   % calculate the perimeter of carbon support
    Dist = 0;
    for i = 1:length(x)-1
        Dist = Dist + ((x(i)-x(i+1))^2+(y(i)-y(i+1))^2)^.5;
    end

    % calculate the perimeter of ionomer represented by F
         Dist_F=0;Dist_F_neighbor=0;x_F_7nm_short; y_F_7nm_short;

        for m1 = 1:length(y_F_7nm_short)
            for m2 = 1:length(y_F_7nm_short)
            Dist_F_neighbor (m2)= ((x_F_7nm_short(m1)-
x_F_7nm_short(m2)).^2 +(y_F_7nm_short(m1)-y_F_7nm_short(m2)).^2).^.5;
            Dist_F_neighbor = Dist_F_neighbor(find(Dist_F_neighbor>0));
            end
            Dist_F(m1,1) = min(Dist_F_neighbor);
        end

    %exclude points with distance exceeding the avg distance of F
        Dist_F_avg = mean(Dist_F)
        [para1, para2]=poissfit(Dist_F,.05); % poisson distribution fit
        Dist_F_corr = 0;
        for mm =1: length(Dist_F)
            if Dist_F(mm) <= para2(2) % 95% confidence in upper limit
of the mean
            Dist_F_corr = [Dist_F_corr;Dist_F(mm)];
            else
            Dist_F_corr = [Dist_F_corr;0];
```

```
            end
            TotalDist_F_corr = sum(Dist_F_corr);
        end
        Dist_F_corr = Dist_F_corr(2:end);

        %extract x y values that are correspond to non-zero Dist_F_corr
        x_F_corr = x_F_7nm_short; y_F_corr = y_F_7nm_short;
        q = find(Dist_F_corr<eps);
        x_F_corr(q) = [];
        y_F_corr(q) = [];

          %find the x,y coordinates with shortest distance between the
F_7nm_short and the carbon edge
        dist_short1=zeros(length(x),length(x_F_7nm_short));
        dist_short1_min=zeros(1,length(x_F_7nm_short));
        for ww = 1:length(x_F_7nm_short)
            for www = 1:length(x)
                dist_short1(www,ww) = ((x_F_7nm_short(ww)-
x(www))^2+(y_F_7nm_short(ww)-y(www))^2)^.5;
            end
            dist_short1_min(1,ww)=min(dist_short1(:,ww));
        end

        for ww = 1:length(x_F_7nm_short)
            loc_x1(:,ww)=dist_short1(:,ww)==dist_short1_min(ww);
            %choose the last one if there more than one pt on carbon
            %support has the shortest distance with a F pixel
            if length(find(loc_x1(:,ww)==1))>1
                loc_x1_MoreThanOne=find(loc_x1(:,ww)==1);
                loc_x1_end=loc_x1_MoreThanOne(1);
                x_dist_short1(:,ww) =x(loc_x1_end);
                y_dist_short1(:,ww) =y(loc_x1_end);
            else
            x_dist_short1(:,ww)
=x(loc_x1(:,ww));y_dist_short1(:,ww)=y(loc_x1(:,ww));
            end
        end
        x_dist_short1=x_dist_short1';y_dist_short1=y_dist_short1';

        %find the x,y coordinates with shortest distance between the
F_corr and the carbon edge
        dist_short2=zeros(length(x),length(x_F_corr));
dist_short2_min=zeros(1,length(x_F_corr));
        for qq = 1:length(x_F_corr)
            for qqq = 1:length(x)
                dist_short2(qqq,qq) = ((x_F_corr(qq)-
x(qqq))^2+(y_F_corr(qq)-y(qqq))^2)^.5;
            end
            dist_short2_min(1,qq)=min(dist_short2(:,qq));
        end

        for qq = 1:length(x_F_corr)
            loc_x(:,qq)=dist_short2(:,qq)==dist_short2_min(qq);
             if length(find(loc_x(:,qq)==1))>1
                 loc_x_MoreThanOne=find(loc_x(:,qq)==1);
                 loc_x_end=loc_x_MoreThanOne(end);
```

```
                x_dist_short2(:,qq) =x(loc_x_end);
                y_dist_short2(:,qq) =y(loc_x_end);
             else
            x_dist_short2(:,qq)
=x(loc_x(:,qq));y_dist_short2(:,qq)=y(loc_x(:,qq));
             end
        end
        x_dist_short2=x_dist_short2';y_dist_short2=y_dist_short2';

        %Find if the distribution of blue cross marks is Poisson
        Dist_C=0;Dist_C_neighbor=0;

        for n1 = 1:length(x_dist_short2)
            for n2 = 1:length(x_dist_short2)
            Dist_C_neighbor (n2)= ((x_dist_short2(n1)-
x_dist_short2(n2)).^2 +(y_dist_short2(n1)-y_dist_short2(n2)).^2).^.5;
            Dist_C_neighbor = Dist_C_neighbor(find(Dist_C_neighbor>0));
            end
            Dist_C(n1,1) = min(Dist_C_neighbor);
        end
            Dist_C = sort(Dist_C);

    %exclude points with distance exceeding the avg distance of F
        [paraC1, paraC2]=poissfit(Dist_C,.05); % poisson distribution
fit

        %find the x,y coordinates with
        DistCF2 = zeros(length(x),1);
        for p = 1: length(x_F_corr)
            for pp = 1: length(x)
            DistCF2(pp) = sqrt((x(pp)-x_F_7nm(p))^2 + (y(pp)-
y_F_7nm(p))^2);
            %DistCF2(pp) = sqrt((x(pp)-x_F_7nm_short(p))^2 + (y(pp)-
y_F_7nm_short(p))^2);
            end
            x_DistCF(p) = x(DistCF2 ==min(DistCF2));
            y_DistCF(p) = y(DistCF2 ==min(DistCF2));
        end
       x_DistCF = x_DistCF';y_DistCF = y_DistCF';

    subplot(2,2,1)
    plot(x,y,'k-',x_F_all,y_F_all,'g.')
    xlabel('x (nm)')
    ylabel('y (nm)')
    axis([0 240   0 125])
    str = 1;
     legend(cell2mat(str),'F element by EDS')
        daspect([1 1 1])

    subplot(2,2,2)
    plot(x,y,'k-
',x_F_7nm_short,y_F_7nm_short,'g.',x_dist_short1,y_dist_short1,'bx')
    xlabel('x (nm)')
    ylabel('y (nm)')
 axis([0 240   0 125])
    str = { 'Support with threshold = 0.22'};
```

```
     legend(cell2mat(str),'Edge F element','Min distance between F and
C')
          daspect([1 1 1])
    subplot(2,2,3)
    plot(x,y,'k-
',x_F_corr,y_F_corr,'g.',x_dist_short2,y_dist_short2,'bx')
    % plot(x,y,'k-',x_F_corr,y_F_corr,'go')
    xlabel('x (nm)')
    ylabel('y (nm)')
   axis([0 240   0 125])
    str = { 'Support with threshold = 0.22'};
    legend(cell2mat(str),'Edge F corrected by 95% Conf in mean','Min
distance between F and C')
        daspect([1 1 1])

 %since F pixels were not in order, need to rank x1,y1 in order of the
x,y curve
x1=x_dist_short2;y1=y_dist_short2;
rank_x1=zeros(length(x1),1); rank_y1=zeros(length(y1),1); %create an
empty array
for i=1:length(x1)
nx1{i,:}=find(x==x1(i)); %find the position of each x1 element in the
order of x array
ny1{i,:}=find(y==y1(i)); %each x1 element may correspond to multiple
positions in x array

    if length(intersect(nx1{i,:},ny1{i,:}))>1
        all_intersect=intersect(nx1{i,:},ny1{i,:});
        rank_x1(i)=all_intersect(end);
        rank_y1(i)=all_intersect(end);
    else
        rank_x1(i)=intersect(nx1{i,:},ny1{i,:}); % consider both x and
y, the multiple positions from the previous step will narrow down to
one position
        rank_y1(i)=intersect(nx1{i,:},ny1{i,:});
    end
end
[Bs, Bi] = sort(rank_x1,'ascend');
%x1_ranked=x1(Bi);y1_ranked=y1(Bi);

          V =x1(Bi);      D = diff([0;V;0]==0);
            C = arrayfun(@(b,e)V(b:e-1),find(D<0),find(D>0),'uni',0);
            V1 =y1(Bi);      D1 = diff([0;V1;0]==0);
            C1 = arrayfun(@(b,e)V1(b:e-
1),find(D1<0),find(D1>0),'uni',0);
            Bx = cell2mat(C);By = cell2mat(C1);
            i=1;Barray_x = Bx(1);Barray_y = By(1);
            for i = 1:(length(Bx)-1)
                dist(i) = sqrt((Bx(i)-Bx(i+1))^2+(By(i)-By(i+1))^2);
                if dist(i)<=i_width

Barray_x=[Barray_x;Bx(i+1)];Barray_y=[Barray_y;By(i+1)];
                else
                    Barray_x =[Barray_x;0;Bx(i+1)];Barray_y
=[Barray_y;0;By(i+1)];
                end
```

```
            end
            Vx =Barray_x;       Dx = diff([0;Vx;0]==0);
            Cx = arrayfun(@(b,e)Vx(b:e-
1),find(Dx<0),find(Dx>0),'uni',0);
            Vy =Barray_y;       Dy = diff([0;Vy;0]==0);
            Cy = arrayfun(@(b,e)Vy(b:e-
1),find(Dy<0),find(Dy>0),'uni',0);
     Dist_corr = 0;
     for i = 1:length(Cx)-1
        for ii = 1:length(Cx{i})-1
         Dist_corr = Dist_corr + ((Cx{i}(ii)-Cx{i}(ii+1))^2+(Cy{i}(ii)-
Cy{i}(ii+1))^2)^.5;
        end
     end
    x2=max(x1);
    y2=y1(find(x1==max(x1)));

%find coordinates in x and y in a cell array according to Cx (x1)and
Cy(y1) separated into different cells
for i = 1:length(Cx)
    if length(Cx{i})>=1 %number of elements in each row>1 means
coverage should be added over this range
        nx=cell(length(Cx{i}),1);ny=cell(length(Cx{i}),1);

        for ii = 1:length(Cx{i}) %
        nx{ii,:}=find(x==Cx{i}(ii));
        ny{ii,:}=find(y==Cy{i}(ii));
            if length(intersect(nx{ii,:},ny{ii,:}))>1
                Individual_intersect=intersect(nx{ii,:},ny{ii,:});
               rank_x{i,1}(ii)=Individual_intersect(1);
                rank_y{i,1}(ii)=Individual_intersect(1);
            else
                rank_x{i,1}(ii)=intersect(nx{ii,:},ny{ii,:});
                rank_y{i,1}(ii)=intersect(nx{ii,:},ny{ii,:});
            end
        end

        rank_x_array{i,1}=[min(rank_x{i,1});max(rank_x{i,1})];

        if length(rank_x_array{i})==2 %if repeated like [43;43], the
code will still proceed
            %but rank_x_array_x is just one value, so it's good!
             for n=1:((rank_x_array{i}(2)-rank_x_array{i}(1))+1)
                rank_x_array_x{i,:}(n)=x(rank_x_array{i}(1)+n-1);
                rank_y_array_y{i,:}(n)=y(rank_x_array{i}(1)+n-1);
             end
        end
       % rank_x_array_x_added=rank_x_array_x;
        if length(rank_x_array_x{i,:})==1
            if rank_x_array{i}(1)==length(x)
                rank_x_array_x_added{i,:}=[x(rank_x_array{i}(1)-
1);x(rank_x_array{i}(1))];
                rank_y_array_y_added{i,:}=[y(rank_x_array{i}(1)-
1);y(rank_x_array{i}(1))];
                rank_x_array_x{i,:} =rank_x_array_x_added{i,:};
                rank_y_array_y{i,:} =rank_y_array_y_added{i,:};
```

```
            elseif rank_x_array{i}(1)==1

rank_x_array_x_added{i,:}=[x(rank_x_array{i}(1));x(rank_x_array{i}(1)+1
);x(rank_x_array{i}(1)+2)];

rank_y_array_y_added{i,:}=[y(rank_x_array{i}(1));y(rank_x_array{i}(1)+1
);y(rank_x_array{i}(1)+2)];
                rank_x_array_x{i,:} =rank_x_array_x_added{i,:};
                rank_y_array_y{i,:} =rank_y_array_y_added{i,:};
            else
                rank_x_array_x_added{i,:}=[x(rank_x_array{i}(1)-
1);x(rank_x_array{i}(1));x(rank_x_array{i}(1)+1)];
                rank_y_array_y_added{i,:}=[y(rank_x_array{i}(1)-
1);y(rank_x_array{i}(1));y(rank_x_array{i}(1)+1)];
                rank_x_array_x{i,:} =rank_x_array_x_added{i,:};
                rank_y_array_y{i,:} =rank_y_array_y_added{i,:};
            end
        end
     end
end
%Det the total distance covered by ionomer
Dist_corr = 0;
     for i = 1:length(Cx)-1
        for ii = 1:length(Cx{i})-1
         Dist_corr = Dist_corr + ((Cx{i}(ii)-Cx{i}(ii+1))^2+(Cy{i}(ii)-
Cy{i}(ii+1))^2)^.5;
        end
    end

    subplot(2,2,4);
    graph1= plot(x,y,'k-');%,x1,y1,'g-',x2,y2,'g-',x3,y3,'g-',x4,y4,'g-
',x5,y5,'g-',x6,y6,'g-',x7,y7,'g-',x8,y8,'g-',x9,y9,'g-');
    set(graph1,'LineWidth',1.5)
     hold on

 for n=1:length(rank_x_array_x)
     graph1=plot(rank_x_array_x{n},rank_y_array_y{n},'g-');
     set(graph1,'LineWidth',1.5)
 end
    %graph1 = plot(x_DistCF,y_DistCF,'.')
    set(graph1,'LineWidth',1.5)
     xlabel('x (nm)')
    ylabel('y (nm)')
   axis([0 240   0 125])
    str = { 'Carbon support with threshold = 0.22'};
    legend(cell2mat(str),'Portions of carbon with ionomer')
     daspect([1 1 1])

   str = {'Surface Ionomer Coverage =  ' num2str(Dist_corr/Dist*100) '
%'};
    suptitle(cell2mat(str));

    display( Dist,' Carbon Support Surface (nm)')
    display(Dist_corr,' Ionomer Surface after correction (nm)')
    display(Dist_corr/Dist,' Ionomer Surface Fraction')
    toc
```

A.2.5 References

1. Y.-C. Park, H. Tokiwa, K. Kakinuma, M. Watanabe, and M. Uchida, *Journal of Power Sources,* **315** 179-191 (2016).